

16. Mai 1994

Diss. ETH Nr. 10644

**Stress corrosion cracking of pressure vessel steels
in high temperature water**

A dissertation submitted to the
SWISS FEDERAL INSTITUTE OF TECHNOLOGY ZURICH
for the degree of
Doctor of Technical Sciences

presented by

Andreas Kraus

Dipl. Werkstoff-Ing. ETH
born January 1, 1964
citizen of Uster (ZH)

Accepted on the recommendation of
Prof. Dr. Dr. h.c. M. O. Speidel, examiner
Prof. Dr. H. Böhni, co-examiner



Preface

The present work was performed at the Institute of Metallurgy of the Swiss Federal Institute of Technology in Zurich from 1989 to 1993. Financial support was given by the Swiss Federal Nuclear Safety Inspectorate.

As my mentor and head of the Institute, I like to thank Prof. Dr. Dr. h.c. Markus O. Speidel for his commitment, confidence and guidance in the course of this work.

I thank Prof. Dr. Hans Böhni for the acceptance of the role as co-examiner

In memory of the deceased Dr. Paul Sigrist, I like to express my grief and gratitude for his support in technical issues.

I owe a thank to Ueli Ineichen and Dr. Philip Tipping from the Paul Scherrer Institute for their effort in operating and managing the refreshed water loop and delivering the material.

Further, I thank all the colleagues at the Institute who all contributed in some way to the successful outcome of this work, be it by giving technical or personal support.

Abstract

The generation of electrical energy in thermal power stations is generally based on water as the heat carrier because of its availability and easy handling. Unfortunately, this results also in a variety of corrosion problems which affect the reliability and restrict the useful life of the equipment.

The present work concentrates on the investigation of stress corrosion cracking of reactor pressure vessel steels in hot water above 200 °C, under environmental conditions resembling those in the primary circuit of light water reactors under normal and faulted conditions.

Today it's well known that practically all of the applied structural metallic alloys may undergo environmentally assisted cracking in hot water, if stresses and environment meet certain conditions. It has become apparent that in relation to the susceptibility to stress corrosion cracking with deionized water is not just water and therefore a number of physical and chemical parameters, partly difficult to access by analytical and measuring techniques, play a decisive role. The effect of these parameters is much too little understood quantitatively to set up reliable thresholds and computation bases.

It was the intention and the goal of this work to quantitatively investigate the main influential parameters of stress corrosion cracking in high temperature water with low alloy reactor pressure vessel steels.

For the testing, a fracture mechanics based technique with precracked double cantilever beam specimens was used to obtain directly measurable crack growth rates. The important parameters which were systematically examined were the dissolved oxygen content and the resulting corrosion potential, the temperature, the stress intensity and the specimen geometry as well as impurities in the water.

It became apparent that the corrosion potential at the crack mouth has a very strong effect and for sustained crack growth, must exceed a certain threshold level. This threshold is however dependent on the temperature, the chemical composition of the water and steel and possibly other factors.

The main part of this work was dedicated to the study of the effect of the corrosion potential and the temperature on the growth rate of stress corrosion cracks. The results obtained allow to define the conditions for fast and stable crack growth in hot water above 200 °C. They provide information about the maximum growth rate which can be expected. Quantitative interrelations between the dissolved oxygen content, the corrosion potential, the temperature and the resulting susceptibility to stress corrosion cracking are given.

Zusammenfassung

Die Erzeugung elektrischer Energie in thermischen Kraftwerken basiert meist auf dem Wärmeträger Wasser, da dieser billig verfügbar und einfach zu handhaben ist. Leider ergeben sich dadurch auch eine Vielzahl von Korrosionsproblemen, welche die Betriebsicherheit beeinträchtigen und die Lebensdauer der Anlagen einschränken.

Die vorliegende Arbeit konzentriert sich auf die Untersuchung der Spannungsrisskorrosion von Reaktordruckbehälterstählen in Heisswasser, unter Bedingungen, welche denen im Primärkreislauf von Leichtwasserreaktoren ähnlich sind.

Es kann heute als sicher angesehen werden, dass praktisch alle heisswasserbeaufschlagten metallischen Legierungen in irgend einer Weise Spannungsrisskorrosion zeigen können, falls Spannungen und umgebendes Medium geeignete Bedingungen annehmen. Es hat sich gezeigt, dass im Zusammenhang mit der Anfälligkeit auf Spannungsrisskorrosion in Wasser eine Reihe physikalischer und chemischer, zum Teil analytisch und messtechnisch nur schwer zugänglicher Parameter eine entscheidende Rolle spielen. Der Einfluss dieser Parameter ist heute quantitativ viel zu wenig gut bekannt, als dass zuverlässige Grenzwerte und Berechnungsgrundlagen geschaffen werden könnten.

Es war Absicht und Ziel dieser Arbeit, anhand niedriglegierter Reaktordruckbehälterstähle einige Einflussgrößen quantitativ zu untersuchen und belastbare Ergebnisse zu gewinnen.

Zur experimentellen Untersuchung wurde eine bruchmechanische Versuchstechnik mit angerissenen Proben verwendet, welche als Ergebnis unmittelbar eine Risswachstumsgeschwindigkeit liefert. Zu den wichtigen Einflussgrößen, welche in der vorliegenden Arbeit systematisch untersucht wurden, gehören der Sauerstoffgehalt, das damit verbundene Korrosionspotential, die Temperatur, die Spannungsintensität und die Probengeometrie, sowie Verunreinigungen im Wasser.

Es hat sich gezeigt, dass das Korrosionspotential am Ort der Rissbildung den stärksten Einfluss ausübt und für schnelles Risswachstum notwendigerweise einen gewissen Grenzwert überschreiten muss. Dieser Grenzwert ist jedoch von der Temperatur, der Wasserchemie und Stahlzusammensetzung und möglicherweise von weiteren, noch nicht systematisch untersuchten Faktoren abhängig. In dieser Arbeit wurden insbesondere die Potentialabhängigkeit des Spannungskorrosions-Risswachstums sowie auch deren Temperaturabhängigkeit untersucht. Die gewonnenen Ergebnisse zeigen auf, unter welchen Bedingungen schnelles Risswachstum mit bekannter Geschwindigkeit in Heisswasser oberhalb 200 °C befürchtet werden muss und liefert quantitative Zusammenhänge zwischen dem gelösten Sauerstoff, dem Potential, der Temperatur und der Anfälligkeit auf Spannungsrisskorrosion.

Table of contents

| | |
|--|----|
| 1. Introduction | 1 |
| 1.1. Objectives | 2 |
| 2. Evaluation of stress corrosion cracking | 3 |
| 3. Materials | 9 |
| 3.1. Structure and chemical composition | 11 |
| 3.2. Mechanical properties | 12 |
| 4. Experimental | 14 |
| 4.1. Test facilities | 14 |
| 4.1.1. Recirculating water loop | 14 |
| 4.1.2. Static autoclaves | 15 |
| 4.2. Specimen preparation | 19 |
| 4.3. Stress intensity and crack length determination | 23 |
| 4.3.1. Compliance and stress intensity | 23 |
| 4.3.2. Crack length determination | 27 |
| 4.4. Measurement of the electrochemical potential | 30 |
| 4.5. Oxygen concentration in the water | 35 |
| 5. Results | 37 |
| 5.1. Free corrosion potential | 37 |
| 5.2. Refreshed autoclaves | 43 |
| 5.2.1. Test conditions | 44 |
| 5.2.2. Stress corrosion cracking results | 46 |
| 5.2.3. Effect of the electrochemical potential | 55 |
| 5.3. Constant load tests | 59 |
| 5.3.1. Test conditions | 59 |
| 5.3.2. Effect of stress intensity | 60 |
| 5.3.3. Effect of the electrochemical potential | 64 |
| 5.3.5. Effect of the temperature | 72 |
| 5.3.5. Effect of the specimen thickness | 75 |
| 5.3.6. Effect of higher water conductivities | 78 |

| | |
|--|-----|
| 6. Discussion | 81 |
| 6.1. Mechanical effects | 81 |
| 6.1.1 Load and strain effects | 82 |
| 6.2.2. Threshold stress intensity | 85 |
| 6.1.3. Fractographic features | 87 |
| 6.2. Environmental and combined effects | 89 |
| 6.2.1. Corrosion in high temperature water | 89 |
| 6.2.2. Critical corrosion potential | 95 |
| 6.2.3. Effect of the sulfur content in the steel | 97 |
| 6.3.4. Initiation of stress corrosion cracking | 99 |
| | |
| 7. References | 103 |
| | |
| 8. Appendix | 116 |

1. Introduction

Environmental degradation of engineering materials is one of the basic problems in their industrial application. One of the most severe forms of environmental attack is undoubtedly the process of stress corrosion cracking (SCC) whose appearance can be unexpected and unpredictable, affecting most often structural integrity. By definition, SCC is initiation and growth of cracks caused by the simultaneous interaction of tensile stress and an environment having access to the crack crevice. The complex interaction between stress, metallurgical and chemical (environmental) factors is a precondition for crack growth in all critical systems investigated so far. Stress corrosion cracks can be identified by a macroscopically brittle fracture which is extensively branched in most of the cases. Comprehensive reviews on SCC in different material/environment combinations have been published [1-8].

For the power generation industry, SCC is an inherent problem for all stressed parts in contact with water or steam. Affected alloys range from low alloy ferritic steels, the martensitic and austenitic stainless steels, up to high nickel alloys such as IN600.

A large number of corrosion related failures has been detected up to now in nuclear power plants [9-11] and a variety of reactor components like pressure vessel nozzles, piping and steam generators have been attacked [12-17]. Failure can often be attributed to high stresses and contamination of the environment. Unpredictable stresses may prevail in certain parts in form of inherent residual stress or adverse thermal gradients. These degradation problems result in extensive down-time and thus in a loss of plant availability and increased operation and maintenance costs. Equipment repair or replacement may be necessary to insure safe operation.

It may be assumed that nuclear power plants will account for a substantial part of the world-wide production of electrical energy for at least half a century from now. A large number of Light Water Reactors (LWR) plants will reach their design life of 30 (PWR) to 40 (BWR) years in the next decade [18]. Therefore, future efforts will be directed to extend time of operation of existing plants to reduce the amount of new constructions needed to satisfy the growing demand for electrical power. Assessment of the remaining lifetime by a detailed life evaluation procedure must replace the concept of a nominal lifetime. Components which are difficult or extremely costly to replace will clearly determine lifetime of the whole power plant. The central and most important of these components is the reactor pressure vessel containing the core with the nuclear fuel, where thermal energy is released from fission processes. The reactor pressure vessel integrity will therefore be an essential part for an evaluation of lifetime extension.

Reactor pressure vessel degradation is mainly discussed with respect to embrittlement by irradiation and thermal ageing. However, cracks may initiate and grow during service by fatigue, corrosion fatigue or stress corrosion cracking. There are a number of causes which can lead to crack initiation:

- Susceptible metallurgical conditions, e.g. at welds
- High local stresses outside the design rules
- Normal or faulted service environment
- Crevices, preexisting cracks etc.

Stainless steel pressure vessel steel cladding material has been observed to fail by strain assisted intergranular stress corrosion cracking [19]. An existing crack can propagate into the low alloy pressure vessel steel and grow by a SCC mechanism. Very fast growth rates are not impossible if conditions for SCC are met.

Crack growth rate evaluations on the basis of stress analysis, material properties and environment are needed to set up safety margins and to take measures for preventing environmental assisted cracking.

1.1. Objectives

Present knowledge about SCC of pressure vessel steels in high purity high temperature water in precracked specimens is based on a relatively small data collection [20]. For low alloy reactor pressure vessel (RPV) steels it has been shown that certain environmental parameters have an immense influence on the corrosion assisted crack growth in simulated reactor primary water. The interrelation between measurable damage quantities (e.g. crack growth rate) and all the system variables is not yet fully known.

The present work is thus intended to make a contribution to a quantitative determination and a theoretical approach about the influence of a variety of materials -, mechanical - and environmental parameters. The use of fracture mechanics specimens for these investigations allows to determine an accurately measurable crack growth rate under defined and reproducible mechanical conditions.

2. Evaluation of Stress Corrosion Cracking

Stress corrosion cracking (SCC) is characterized by the combined action of tensile stress (either residual or applied) and a specific environment on a susceptible material. The required stress level to cause crack growth is generally much lower than that required to fracture the material in an inert environment. Cracking may be either transgranular or intergranular, leading to a brittle-like fracture surface. An initiation step which consists of an incubation time and the nucleation of a detectable crack is usually included in the definition terminology of SCC. Transition from nucleation to propagation of a crack may be gradual both macroscopically and mechanistically during the involved corrosion process (e.g. pitting corrosion).

A lot of work has been done in the last four decades to evaluate the specific environmental parameters leading to SCC susceptibility in a variety of materials. Some examples for SCC promoting mediums in the case of carbon and low alloy steels are given in table 1. The observed crack path in these steels can be intergranular, transgranular or even mixed, depending on the environment and the metallurgical condition of the steel.

| medium | failure morphology |
|--|------------------------------------|
| caustic soda (OH ⁻) | intergranular |
| nitrate (NO ₃ ⁻) | intergranular |
| carbonate (CO ₃ ²⁻) | <i>intergranular/transgranular</i> |
| phosphate (PO ₄ ³⁻) | transgranular |
| sulfate (SO ₄ ²⁻) | intergranular/transgranular |
| cyanide (CN ⁻) | transgranular |
| CO-CO ₂ -H ₂ O | <i>transgranular</i> |
| high temperature water | transgranular |

Tab. 1: SCC promoting environments for carbon and low alloy steels

Laboratory-determination of SCC susceptibility in a specific material/stress/environment configuration results from the use of appropriate specimens. Many test methods are available and standardized through ASTM or ISO-standards and described in the literature [21-26].

In principle, the answers of the following questions are expected from laboratory SCC testing:

- Is stress corrosion cracking possible in a given test configuration.
- What are the decisive and controlling factors in the SCC process.
- What is the probability for initiation and propagation of SCC in a real component.
- What is the useful lifetime of a component under SCC conditions.
- How can SCC be avoided.

The present knowledge is far away from giving conclusive answers to all this questions, one of the main difficulties being the transfer from laboratory results to the situation in industrial components, which requires a mechanistic understanding of SCC. Most of the phenomenological data gathered so far is confined to the first of the above questions and thus mainly valuable to show whether susceptibility is given or not. In the following, some general views on specimen and test configuration, mechanistic and environmental aspects are made as a basis for later discussion.

Specimens for SCC testing can roughly be separated into smooth and notched or precracked shapes. The stress condition can be a constant applied load, a constant deflection or strain or a constant deflection or strain rate. Introduction of precracked specimens and the application of slow strain rates [27] and low frequency cyclic loading has led to a widespread use of these newer techniques.

SCC testing with precracked specimens is based on linear elastic fracture mechanics (LEFM) concepts which were developed to characterize the mechanical behaviour of materials incorporating cracks. This kind of test is closely related to service situations, where cracks in stressed parts are encountered during inspection. A single parameter, the stress intensity K , then serves to quantify the stress/strain field ahead of the crack and can be thought as a driving force available at the crack tip to induce SCC.

Specimen geometries were adopted from the commonly used forms as described e.g. in the ASTM E399 [33] standard for plane-strain fracture toughness determination since compliance and stress intensity calibration is known very well. Statically loaded samples can be configured with either a constant applied load or a fixed crack opening displacement such that K increases (constant load) or decreases (constant displacement) with crack length. A tapered geometry can be designed to keep an approximately constant stress intensity. To allow transfer of stress intensities from cracks in specimens

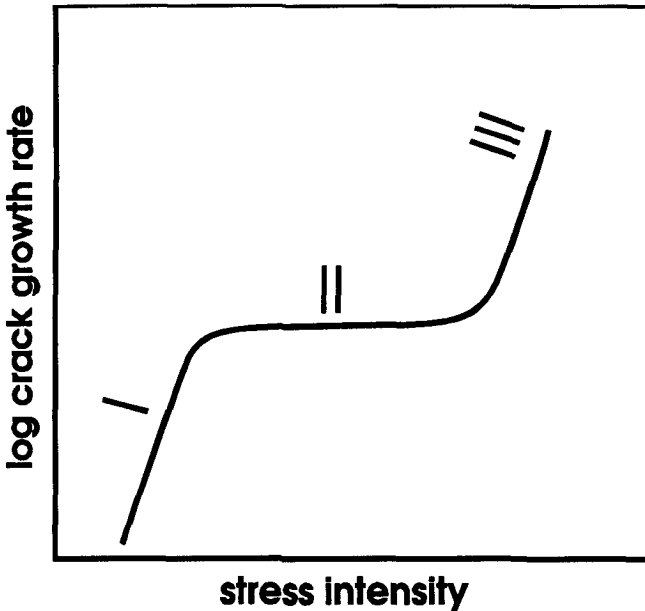


Fig. 1: Generalized plot of the influence of stress intensity on the velocity of stress corrosion cracking

to those in thick-walled service parts, plane strain conditions should be maintained. For thinner sections and more ductile alloys, the principle of small scale yielding becomes invalid and elastic-plastic concepts such as the J integral is used to define the stress state near the crack tip.

Besides the static loading modes, very low frequency stress cycling can be closest related to structures in a process plant with start-up and shut-down phases which are accompanied by changes in pressure and temperature.

Several techniques are available to measure the crack length in fracture mechanics specimens such as electrical resistance (potential drop) or compliance methods. The derived crack growth rate is usually plotted vs. the applied stress intensity, generally resulting in a relationship of the type depicted in figure 1.

Three distinctive crack growth regions are generally observed in experiments covering the whole range of possible stress intensity values. Region III applies to high stress intensities approaching the fracture toughness K_{IC} when fracture is purely mechanical resulting in ductile or brittle failure of the whole ligament. In Region II which covers a

broad stress intensity interval, crack growth rate is essentially constant or influence of stress intensity is weak. Kinetic considerations in the rate limiting step for the SCC process involving mass transfer of reaction products from and to the crack tip are believed to keep the velocity approximately constant. In ductile materials, extensive crack branching is usually encountered in this region, since multiple cracks 'seeing' different stress intensities can grow with about the same velocity. Because of the extensive crack branching, the true stress intensity at the crack tip varies with the crack angle and the number of cracks, complicating the specification of a stress intensity value. Generally, multiple cracks will decrease the stress intensity at the crack tips.

Region I shows a large decrease in crack growth rate by a small decrease in K_I . A vertical asymptote marks a threshold value known as K_{ISCC} , below which SCC is impossible. The practical definition of K_{ISCC} may be a function of the crack length measurement capability. It's important to notice that this value is not a material parameter comparable to K_{IC} but may vary with the prevailing environmental conditions. Determination of K_{ISCC} allows to set up safety margins in real components if a measurable flaw size is given. The flaw depth can be assumed to be the detection limit of the non destructive evaluation procedure or the maximum depth allowed by design codes.

Apart from the transferability to real components, stress corrosion testing with precracked specimens is valuable to study the mechanisms which lead to sustained cracking and to determine the main influential environmental parameters. Available crack length measurement capabilities allow to exactly follow the crack growth rate during an experiment.

Taking into account the most important models for an anodic SCC mechanism in high temperature water with a chemomechanical interaction between the crack tip plastic strain, anodic dissolution and hydrogen ad-/absorption, slow dynamic straining of a plane or precracked specimen is thought to severely promote failure not seen in constant load testing up to very long times.

This technique is known as slow strain rate testing (SSRT) or constant extension rate testing (CERT). A main feature of SSRT is that the test-end is always marked by specimen fracture, giving a result in comparatively short times. Several parameters may serve to measure the degree of susceptibility, which are the time to failure, elongation to fracture, reduction in area or the ductility ratio which compares the test result to one obtained in an inert environment. An important parameter in SSRT is the strain rate de/dt . At strain rates approaching those used in ordinary mechanical tensile tests on plane specimens, ductile fracture will be observed due to the short time to fracture and the kinetic limits in the growth of stress corrosion cracks. On the other side, at constant load

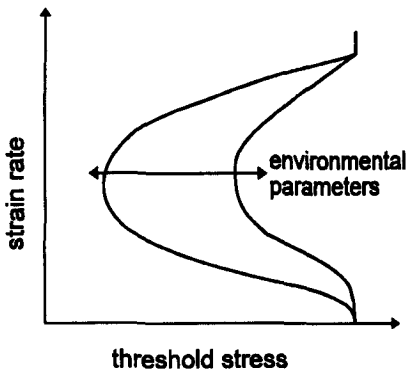
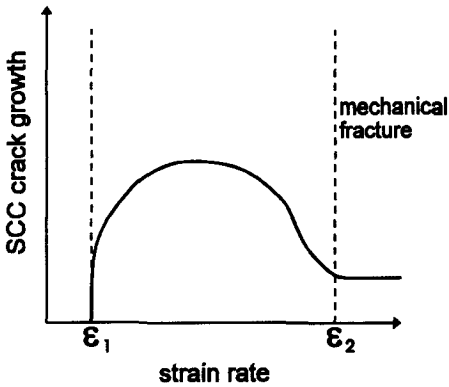


Fig. 2a: Effect of strain rate on SCC crack growth rate in SSRT

Fig. 2b: Variation of threshold stress for SCC with strain rate

conditions, $d\epsilon/dt$ decreases rapidly to very low values. It has been demonstrated for some metal-environment combinations, that susceptibility is not seen in constant load tests with plane specimens [28]. Accordingly, there is a lower threshold for $d\epsilon/dt$ below which SCC is not initiated on a plane surface. This effect is illustrated in figure 2a. The threshold stress for SCC is also a function of the applied strain rate as shown schematically in figure 2b.

Often, a strain rate of about 10^{-6} s^{-1} is chosen because many systems show a large susceptibility at this value and test times can be kept relatively short [29]. However, for SCC-systems involving very slow stress corrosion crack growth rates, SSR tests with 10^{-6} s^{-1} may be misleading, since they would indicate immunity to SCC where there may

indeed be an enormous SCC problem, albeit with very slow cracks, thus demanding longer testing times to be observed.

The sensitivity of stress corrosion initiation to dynamic straining is closely related to the surface condition of the metal. It's a characteristic feature of metallic corrosion in aqueous environments that protective surface films develop which can lower the dissolution rate by several orders of magnitude. These protective oxide-layers are responsible for the excellent corrosion resistance of many alloys in aggressive solutions. However, this protection from uniform corrosion goes along with a susceptibility to local attack due to aggressive ions or mechanical tearing since ductility of the layer is generally much lower than that of the bulk material. Local corrosion attack and rupture/repair of oxide films further stress the relevance of time related effects in a mechanistic approach to SCC. Strain rate effects are also encountered in precracked specimens. This is shown by the existence of a threshold stress intensity K_{ISCC} which is a function of the beam deflection rate in a rising load test.

Precracking and continuous straining thus facilitate the initiation step for crack nucleation. However, dynamic stressing does not circumvent the initiation stage since this may involve the establishment of localized particular environmental conditions. Comparison of tests performed with different specimen and load configuration clearly show that a localized aggressive environment is probably most important for the onset of SCC. The development of occluded cells in pits, crevices or cracks is accompanied by large changes in the solution chemistry which are electrochemical implications of variations in the corrosion potential and the localized enhanced dissolution. The highly directional crack path requires a narrow process zone at the crack tip with strong mechano-chemical interactions.

Above considerations clearly show that proper stress corrosion testing for evaluation of materials and environments is complex. To assure reproducible and comparable results, system parameters have to be known as exactly as possible, which requires expensive instrumentation capabilities. Though world-wide effort are made in this area, a certain unpredictability will still remain in SCC testing due to statistical scatter in the corrosion processes and the inhomogeneity of the investigated material.

3. Materials

Investigated materials were exclusively low alloy steels which are typically used for nuclear pressure vessels and piping. With few exceptions, the present work concentrated on four different heats of the standard nuclear reactor pressure vessel steel 20MnMoNi55 or A533B according to ASTM specifications [30]. These steels are alloyed with Manganese, Molybdenum and Nickel to improve hardability for large cross-sections. The normal heat treatment consists of normalizing, quenching and tempering at 650 to 700 °C to get a fine grained bainitic microstructure and to achieve high toughness and moderate strength. Such pressure vessel steels are not susceptible to temper embrittlement but their toughness may be lowered during the lifetime when exposed to fast neutron irradiation in a nuclear pressure vessel.

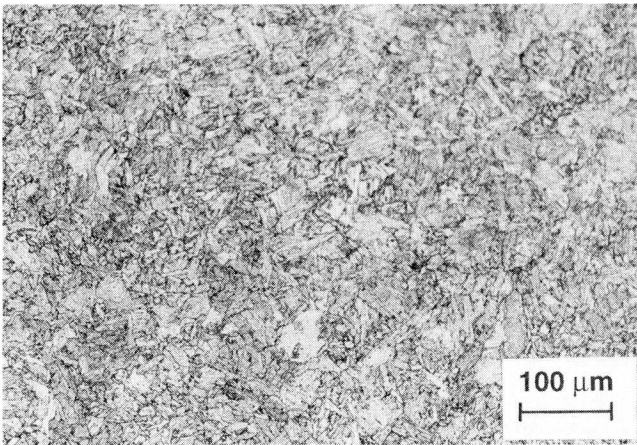


Fig. 3: Etched microstructure of nuclear pressure vessel steel 20MnMoNi55

| steel designation | C | Si | Mn | P | S | Cr | Mo | Ni | V | Al | Cu |
|-------------------|------|------|------|-------|-------|-------|-------|------|-------|-------|------|
| 20MnMoNi55 A | 0.15 | 0.29 | 1.40 | 0.005 | 0.005 | 0.14 | 0.51 | 0.65 | 0.007 | 0.036 | - |
| 20MnMoNi55 B | 0.21 | 0.23 | 1.26 | 0.004 | 0.005 | 0.14 | 0.53 | 0.81 | 0.008 | 0.019 | 0.08 |
| 20MnMoNi55 C | 0.19 | 0.20 | 1.39 | 0.008 | 0.010 | 0.14 | 0.53 | 0.53 | 0.009 | 0.04 | 0.08 |
| 20MnMoNi55 D | 0.25 | 0.24 | 1.42 | 0.006 | 0.012 | 0.12 | 0.54 | 0.62 | 0.007 | 0.03 | 0.15 |
| A508-II | 0.21 | 0.27 | 0.69 | 0.005 | 0.004 | 0.38 | 0.63 | 0.78 | 0.006 | 0.015 | 0.16 |
| BW 30 | 0.17 | 0.31 | 1.50 | 0.019 | 0.012 | 0.058 | 0.019 | 0.64 | 0.20 | 0.005 | - |

Tab. 2: Chemical composition of the investigated nuclear pressure vessel and piping steels

| steel designation | RP _{0.2} | R _m | A | Z | heat treatment | |
|-------------------|-------------------|----------------|------|------|--------------------------------------|--|
| | [MPa] | [MPa] | [%] | [%] | | |
| 20MnMoNi55 A | 533 | 669 | 22.3 | 74.5 | as received | |
| 20MnMoNi55 B | 464 | 622 | 19.0 | 58.3 | 900°C/1h/WQ;670/710°C/0.5h/air | |
| 20MnMoNi55 C | 565 | 684 | 19.6 | 73.5 | 910/920°C/6h/WQ;640/650°C/9.5h/air | |
| 20MnMoNi55 D | 468 | 616 | 21.0 | 43.0 | 915°C/12h/860°C/12h/WQ;660°C/18h/air | |
| A 508-II | 515 | 605 | 26.7 | 61.0 | as received | |
| BW 30 | 515 | 673 | 25.1 | 58.2 | as received | |

Tab. 3: Tensile mechanical properties and heat treatment of the investigated low alloy steels

3.1. Structure and chemical composition

A micrograph of the etched structure of a tempered pressure vessel steel is shown in figure 3. The structure contains finely dispersed carbides in a ferritic matrix. The prior austenite grains are visible due to a carbide border. The chemical composition of the investigated steels is listed in table 2. A piping steel with the designation BW30 was also tested for comparison and is included in the list.

Steels A to D are very similar in their composition, except for the sulphur content, which ranges from low to medium values. Additionally, another low sulfur pressure vessel steel A508-II was also included at a later stage of this work to investigate the effect of the specimen thickness. The sulfur content was expected to possibly have some influence on the susceptibility to SCC in high temperature water. A steel with more than 0.02 wt. % sulfur would have been desirable for a more extended comparison, but modern steel making has reached such a high standard that available alloys are generally very low in sulfur content. However, steels presently in service in older power plants may have still sulfur contents above 0.02%.

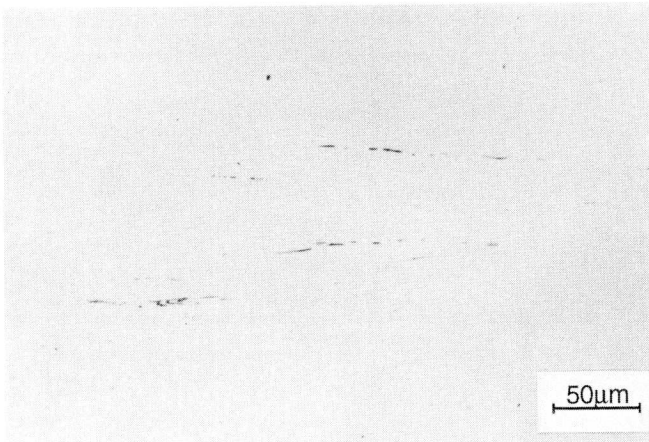


Fig. 4: Mechanically polished surface of alloy B

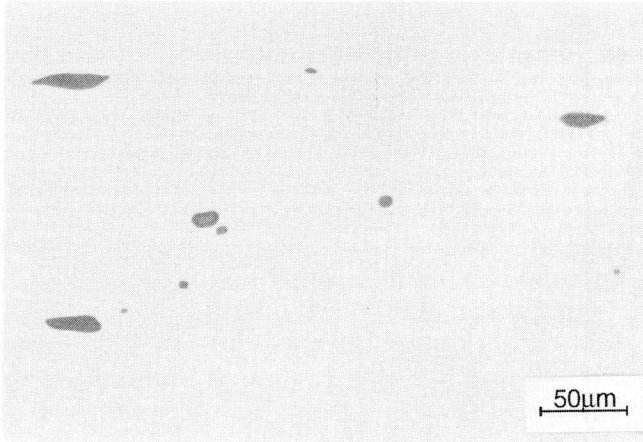


Fig. 5: Mechanically polished surface of alloy D

MnS inclusions may have an important role for stress corrosion susceptibility. A strong influence on the ductility, e.g. the upper shelf toughness and the ductile/brittle transition in impact tests, is also observed. Figures 4 and 5 show mechanically polished surfaces of alloy B and D, a low and a medium sulfur steel. The difference in MnS size and orientation is very large in these two alloys. Alloy A, B and C contain smaller particles which are strongly elongated in the rolling direction. In contrast, alloy D contains large globular particles up to about 100 microns in diameter.

3.2. Mechanical properties

The four pressure vessel steel alloys were originally delivered as plate material from which a part was available to cut the specimens used in this work. Mechanical properties were measured in tensile tests at room temperature and are given in table 3, together with the heat treatment as far as known. Additional heat treatments were not performed. Tensile properties are mean values of longitudinal and transverse gage orientations, but values showed only slight differences. The toughness properties of the investigated pressure vessel steels were determined with standard charpy V-notch impact tests and J-

Integral fracture mechanics tests. The Charpy energies are given in table 4 as a mean value from three specimens for longitudinal and transverse crack plane orientation, respectively. There is a comparatively large difference between the two orientations, especially in alloy B. The difference elucidates the effect of inclusion elongation in the main rolling direction which reduces the transverse impact toughness but has little or no effect on strength properties. The lowest toughness was measured with alloy D which is the one with the highest sulfur content. For this alloy, the Charpy impact toughness lies in the brittle to ductile transition zone. Thus, for the temperatures at which stress corrosion tests were performed (usually above 200 °C), a better toughness can be expected. Fracture toughness at room temperature was measured by the J-Integral method according to ASTM E813 [31]. Specimen dimensions were those of a standard CT specimen, but only 40% of that size since specimens were taken from 10 mm thick plate material (DCB specimens for SCC testing). It was then seen that the thickness was too low to yield reproducible results (even with side notches), which however indicates a fracture toughness above 200 MPam^{1/2} for all steels at room temperature. Also, the thickness criteria $B > 2.5J_{IC}/\sigma_y$ could not be met any more at the high fracture toughness values.

| alloy designation | crack plane orientation | Charpy V-notch energy [J] at room temperature |
|-------------------|-------------------------|---|
| A | LT | 145 |
| B | LT | 186 |
| B | TL | 82 |
| C | LT | 160 |
| C | TL | 120 |
| D | LT | 64 |
| D | LT | 44 |

Tab. 4: Charpy V-notch impact energy of investigated steels

4. Experimental

4.1. Test facilities

4.1.1. Recirculated water loop

Testing of fracture mechanics specimens under well controlled environmental conditions was conducted in a recirculating water loop located at the Paul Scherrer Institute (PSI) in Würenlingen CH. A schematic view of the testing facility is given in figure 6. The loop roughly consists of a low pressure part and a high pressure high temperature part where specimens are located in two autoclaves. Construction material of all water-bearing tubes and autoclaves is stainless steel 316L.

Water is drawn from the 150-liter storage tank and pumped through a regenerative heat exchanger where heat is recovered from the water exciting the autoclaves. A heater is located downstream of the heat exchanger to increase the water temperature to the test temperature before it enters the autoclaves. Maximum flow rate through the high pressure pump is 35 l/h. Two test vessels with a volume of 10 litres each are installed parallel in the high pressure part where water flow can be regulated and measured independently. An additional high pressure circulation pump is able to produce a water flow rate of 600 l/h maximum in a loop through the autoclaves. Up to 16 wedge-loaded DCB specimens could be suspended into a holding frame which was attached to the bottom of the autoclave lid. Complete isolation of each specimen was achieved by ceramic parts. An external Ag/AgCl reference electrode allowed continuous recording of corrosion potential from the autoclave, a platinum redox electrode and four different specimens. Data was logged by computer control and saved on hard disc. A computer program was written to retrieve the data and plot them as a function of test time.

The low pressure part of the recirculation system contains most of the measurement capabilities. These comprise determination of oxygen concentration and conductivity for inlet and outlet water, pH, flow rate and temperature measurement. All relevant data (13 channels) is logged by computer and stored for later interpretation. The storage tank can alternatively be purged with pure argon or an argon/oxygen mixture. To keep a constant oxygen concentration in the water, a computer governs opening and closing of magnetic valves for the two gases and adjusts the measured concentration to the desired value. This feature allows to conduct experiments with an arbitrary oxygen concentration in the outlet water.

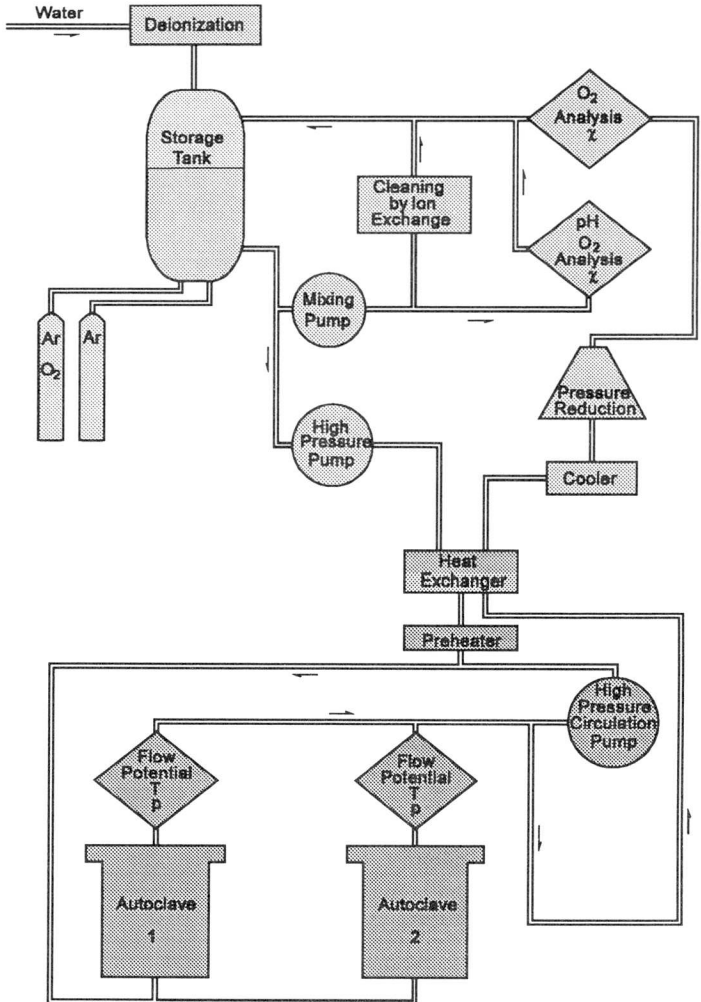


Fig. 6: Stress corrosion cracking autoclave recirculation system

4.1.2. Static autoclaves

Two autoclaves for constant load testing of fracture mechanics specimens were available at the Institute of Metallurgy. Both of them were internally developed and built [32]. Figure 7 shows a photograph of one autoclave mounted in a load frame.

The load bearing pull rods act horizontally and pass through the autoclave side wall. The sliding sleeve is water cooled and sealed with Teflon® slide rings and a Kalrez® sealing ring. Construction material for the first autoclave with a volume of 1.9 litres was stainless steel 316L. Design allows temperatures and pressures up to 350 °C and 200 bar. The second autoclave with a volume of 2.6 litres was totally made of TiPd0.15 which is known to have an excellent corrosion resistance when test environment contains high amounts of chloride (no such experiment has been done so far). Both autoclaves are heated by thermocoax heating elements located inside. Temperature is measured by one

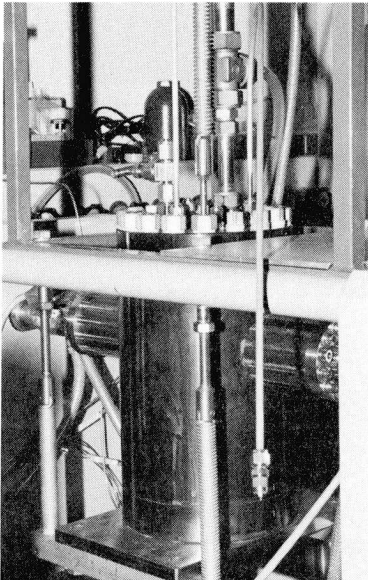


Fig. 7: Autoclave for constant load testing of DCB and CT specimens in high temperature high pressure water

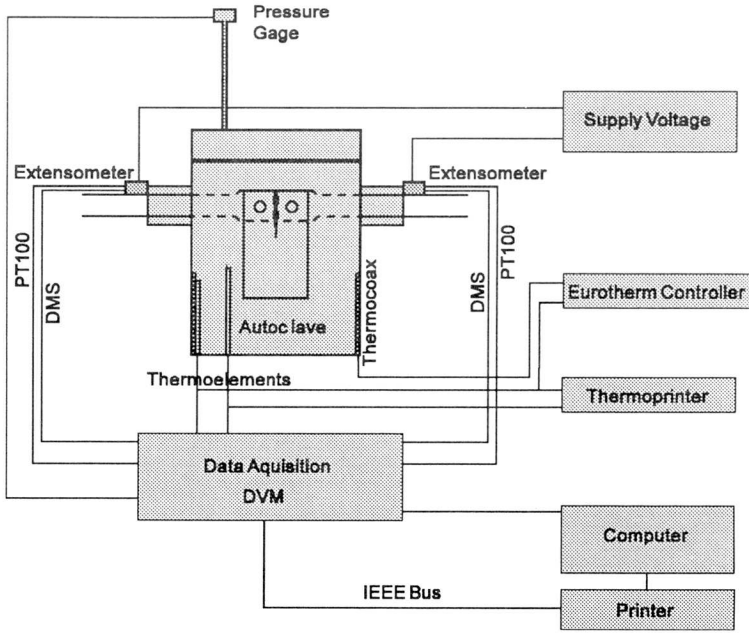


Fig. 8: Measuring arrangement for constant load autoclaves

thermocouple located near the specimen and controlled by another located next to the heating element.

To allow free movements and to prevent stuck pull rods, the autoclave body hangs freely on four springs which exactly counterbalance the weight. Load was applied manually in the form of 10.2 and 2.04 kg steel plates which are hanged on a cantilever beam arm rotating in a pin bearing to minimize possible friction. The construction provided a load ratio of 1:25.

Two extensometers measure a relative displacement of the tension rods vs. the autoclave body. The two signals are summed so that movements of the autoclave in rod axis direction will give the same displacement on each side and are thus compensated.

The extensometer signal is measured by a digital multichannel voltmeter which is controlled by a personal computer over the IEEE bus. A computer program starts a measurement cycle, calculates the actual load line displacement and prints the data on a printer functioning as a recorder. Figure 8 illustrates the device arrangement.

An installed extensometer is shown in figure 9. It contains a ring made of a high strength titanium alloy which gives a favourable ratio between strength and Young's modulus to allow a measuring range of about 1 mm. A full bridge wire strain gage was applied at the inner and outer sides of the ring. Each extensometer was separately calibrated and showed good linearity in its measuring range. Resolution of an extensometer was 10 nm and the measured noise band was generally smaller than 0.3 μm . Measurement precision was thus not limited by inadequate accuracy of the extensometers but by the much greater disturbances due to fluctuations of cooling water and the external room temperature.

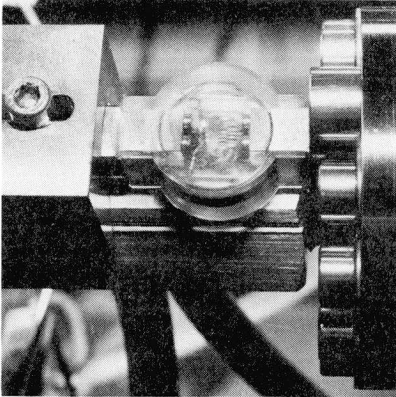


Fig. 9: Extensometer installed on the pull rod

4.2. Specimen preparation

Double cantilever beam (DCB) specimens were cut from the plate material described before. The specimen geometry is given in figure 10.

Crack plane orientation was marked on the top according to ASTM E399 [33]. Most of the specimens had either LT or TL orientation, so that the crack growth was in transverse and longitudinal direction, respectively. Front and back surfaces were ground in cross-direction and a chevron notch of 2 mm width was cut to a length of 30 mm from the upper edge. Precracking was done in air with a high frequency (≈ 100 Hz) resonance testing machine under load control and with a R-ratio of 0.1. The fatigue crack was usually initiated with an upper load of 8 kN and stopped at 4 to 5 kN which resulted in a stress intensity between 10 and 15 MPam^{1/2}. The initial crack length was measured at the side faces and the average between the two values was taken. Finally, before using a specimen, it was cleaned in a ultrasonic bath in pure solvents (ethanol, propanol, ethylacetate).

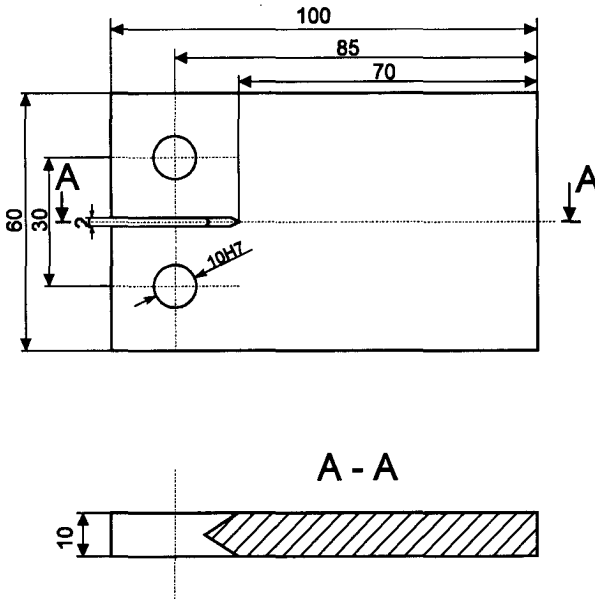


Fig. 10: Double cantilever beam specimen

The chosen specimen geometry allowed to perform stress corrosion tests with fixed load-line deflection as well as constant load imposed by a load frame and pins. A well established method to apply constant deflection is a wedge which is pressed into the gap resulting from the cutting of the chevron notch [34]. A suitable wedge material is alloy 718, heat treated to its maximum hardness of 39 to 40 HRC. The good corrosion resistance of this alloy prevents localized attack at the wedge in contact with the specimen. The total wedge angle was 6° , allowing to increase the crack opening displacement by about $50\ \mu\text{m}$ when pushing the wedge one mm further. A hand-operated hydraulic press served to insert the wedge into the chevron notch, simultaneously measuring crack opening displacement (COD) with a micrometric device.

Figure 11 illustrates the two possibilities and indicates the relevant geometry parameters.

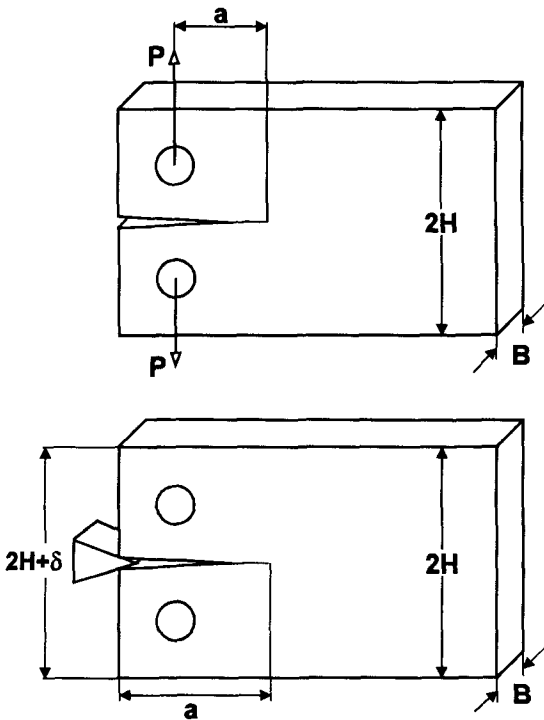


Fig. 11: Loading cases and relevant geometry parameters

Wedge-loaded specimens were inserted in the recirculating water loop described before. The simple loading arrangement offers several advantages for stress corrosion testing. Due to the fixed displacement, stress intensity decreases with crack length, thus allowing to determine the lower limit K_{ISCC} for stress corrosion cracking in the test environment. The space saving loading by wedges offers the possibility to test a lot of specimens simultaneously in the same environment. Loading and material parameters can thus be varied and investigated in the same test.

To insert the specimens into the autoclaves of the recirculating loop, a special specimen holding frame was built and attached directly to the bottom of the autoclave lid (figure 12). Complete electrical insulation of each single specimen was achieved by ceramic parts made of ZrO_2 .

The testing procedure for the recirculating water loop is given as follows:

All specimens were wedge loaded in air one day before assembling into the holding frame. Upon closing the test autoclaves they were filled and refreshed with cold (RT) deoxygenated water with a conductivity $< 0.1 \mu S/cm$. When heating up the loop, the

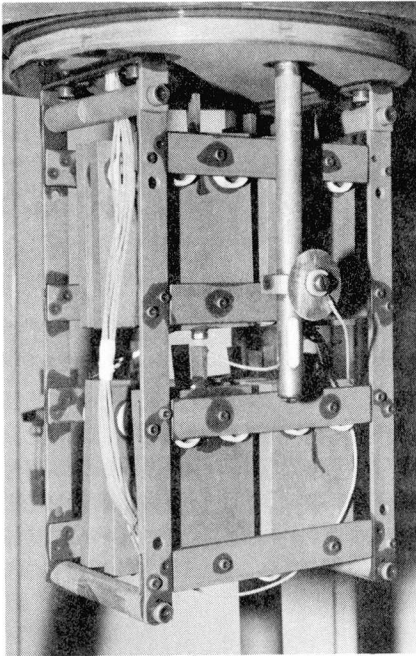


Fig. 12: Specimen holding frame used in recirculating loop

dissolved oxygen content was simultaneously raised to the desired level. Test conditions as specified were reached when oxygen content and conductivity were within $\pm 10\%$ of the intended values. These specifications evolved from the operating experience with the loop during the first tests when it was seen that both conductivity and oxygen content could be kept within a narrow scatterband.

Usually, conductivity took longest to reach test specifications since no attempt was made to add chemicals to the loop. At the desired test duration, the autoclaves were cooled down and the oxygen content was simultaneously lowered as fast as possible during this action to avoid low temperature corrosion.

4.3. Stress intensity and crack length determination

4.3.1. Compliance and stress intensity

Fracture mechanics specimens with well known calibration related to stress intensity factor and compliance are usually used for testing for investigation of stress corrosion cracking. Data can be found in the annual books of ASTM standards [33] and stress intensity handbooks [35,36]. However, specimens designed originally to determine characteristic quantities like fracture toughness, are often unsuitable for stress corrosion testing. (W-a) is too small to allow long stress corrosion cracks and high crack growth rates can be sustained for a short time only. Also, stress intensity increases strongly with growing crack length, which is often undesired. Specimens used in this work offer the possibility for longer stress corrosion cracks under both constant deflection and constant load. Due to the compromise between specimen length and width needed to apply constant load with pins, the calibration of stress intensity is not established very well.

Measuring compliance offers an experimental way to obtain K_I calibration factors for an arbitrary specimen design. Compliance is defined as the slope of a deflection δ vs. load P curve and is equivalent to the inverse spring constant. The concept of the calculation of a stress intensity factor K_I is based on the strain energy release rate G and the relationship between G and K_I [37].

It can be shown [43] that the strain energy release rate is given by:

$$G = \frac{P^2}{2B} \cdot \frac{\partial C}{\partial a} \quad (1)$$

where P is the applied load, B the thickness and C the compliance. The compliance is dependent upon Young's modulus E and geometry and can readily be measured.

The fundamental relationship between G and K_I [37] is given through :

$$K_I = \sqrt{E \cdot G} \quad (2)$$

combining equation 1 and 2 one gets:

$$K_I = P \sqrt{\frac{E}{2B} \cdot \frac{dC}{da}} \quad (3)$$

In practice, the normalized compliance $BE\delta/P$ is used for determination of K_I . Equation

3 may thus be altered to:

$$K_I = \frac{P}{B} \sqrt{\frac{1}{2S} \cdot \frac{d}{d} \cdot \frac{EBd}{P}} \quad (4)$$

S is a geometry parameter which is either one-half of the height (H/2) or the width (W) of the specimen.

Single-edge cracked plate specimens can be classified [42] according to the proximity (W-a) of the boundary normal to the direction of the crack plane. This boundary affects the stress field at the crack tip.

The DCB specimen is generally known in a configuration where (W-a) is large compared to a. Calibration equations for this type of specimen are valid only in a restricted range of the ratio a/H. Gross and Srawley [42] gave a linear solution for K_I :

$$\frac{K_I B \sqrt{H}}{P} = 3.46 \frac{a}{H} + 2.38 \quad (5)$$

The validity range was given as $\frac{W}{H} \geq \frac{a}{H} + 2$ and $\frac{a}{H} > 2$. Foote and Buchwald [39] derived an approximate formula for K_I for all values of a/H:

$$\frac{K \sqrt{H}}{P} = \sqrt{12} \left(\frac{a}{H} + 0.673 \right) + \sqrt{\frac{2H}{\pi a}} - (0.815 \left(\frac{a}{H} \right)^{0.619} + 0.429)^{-1} \quad (6)$$

with the same validity restrictions as equation 5.

However, DCB specimens used in this work had a W/H ratio of 3.3 and 2.8 for constant deflection and constant load, respectively. Longer cracks will thus be outside the given validity range and an unique calibration of K_I is necessary to obtain exact values. Own compliance measurements were done to confirm and eventually extend the validity range of existing calibrations. A simulated crack was achieved through a 0.3 mm saw cut. The measured compliances at different crack lengths were then fitted to a polynomial and K_I could be derived according to equation 3. Comparison of the resulting stress intensity factor, in non-dimensional terms, is shown in figure 13, together with literature data. For higher resolution, relative deviation from own results is plotted in Figure 14.

Data from Srawley and Gross [42], Mostovoy et al [38] and Foote/Buchwald [39] is based on theoretical K values while Stellwag/Kaesche [41] used the compliance method on a specimen with a W/H ratio of 2.538 compared to 2.83 of the specimen of this work.

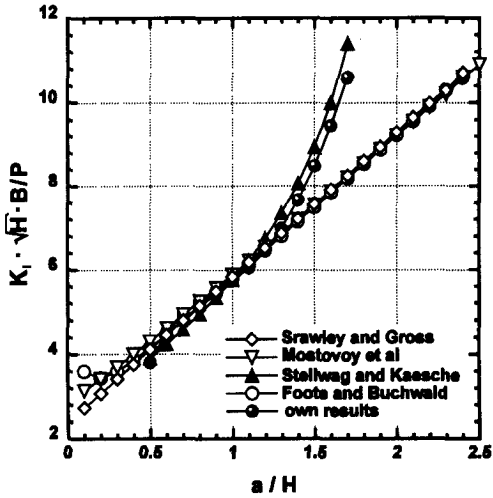


Fig. 13: Comparison between own results and literature data for dimensionless K-calibration curve of DCB specimen

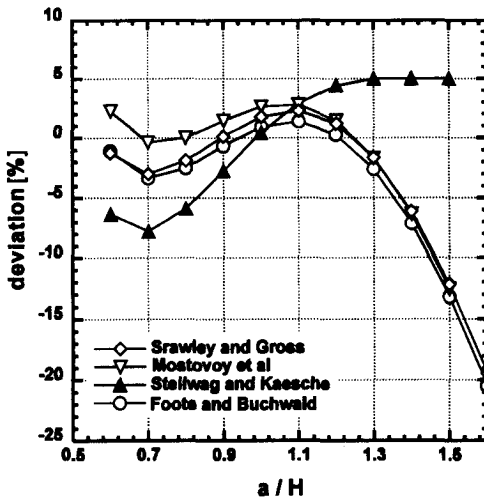


Fig. 14: Deviation of literature data from own results for dimensionless K calibration curves

As can be seen from figure 14, deviation from theoretical curves remains small up to a a/H ratio of about 1.3 and the simple equation 5 can be used for calculation of the stress intensity K_I from the crack length a and the applied load P .

For calculations on wedge loaded specimens, a relation between crack opening displacement and stress intensity can be determined by integrating equation 4 for the different K-calibration formulas. Comparison of the non-dimensional term $\frac{K_I \sqrt{H}}{E \cdot \delta}$ vs. a/H ratio between own results and literature mentioned above is shown in figure 15 while relative deviation to own results is plotted in figure 16.

Again, deviations up to a a/H ratio of about 1.3 seem to be acceptable, remaining in the range $\pm 5\%$ within the theoretical values.

As a result of the measurements it can be stated that the validity range $a/H > 2$ is too conservative and formulas can be used down to a ratio of 0.5. For $a/H > 1.3$, stress intensities derived from theoretical calibration data are too low for both constant load and constant deflection for the given specimen geometry. As long as crack lengths were within the derived validity range, stress intensities of wedge loaded specimens investigated in this work were calculated with equation 5 and the easy to handle expression of Mostovoy et al. as given in the following equation:

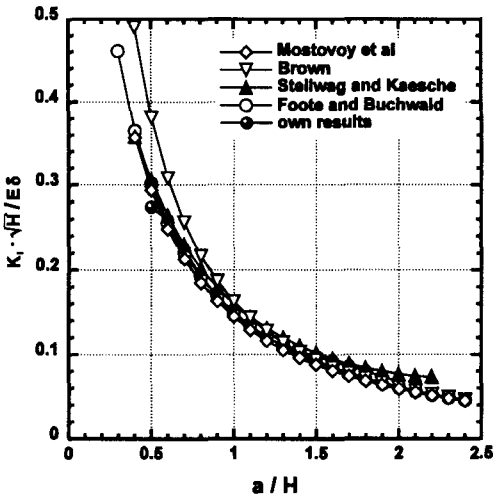


Fig. 15: Comparison between own results and literature data for dimensionless K-calibration curve of DCB specimen

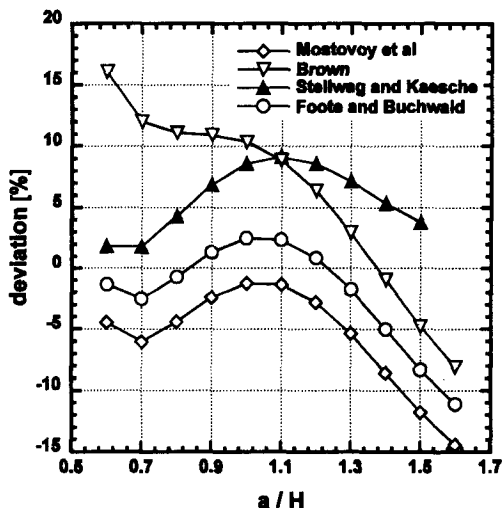


Fig. 16: Deviation of literature data from own results for dimensionless K calibration curves

$$K_I = \frac{E \cdot \delta \cdot H \left[3H(a + 0.6H)^2 + H^3 \right]^{1/2}}{4 \left[(a + 0.6H)^3 + H^2 a \right]} \quad (7)$$

4.3.2. Crack length determination

Stress corrosion cracks often trail near the specimen surface resulting in a thumb nail shaped crack front. For wedge-loaded specimens with a stress corrosion crack, simply the maximum penetration distance was taken as the crack length to determine the resulting growth rate.

The two constant load autoclaves with lead-through arms allowed for in situ crack growth rate measurement. To transform the crack opening displacement signal from the extensometers to a crack length, a compliance calibration curve of the actual specimen

must be known. As described above, compliance was measured as a function of crack length and the following polynomial form was taken to fit the data:

$$\frac{a}{H} = A_0 + A_1U + A_2U^2 + A_3U^3 + A_4U^4 + A_5U^5 \quad (8)$$

U is a function of the normalized compliance:

$$U = \frac{1}{(\text{BEC})^{0.5} + 1} \quad (9)$$

C is equivalent to δ/P where δ is the crack opening displacement at the load line and P the total load.

The coefficients were obtained by least square regression analysis and are given as follows:

| | |
|---------|------------|
| A_0 : | 4.3368 |
| A_1 : | -57.9683 |
| A_2 : | 504.6188 |
| A_3 : | -3045.0705 |
| A_4 : | 10355.599 |
| A_5 : | -14343.603 |

To determine a crack growth rate from the recorded load line deflection vs. time curve, the following algorithm was used:

- At the beginning of crack growth measurement, a starting value for the load line deflection had to be calculated from load, specimen thickness and Young's modulus. Equation 8 must be used in an iteration process by changing δ until a/H has reached the right value. This task was accomplished with a small computer program integrated as a makro in a spreadsheet program.
- Since load line deflection data had to be taken graphically from the printer output, only one point every eight hours was selected and tabulated. A measured difference is then added to the initial δ and introduced into equation 8 to get a new crack length a .

The last step, determination of crack growth rate as a function of time, requires a monotonic crack length vs. time curve in a form where the first derivative can easily be calculated. For further treatment, data was therefore separated into appropriate overlapping intervals and fitted to a polynomial. When crack growth rate changed within a short time, polynomials gave no satisfying approximation and a smoothing spline was used in these cases. An own computer program was written for these calculations. To

illustrate the fitting procedure, figure 17 shows measured crack length values from an experiment conducted at 240°C. Crack length scatter is about ± 0.05 mm as estimated from the plot. Two different polynomials were fitted in the given time interval, one 4th order polynomial and a linear regression line restricted to the flat region. The first derivative of these lines is the crack growth rate and is plotted in the same diagram. Choice of the appropriate regression function was done arbitrarily, giving very similar results when crack growth rate was higher than about $1\text{E-}9$ m/s. For the given example, it was difficult to decide whether the crack was still growing in the flat region since the derivative of the 4th order polynomial showed even negative values and the linear regression showed a slope of only $1.4\text{E-}11$ m/s. Due to the limited accuracy, crack growth rates derived from regression analysis were only plotted for values greater than $1\text{E-}10$ m/s. The incidence of lower crack growth rates which are maintained within an extended period of time can thus not be ruled out.

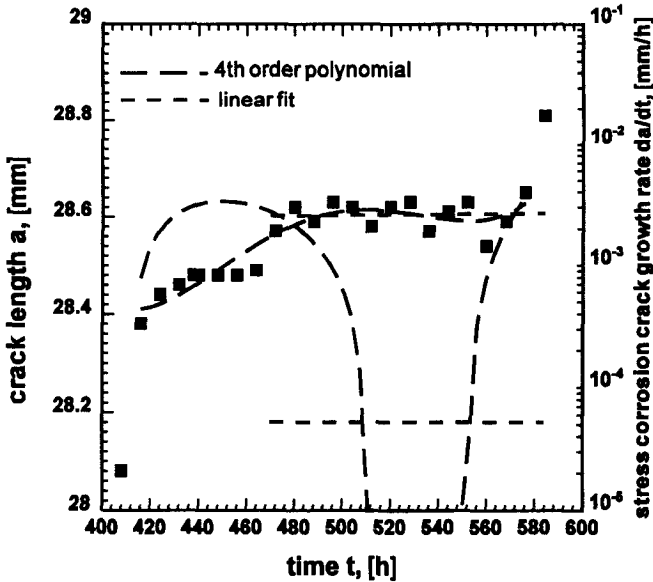


Fig. 17: Example of measured crack length data and regression polynomials for calculation of crack growth rate

4.4. Measurement of the electrochemical potential

Electromotive forces (emf) are measured as voltage differences between two electrodes on which oxidation and reduction processes are taking place simultaneously. Separation of the cell into half-cells makes it possible to state single potentials of individual electrode reactions. However, a suitable reference half-cell must be determined to have a well defined reference point. The customary convention is to define the Gibbs free energy of the formation of hydrogen ions in a hypothetical solution of activity one at one atmosphere hydrogen pressure to be zero at all temperatures. This half-cell is known as the *standard hydrogen electrode* (SHE).

However, for high temperature studies the hydrogen electrode is often inconvenient because of difficulties in exactly measuring hydrogen partial pressure in the system. Moreover, this electrode can only be used in a static system with a liquid-gas interface. Instead, metal/metal salt electrodes are used in practice. Then, the potential is a definite function of the anion concentration and the solid compound $(Me^{z+})_s \cdot (A^{y-})_s$ which builds an adherent layer on the metal. A reference electrode which is widely used in room temperature applications is based on the Ag/AgCl couple in contact with a potassium chloride solution. This type of electrode has also proven to be one of the most reliable electrodes for high temperature electrochemical applications. In the KCl system, the transference numbers of the potassium and the chloride ion are almost identical so that liquid junction potentials arising from large concentration gradients can be neglected. The cell potential given by the Nernst equation is only dependent on the activity of potassium chloride at a fixed temperature and may be used in polluted environments provided that the electrode is shielded properly from the surrounding electrolyte [47].

Several designs of Ag/AgCl reference electrodes for use in high temperature/pressure environments have been described in literature [44-47]. Two distinctive variants are popular: One, the *isothermal type*, operates entirely at the temperature and pressure of the environment being monitored. The other, the *thermal junction type*, operates with a thermal junction across the electrolyte bridge, and the reference couple itself is kept at room temperature.

Roughly following the design of the external reference electrode described by Andresen [46], a new electrode for use in static autoclaves was built. The decision to use an external reference was based on several advantages over internal reference electrodes.

Some of them are listed below:

- The high pressure seal remains cool so that sealing material and construction is not a

problem.

- The required space in the pressure vessel can be restricted to the lead-in salt bridge tube.
- Only a portion of the electrode is exposed to high temperatures. Thus, gas bubble formation is small.
- Volume changes by thermal expansion of the electrolyte are restricted to the hot part, so that dilution can be minimized.

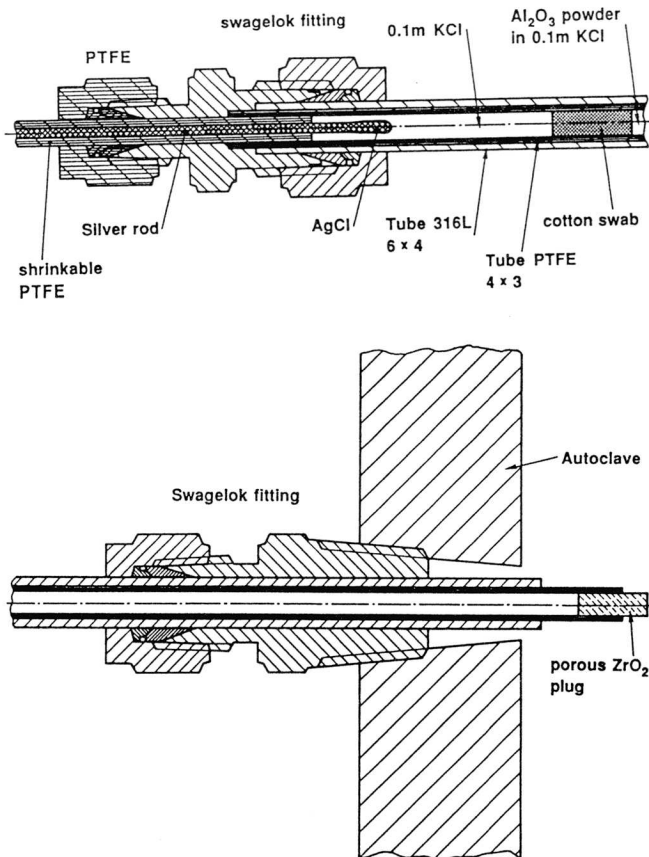


Fig. 18: Drawing of an external reference electrode designed for potential measurements in static autoclaves at temperatures up to 300°C

Figure 18 shows a drawing of the external type electrode built by the author and used in high temperature potential measurements.

Sealing was done with standard Swagelok[®] fittings and heat shrinkable PTFE. AgCl was applied on a pure silver wire by dipping the hot wire into AgCl powder whose melting point is around 455 °C. Alumina powder of -90 +45 microns in 0.1 m KCl solution was used as internal solution bridge. The zirconia plug was cut from porous plate material.

A disadvantage of the external type reference electrode is the non reversible thermal junction potential which arises from the thermal gradient in the solution bridge. Therefore, the behaviour is non thermodynamic, but the couple still works as a quasi-reference electrode if properly calibrated vs. a known standard. The calibration procedure will serve to relate measured electromotive forces to the standard hydrogen electrode (SHE):

$$\Delta E_{\text{SHE}}(T) = \Delta E_{\text{MEAS}} + E_{\text{Ag/AgCl}}(T) - \Delta E_{\text{TH}} \quad (10)$$

| | |
|--------------------------|---|
| ΔE_{SHE} | Potential of working electrode vs. the standard hydrogen electrode |
| ΔE_{MEAS} | Potential of working electrode vs. the reference electrode |
| $E_{\text{Ag/AgCl}}$ | isothermal potential of the silver/silver-chloride electrode vs. SHE at temperature T |
| ΔE_{TH} | Thermal liquid junction potential and EMF of the thermal cell: |



The thermal liquid junction potential can be split into two terms:

$$\begin{aligned} \Delta E_{\text{TH}} &= E_{\text{Ag/AgCl}}(T) - E_{\text{Ag/AgCl}}(T_0) + && \text{Thermocell potential} \\ E_{\text{S}}(T) - E_{\text{S}}(T_0) &&& \text{Thermal liquid} \\ &&& \text{junction potential} \\ &&& \text{(TLJP)} \end{aligned}$$

In the above equation, isothermal liquid junction potentials (due to diffusion) and the Thompson effect on metallic silver are neglected because their contribution remains small compared to the TLJP. Literature data of measured ΔE_{TH} was available from two

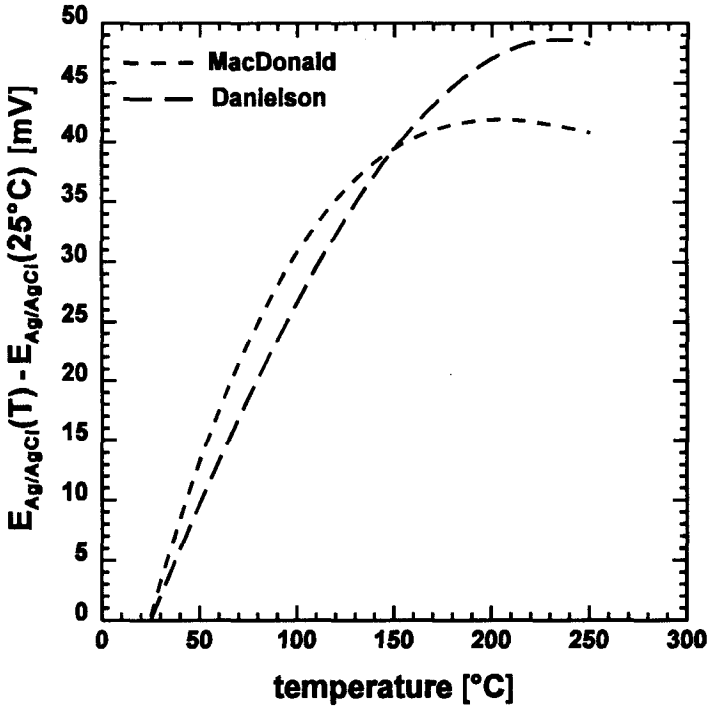


Fig. 19: Thermal liquid junction potential $E_s(T) - E_s(T_0)$

sources [45,48] and is shown in figure 19. The data agree well, however, the maximum temperature at which measurements were carried out was 250°C and values given at higher temperatures had to be extrapolated.

To get $\Delta E_{SHE}(T)$ of equation (10) the potential $E_{Ag/AgCl}(T)$ of the silver-silver chloride electrode at the temperature T must be known. Greeley et al. [50] measured the electromotive force of the cell $Pt/H_2/HCl(m)/AgCl/Ag$ at temperatures from 25 to 275 °C and determined the standard potential of the $Ag/AgCl$ electrode.

The electromotive force E of the cell used by Greeley can be expressed as:

$$E = E^0 - \frac{RT}{F} \ln \gamma_{\pm}^2 m^2 \quad (11)$$

where γ_{\pm} is the mean activity coefficient for HCL and m is the mean molality of H^+ and Cl^- ($m = \sqrt{m_{H^+} \cdot m_{Cl^-}}$). E^0 is the standard potential. The term $\frac{RT}{F} \ln \gamma_{\pm}^2 m^2$ reflects the

deviation from an ideal 1 molal solution. To get standard conditions for the hydrogen electrode, the activity of H^+ must be corrected to one. Since $m_{H^+} \approx m_{Cl^-}$ in a HCl solution and assuming that $\gamma_{\pm}(HCl) = \gamma_{\pm}(KCl)$, the correction term $\frac{RT}{F} \ln(\gamma_{\pm}m)$ is simply given by $\frac{E - E^0}{2}$.

$E_{Ag/AgCl}$ may directly be used to relate measurements vs. a high temperature inner Ag/AgCl reference electrode to the standard hydrogen electrode. $E_{Ag/AgCl}(T) - \Delta E_{TH}$ then refers to the potential of a pressure balanced external reference electrode when the reference system is at room temperature. These potentials are plotted in figure 20 for the case of a 0.1 M KCl electrolyte.

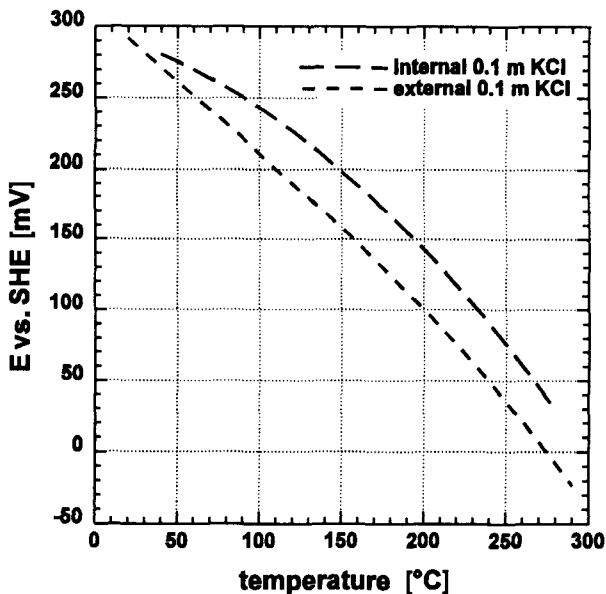


Fig. 20: Potential of an internal and external Ag/AgCl reference electrode vs. SHE

4.5. Oxygen concentration in the water

In a static autoclave, the system pressure is maintained by the sum of the water vapour pressure at the given temperature and the partial pressure of the gas bubbling through the water. The composition of the gas can be chosen to give a preset equilibrium concentration in the high temperature water in the test vessel. Convective flow caused by the heating elements inside the vessel ensures a fast equilibrium restoration with the gas cushion. Data about gas solubilities in high temperature water was taken from the literature [51-55]. Oxygen concentration was calculated according to an expression evaluated by Clever [55], who fitted measured mole fractions to an appropriate function of the temperature. The final expression is given as follows:

$$[O_2] = \frac{X_{O_2} M_{O_2}}{M_{O_2} X_{O_2} + M_{H_2O} (1 - X_{O_2})} \cdot \frac{Y_{O_2} (P - P_{H_2O})}{1.01325} \quad (12)$$

$$X_{O_2} = \exp(-54.0411 + 68.8961/(T/100) + 18.5541 \cdot \ln(T/100)) \quad (13)$$

where:

| | |
|------------------------|--|
| $[O_2]$ | oxygen concentration as a weight fraction |
| X_{O_2} | mole fraction of oxygen in the water at 1 atm partial pressure |
| M_{O_2} , M_{H_2O} | molar weight of oxygen and water |
| Y_{O_2} | mole fraction of oxygen in the gas |
| P , P_{H_2O} | total system pressure and water vapour pressure |
| T | absolute temperature |

Calculations are made with the assumption that Henry's law is valid if the partial pressure is kept low. This is certainly true for the gas compositions used in this work, where oxygen concentrations ranged from 300 ppm to 1.2 % (main part was argon).

A lot of experiments were conducted with several changes from one gas mixture to another, with the intention to slowly alter the electrochemical potential of the specimen. It was seen, that oxygen concentration in the water can be estimated by measuring the gas flow rate through the autoclave. The following equation was derived:

$$C = C_2 + (C_1 - C_2) \exp\left(-\frac{V_2}{V_1}\right) \quad (14)$$

where C is the actual concentration, C_1 and C_2 are the equilibrium concentrations of gas mixture 1 and 2 respectively when gas is changed from 1 to 2. V_1 is the total normalized

volume of the gas in the autoclave. This volume was estimated by a hot part in the autoclave and a cold part in the tube leading to the pressure and needle valves. Normalization was done to the temperature of the escaping gas. V_2 is then the volume of the escaped gas during the elapsed time since the change of the gas mixture. Equation 14 is valid with the assumption that oxygen concentration is always in equilibrium with the overlaying gaseous atmosphere and the latter having the same oxygen content all over the pressurized volume.

5. Results

5.1. Free corrosion potential

The corrosion potential is believed to play an important role in determining the rate of environmentally assisted cracking in high temperature water. The actual value measured vs. a reference electrode is always a mixed potential resulting from oxidation and reduction reactions which take place at the same location at a conducting electrode surface. The reaction system may consist of a metal surface and an electrolyte such as high purity water in the present case. Possible reactions comprise the electrode itself (e.g. dissolution $Me \rightarrow Me^{2+} + e^-$) and redox processes involving water and dissolved molecules.

In Boiling Water Reactors a considerable concentration of oxygen and hydrogen peroxide are maintained by radiolysis of the water circulating through the core region, especially during start-up. These species are known to have a very strong influence on the corrosion potential of reactor materials like stainless and low alloy steel.

There exists a wide data basis on electrochemical potentials of BWR-structural materials in high temperature water as a function of the dissolved oxygen content. The strong influence of hydrogen peroxide is not established so well, because of experimental difficulties to exactly measure the concentration. Figure 21 shows scatterbands of measured corrosion potentials as a function of the dissolved oxygen concentration in stagnant and quasi-stagnant deionized water as well as literature data for austenitic steels, low alloy steels (own measurements in static and refreshed autoclaves) and titanium. Literature data for type 304/316 stainless steel and RPV steel is plotted as scatterbands [59-66]. Apart from the fact that the data scatter is relatively large, some general trends can be observed. The relation between corrosion potential and oxygen concentration appears as a S-shape curve for low alloy steels and titanium. During tests with decreasing oxygen concentrations, it was observed that the steep transition from high to low potentials moves to lower oxygen concentrations when the temperature is lowered from about 290 °C to 200 °C. Moreover, potentials vs. SHE at the same nominal oxygen concentration in the upper part of the curve are higher for lower temperatures. These results agree with published data [68] and may be important discussing the susceptibility to SCC at different temperatures as a function of the oxygen concentration in the water.

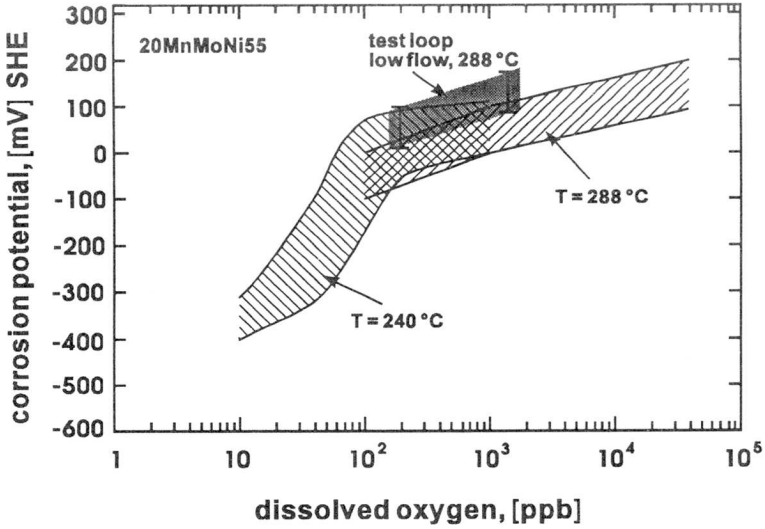


Fig. 21a: Free corrosion potential of RPV steels as a function of the dissolved oxygen concentration

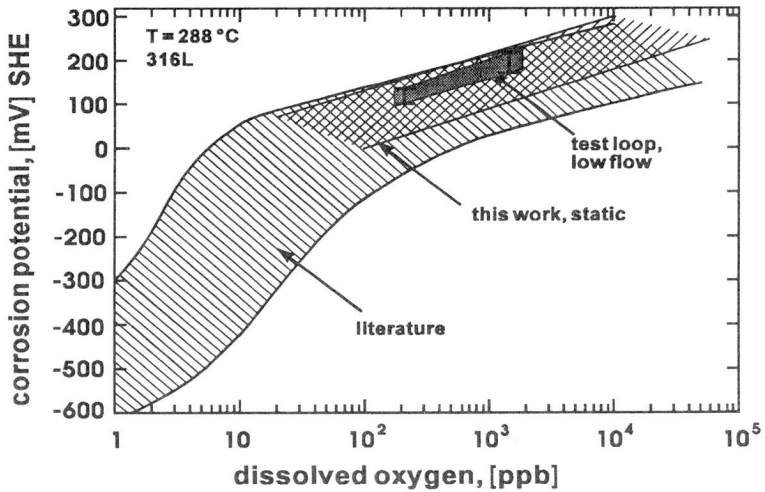


Fig. 21b: Free corrosion potential of stainless steel 316L and 304 as a function of the dissolved oxygen concentration

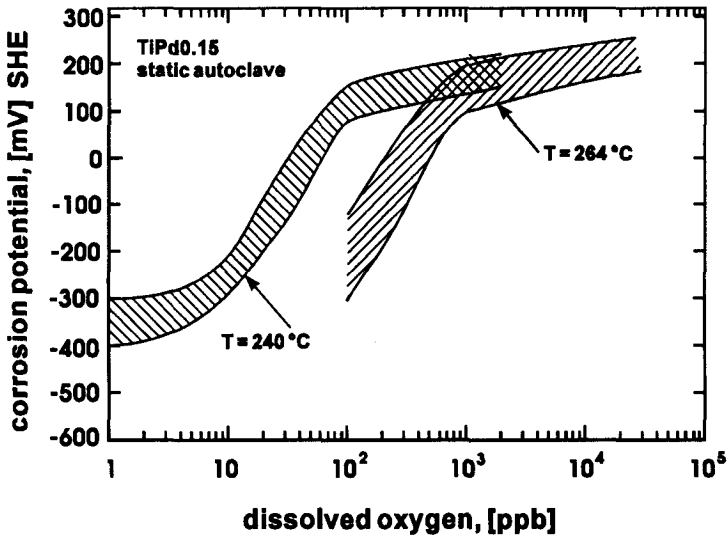


Fig. 21c: Free corrosion potential of Ti0.15Pd as a function of the dissolved oxygen concentration

The stainless steel autoclave behaved quite sluggish when the oxygen concentration was lowered continuously and an abrupt drop could not be observed down to very low oxygen concentrations. It's not believed that oxide formation at high potentials is irreversible in stainless steels, but equilibrium restoration can be very slow.

Reasons for the different behaviour of stainless and low alloy steels can be found in the composition, the structure and the thermodynamic stability of the oxide layers. Also, the exchange current density for redox reactions will depend on the oxide surface structure and composition. At low corrosion potentials, measurements indicate that oxide layers are slowly reduced and thus some oxygen is steadily released, retarding the reduction process. Titanium seems to be a more favourable (but expensive) material for test autoclaves when low potentials must be reached within short times.

The electrochemical potential of the autoclave material is important because in most of the tests, specimens were not insulated in the grips of the loading frame. It turned out that both stainless steel 316L and titanium always have a higher electrochemical potential than the low alloy steel specimen. At a high oxygen concentration, the difference is about 100 mV in stagnant water at 288 °C.

Insulation of the specimen is difficult under the high loads acting upon the bolts in the clevis. In order to get insulated bolts, a thin zirconium alloy tube (Zr2.5Nb) was pressed over a high strength Nimonic alloy bolt after oxidising at 550 to 570 °C for several hours to build a dense ZrO₂ layer. However, the moderate strength of zirconium alloys does not permit to use full bolts. Due to plastic deformation of the zirconium tube, resistance between autoclave and specimen was often not as high as desirable for an effective galvanic separation.

In the case of non-insulated specimens, it was assumed that the measured potential is mainly fixed by the autoclave material because of the much larger surface area. Conductivity at the test temperatures is expected to be high enough to prevent large potential differences between locations at the clevis and the lower end of the specimen. No contact corrosion problems have occurred in this context.

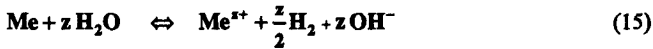
The wide scatter in the corrosion potentials plotted in figure 21 implies that knowledge of the nominal oxygen concentration in the water is not sufficient to clearly determine the resulting electrochemical potential. For a closer look at the parameters which determine the corrosion potential, basic principles of electrochemistry based on the concept of mixed potential can be helpful. These principles assume that the electrochemical reduction and oxidation currents at a metal surface can be treated separately. The measured current density at a certain electrode potential can then be taken as the sum of an anodic and a cathodic current density branch and the corresponding potential is thus defined as a mixed potential. At open circuit conditions, without a potential gradient in the electrolyte, the cathodic and anodic current density match exactly and the corresponding potential can easily be identified if the shape of the single current branches is known. However, potentiodynamic polarization curves are difficult to measure in high purity water because of the low conductivity and the associated iR potential drop between the specimen and the reference electrode. Published data is often based on molybdate [71] or sulfate solutions [72], the latter indicating primary passivation of a carbon steel at temperatures above 175°C. The passivating film exists as a comparatively thick duplex film which effectively protects against fast corrosion attack in high temperature water plants as long as pitting doesn't take place. The passive current density can be measured by gravimetric analysis. It must be considered that the weight loss is strongly dependent on the immersion time [56], since the corrosion process is controlled by transport processes in the inner oxide layer.

The current density of the redox reactions depend on the exchange current density, the polarization characteristics and the limiting mass transfer rates through a diffusion layer at the steel surface. Attempts have been made to model the system for special cases [57,58].

A qualitative discussion of the effect of oxygen on the corrosion potential will be given as follows:

As shown in figure 22, the anodic polarization curve for the electrode is given in its typical shape for passivating metals. As an oxidizing species, only oxygen will be considered.

Starting with a fresh electrode surface at very low oxygen concentrations in pure water, the hydrogen/water reaction controls the electrochemical potential. The corrosion potential is kept in the active part of the anodic polarization curve of the specimen through the reaction



A part of the metal ions hydrolyze to soluble and insoluble products. On low alloy steel, a magnetite (Fe_3O_4) layer is built [67].

Of particular interest for BWR applications is the intermediate corrosion potential region where the critical potential for SCC is often located. By assuming negligible hydrogen concentrations, the important reactions comprise basically the oxidation of the metal electrode and the O_2 redox reaction



The change of the corrosion potential with rising oxygen concentration is shown schematically in figure 22. At a low oxygen concentration, the corrosion rate of the metal electrode is given by the maximum diffusion limited current density of the above redox reaction caused by a concentration gradient from the surface to the bulk solution. The concept of a boundary layer assigns control of the transport process to a thin portion of the electrolyte adjacent to the electrode surface. The thickness of this diffusion layer can be related to a hydrodynamic boundary layer which depends on the water flow rate in the system [70]. Expressions between limiting current density and water flow rate can be derived for well defined flow conditions [62,73].

The important conclusion which can be drawn from mass transfer considerations is that flow rate is nearly as important as the bulk oxidant concentration in this intermediate range of oxygen concentration. Comparison between flowrates of 10 l/h and 100 l/h in the refreshed water loop revealed that the corrosion potential of the pressure vessel steel is raised by about 50 mV and is then about equal (within 20 mV) to the stainless steel autoclave potential. Because of the large number of specimens in a test autoclave, true flow rates or Reynolds numbers cannot be given but the data indicates that the change in

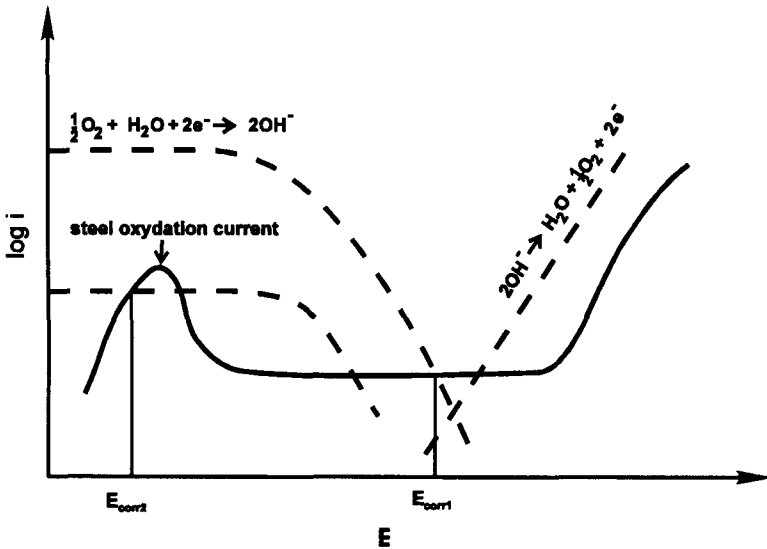


Fig. 22: Schematic E vs. log I diagram showing the interactions of a redox reaction and a steel polarization curve

the corrosion potential can be pronounced within a range of flow rates usually specified as 'quasi-stagnant'.

Besides the flow rate, also the total time of exposure to oxygenated high temperature water can have a strong effect when film free specimens are used at the beginning of an experiment. In up/down scans a hysteresis loop can appear because of a non-equilibrium state in the structure and the composition of the oxide layer. Figure 23 illustrates the behaviour of the corrosion potential of pressure vessel steel samples at 290 °C, when oxygen concentration was changed consecutively between low, medium, and high values. The numbers designate the chronological order between the measurements. The potential is higher the longer the test duration and saturates after about one week.

At medium to high oxygen concentrations, the corrosion potential is determined by the O_2 reduction current and the passive current density of the specimen. If the exchange current density of the redox couple O_2/OH^- is high or if some hydrogen is present, the corrosion potential may be completely controlled by redox processes on the specimen surface. In the high oxygen regime, the slope of the E vs. $\log[O_2]$ curve is approximately linear and was between 50 and 65 mV per decade in the static autoclaves. On the other

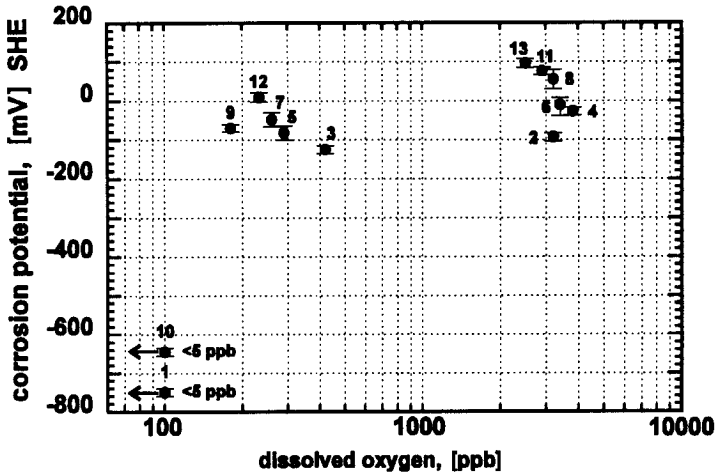


Fig. 23: Corrosion potential of RPV steel samples in deionized water at 290 °C during a one week period with several changes in the dissolved oxygen concentration as given by the numbers in their chronological order.

hand, in the refreshed systems, a higher slope of about 100 mV per decade was measured in agreement with published values [64,66].

5.2. Refreshed autoclaves

Only refreshed autoclave systems offer the possibility to measure and control the important environmental system parameters like oxygen concentration, conductivity and flow rate. The available equipment was designed to allow laboratory simulation of light water reactor (LWR) environment to evaluate possible SCC susceptibility of reactor materials.

Investigations accomplished in the refreshed water loop at the Paul Scherrer Institute were specifically aimed to achieve reliable results in a typical BWR environment. A dissolved oxygen concentration of 200 ppb and a room temperature conductivity of less than 0.3 $\mu\text{S}/\text{cm}$ is the commonly used test specification to represent the water conditions within the pressure vessel. The water flow rate is an additional important factor which is not specified but should certainly be controlled in the testing procedure.

5.2.1. Test conditions

Until completion of this work, seventeen testruns with wedge loaded DCB specimens in the recirculated water loop were accomplished. The environmental test parameters are listed in table 5. The given values for oxygen concentration and conductivity were kept constant within a scatterband of $\pm 10\%$ during the chosen test duration. Adjustment of both values was done with the outlet water.

At the end of each test, all specimens were dried and examined at the surface ahead of the fatigue crack for visible crack growth. Moreover, the load line displacement was measured to detect creeping or loosening of the wedge. Usually, after-test displacement was a little smaller (up to about 5%) than that measured immediately after the loading procedure before the test, which indicates some relaxation of the load.

When crack growth was detected at the surface, a new fatigue crack was induced, in order to mark the tip of the stress corrosion crack. The specimens were then broken open. Alternatively, specimens were cooled in liquid nitrogen and then broken open. The maximum stress corrosion crack length on the fracture surface was always taken as the relevant parameter for determination of the crack growth rate since the stress corrosion crack front tends to be thumb nail shaped in 10 mm DCB specimens.

In several cases SCC took place but was not yet visible at the outside due to the thumb nail shaped crack. These specimens could be identified by slightly enhanced load line displacements measured between the side faces. The slight difference arises from elastic deformations changing with crack length, while displacement at the wedge itself remains constant.

Specimens without indication for SCC were treated in one of the following ways and were then reused for the next test:

- New fatigue crack several mm ahead of the old one with a final K_{\max} lower than that in the following test.
- Increase of K_I by 8 % or more by increasing the wedging force at the notch.

Thus, all specimens were either newly precracked or loaded to a higher stress intensity before starting a new experiment, the latter being applied preferentially. An exception was test 5, where the specimens were immediately reused after completion of the test and a visual inspection. Following test 4, all specimens were broken open and a new set of specimens was prepared. The detailed procedure for all specimens is given in table I in the annex.

The experimental sequence started with an oxygen content of 0.2 ppm at outlet and a conductivity of 0.3 $\mu\text{S}/\text{cm}$ to simulate typical BWR water with the maximum allowable

| test number | number of specimens | oxygen content ¹⁾ [ppm] | conductivity ²⁾ [μ S/cm] | flow rate [l/h] | pressure [bar] | temperature [°C] | test duration [h] |
|-------------|---------------------|---------------------------------------|---|--------------------|-------------------|---------------------|----------------------|
| 1 | 15 | 0.2 | 0.3 | 100 | 110 | 288 | 700 |
| 2 | 15 | 0.2 | 0.3 | 20 | 110 | 288 | 1000 |
| 3 | 15 | 1.5 (2) | 0.3 | 20 | 110 | 288 | 1000 |
| 4 | 15 | 1.5 (2) | 1.0 | 20 | 110 | 288 | 1000 |
| 5 | 15 / 15 | 1.5 (2) | 1.0 | 10 | 110 | 288 | 1000 |
| 6 | 15 / 15 | 1.5 (2) | 1.0 | 10 | 110 | 288 | 1000 |
| 7 | 15 / 1 | 1.5 (2) | 1.0 | 10 | 110 | 288 | 1000 |
| 8 | 11 / 15 | 1.5 (2) | 1.0 | 10 | 110 | 288 | 1000 |
| 9 | 15 / 15 | 1.5 (2) | 1.0 | 10 | 110 | 288 | 400 |
| 10 | 15 / 15 | 1.5 (2) | 1.0 | 10 | 110 | 288 | 400 |
| 11 | 15 / 15 | 0.8 (1.1) | 1.0 | 10 | 110 | 288 | 400 |
| 12 | 15 / 15 | 0.4 (0.6) | 1.0 | 10 | 110 | 288 | 450 |
| 13 | 13 / 13 | 0.2 (0.35) | 1.0 | 10 | 110 | 288 | 580 |
| 14 | 15 / 15 | 0.2 (0.40) | 1.0 | 10 | 110 | 288 | 540 |
| 15 | 15 / 15 | 0.2 (0.34) | 1.0 | 10 | 110 | 288 | 920 |
| 16 | 15 / 15 | 0.4 (0.6) | 0.5 | 10 | 110 | 288 | 580 |
| 17 | 15 / 15 | 0.4 (0.6) | 0.5 | 10 | 110 | 288 | 620 |
| 18 | 15 / 15 | 0.4 (0.6) | 0.5 | 10 | 110 | 288 | 590 |

1): Measured at outlet. Inlet values in brackets

2): Measured at inlet

Tab. 5: Adjusted test parameters in the recirculated high pressure loop

conductivity under normal operating conditions according to EPRI guidelines [74]. The tests were initially aimed to clarify whether stress corrosion is possible in low alloy pressure vessel steels under these conditions. Since crack growth could not be detected in tests 1 and 2, it was decided to raise the oxygen concentration to 1.5 ppm in test 3. However, stress corrosion cracking did not happen in this test.

In order to promote stress corrosion cracking, the conductivity was finally enhanced to 1.0 μ S/cm for the further experiments. This conductivity was reached without adding chemicals to the water, due to corrosion products and KCl contamination from the reference electrodes. Upon reaching the specified conductivity, a constant value was then kept by adjusting the flow through the ionic exchanger .

Samples for chemical analysis of the process water were taken into 100 ml PE-bottles from test 9 on, about once a week. Two identical samples were analyzed in each case for control of reproducibility of the measurements. The results revealed that the main contribution of ionic impurities arose from KCl leakage of the reference electrodes, leading to the conductivity of $1\mu\text{S}/\text{cm}$ in tests 4 to 15. Measured chloride concentrations were always in excess of 50 ppb in these tests. Sulphate was detected in concentrations up to about 100 ppb in experiments 11 to 14, but identical water samples (two samples were taken at the same time) showed large scatter, so that some contamination during sampling or analysis cannot be ruled out. From test 15 on, water sampling was improved and another laboratory was chosen to do the chemical analysis. The results then showed consistent sulphate levels below 30 ppb in all samples. However, some sulphur may be liberated by dissolution of MnS inclusions, especially from fresh specimens.

5.2.2. Stress corrosion cracking results

A survey of the applied stress intensities and the appearance of crack growth in all tests so far conducted is plotted in figure 24. Closed symbols denote specimens with stress corrosion crack growth.

None of the 15 specimens of test 1 through 4 exhibited stress corrosion cracking. The chosen stress intensities were between 40 and $95 \text{ MPam}^{1/2}$. In these tests, only one of the two autoclaves was used. The total test duration for a single specimen was 3700 hours maximum. In test 1, a higher flow rate was achieved with a high pressure recirculating pump generating a water loop in the high temperature part of the facility. The pump failed after 700 h and the following tests were performed with a low refreshment rate of only 20 and 10 l/h respectively. The autoclave volume with assembled specimens is about 9 litres, giving quasi stagnant conditions for the low refreshment rates. Because of the low refreshment rate, the oxygen concentration at inlet and outlet differed somewhat as given in table 5.

The absence of any cracking in test 1 and 2 gave rise to a change of the test conditions. Literature data indicate that SCC of pressure vessel steel in clean BWR water is hardly observed in fracture mechanics specimens at constant load or constant deflection. However, the lack of any SCC results does not prove that environmental cracking is not possible at the nominal BWR oxygen concentration and conductivity. To investigate the susceptibility of pressure vessel steels for stress corrosion cracking, it's most promising to approach the supposed thresholds from a field where SCC is readily found. The

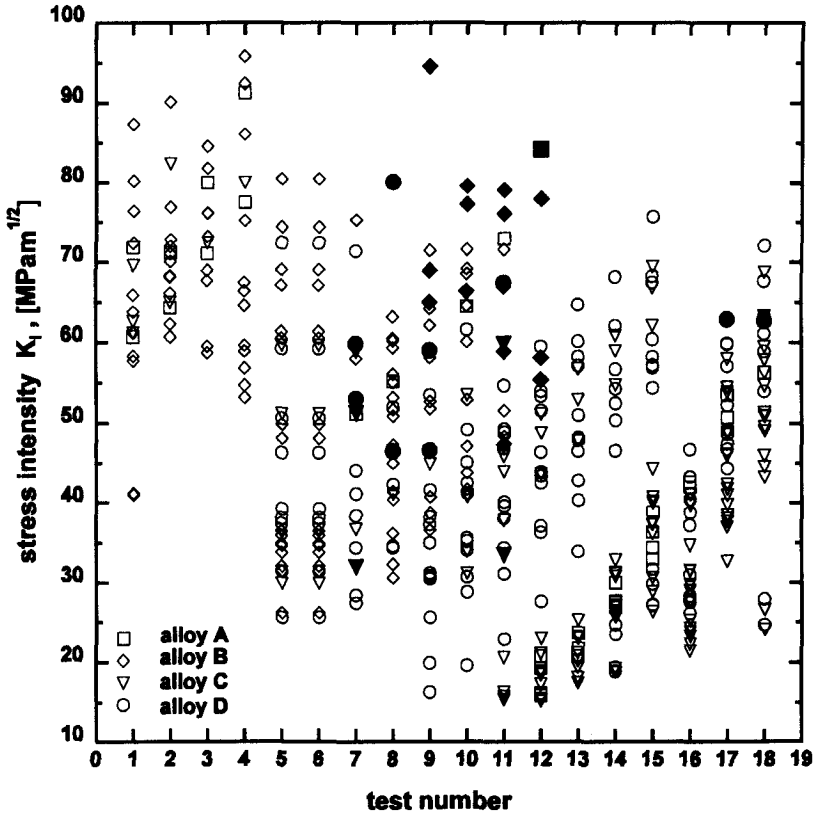


Fig. 24: Applied stress intensity values for tests 1 to 18. Filled symbols denote incidence of stress corrosion cracking

transition from SCC to non-SCC behaviour would then be a strong argument for a threshold behaviour of the investigated influential parameters.

Therefore, oxygen concentration was enhanced to 1.5 ppm in test 3. Since no cracking was detected, conductivity was also enhanced to $1 \mu\text{S}/\text{cm}$. These conditions were known to be sufficient to cause cracking in constant load test as measured in the static autoclaves. After completion of test 4, all specimens were broken open to check for stress corrosion cracking in the stereo microscope. However, there was no indication for crack growth in these specimens.

Steels exposed to 1.5 ppm dissolved oxygen in tests 3 and 4 were all of the low sulfur type (designation A and B) with exception of one specimen. A whole new set of 30

specimens (15 for each of the two autoclaves) was then prepared for tests 5 and 6, about half of them loaded to a stress intensity below $40 \text{ MPam}^{1/2}$. Also, steel with higher sulfur content (alloy D, ref. to table I) was introduced in the test. No crack growth could be detected after these two tests, with a total test duration of 2000 h. These specimens were then again prefatigued to a length of a few mm ahead of the old precrack.

Remarkably, in test 7, five or one third of all specimens (all taken from test 6 but with a new precrack) were found containing large stress corrosion cracks. In the same test, it was tried to keep a single specimen at a constant potential of 200 mV vs. the reference electrode in the second autoclave. A stainless steel sheet was used as the counter electrode. However, the potentiostatic control did not yield stable current densities with or without compensation of the ohmic potential drop. Crack growth could not be detected in this specimen. Since only one single specimen can be tested in potentiostatic mode and due to problems with the low water conductivity, this type of test was rejected for the further work.

In each of the following tests 8 to 12, several specimens showed long stress corrosion cracks. The cracked specimens were replaced by fresh ones loaded to a stress intensity below $30 \text{ MPam}^{1/2}$ to assure primarily preoxidation of the surface during the first test cycle.

Some of the measured stress corrosion crack lengths were about 20 mm. It can be argued that K_{ISCC} had been reached before the test end in these long cracks and the calculated crack growth rate is accordingly low. The duration of a test was thus lowered from 1000 to about 400 hours to improve the accuracy of the growth rate determination. A maximum crack growth rate of 1.6 E-8 m/s was then measured in test 9 and 11, a value which should come close to the true velocity, which is probably up to 3 E-8 m/s as was measured under constant load conditions.

All the crack lengths and crack growth rates measured at a conductivity of $1 \mu\text{S/cm}$ are summarized in table 6. Stress corrosion crack growth rates are plotted vs. stress intensity in figure 25 and correspond to the values given in table 6.

Stress corrosion crack growth rates lie roughly between 1E-9 and 2E-8 m/s in a plateau region, where growth velocities are independent of stress intensity. This is a typical result for medium strength low alloy steels in high temperature water [75]. The lowest stress intensity at which SCC initiated was $32 \text{ MPam}^{1/2}$. Most of the cracked specimens exhibited macrobranching from the beginning of SCC at an angle up to approximately 45° to the centre plane. Then, typically only one crack grew to its final length. A feature of the crack front in these specimens is that it tends to trail near the specimen surface. At the high stress intensities which were usually applied, there is a strong plastification ahead of the crack tip and the deformation becomes triaxial particularly near the surface.

| test number | material designation and orientation | stress intensity K_I [MPam ^{1/2}] | SCC crack length [mm] | da/dt [m/s] |
|-------------|--------------------------------------|--|--------------------------|----------------|
| 7 | alloy C TL | 32.0 | 4.7 | 1.3 E-9 |
| 7 | alloy C TL | 51.3 | 20.2 | 5.6 E-9 |
| 7 | alloy C TL | 59.0 | 16.9 | 4.7 E-9 |
| 7 | alloy D TL | 53.0 | 16.0 | 4.4 E-9 |
| 7 | alloy D TS | 59.8 | 3.8 | 1.1 E-9 |
| 8 | alloy D LS | 46.5 | 20.5 | 5.7 E-9 |
| 8 | alloy D SL | 80.1 | 8.5 | 2.4 E-9 |
| 9 | alloy B LT | 65.0 | 5.8 | 4.0 E-9 |
| 9 | alloy B LT | 69.0 | 4.6 | 3.2 E-9 |
| 9 | alloy B TL | 94.6 | 3.3 | 2.3 E-9 |
| 9 | alloy D ST | 46.6 | 8.2 | 5.6 E-9 |
| 9 | alloy D TL | 59.0 | 23.4 | 1.6 E-8 |
| 10 | alloy B TL | 79.6 | 8.5 | 5.9 E-9 |
| 10 | alloy B TL | 66.4 | 4.0 | 2.8 E-9 |
| 10 | alloy B TL | 77.3 | 5.3 | 3.7 E-9 |
| 11 | alloy B LT | 47.4 | 3.6 | 2.5E-9 |
| 11 | alloy B LT | 58.9 | 3.5 | 2.4e-9 |
| 11 | alloy B LT | 67.0 | 5.0 | 3.5E-9 |
| 11 | alloy B LT | 76.1 | 7.7 | 5.3E-9 |
| 11 | alloy B LT | 79.1 | 8.9 | 6.2E-9 |
| 11 | alloy C TL | 59.8 | 11.1 | 7.7E-9 |
| 11 | alloy C TL | 33.5 | 23.1 | 1.6E-8 |
| 11 | alloy D LT | 67.4 | 14.6 | 1.0E-8 |
| 12 | alloy B TL | 55.4 | 4.3 | 2.7E-9 |
| 12 | alloy B TL | 58.1 | 3.6 | 2.2E-9 |
| 12 | alloy B TL | 78.0 | 3.6 | 2.2E-9 |
| 12 | alloy A | 84.3 | 6.8 | 4.2E-9 |
| 17 | alloy D LT | 62.9 | 0.2 | 9.0E-11 |
| 18 | alloy D LT | 62.7 | 0.3 | 1.4E-10 |

Tab. 6: Specimens with stress corrosion crack growth in tests 7 to 18

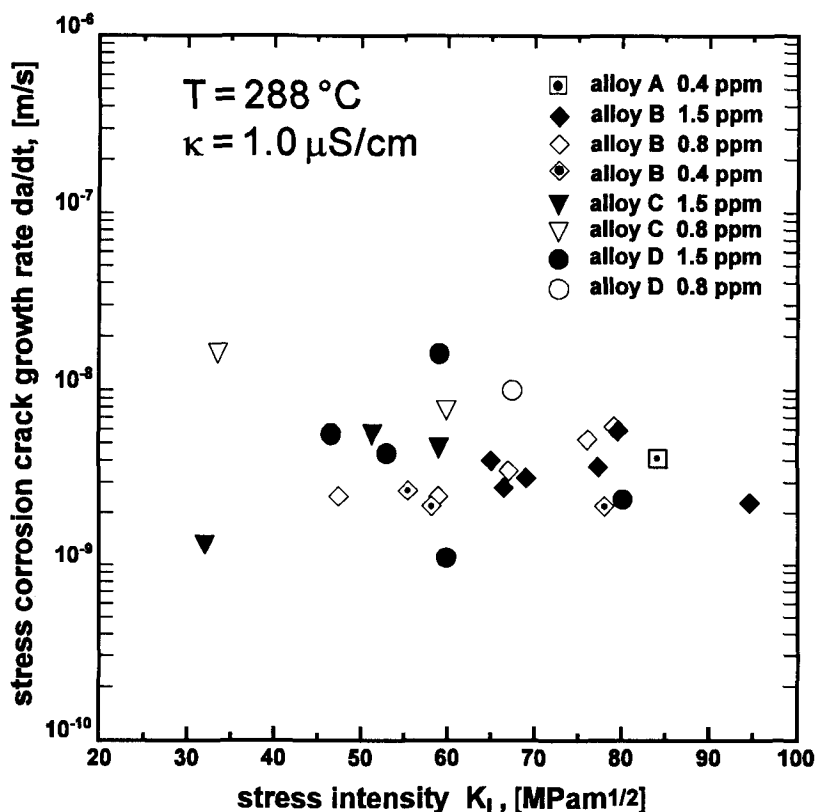


Fig. 25: Measured stress corrosion crack growth rates in pressure vessel steels in the high temperature water loop at 288 °C.

This effect seems to hinder the advance of the crack front. Figure 26 shows a transgranular stress corrosion surface from test 12 (alloy B) and figure 27 depicts a polished cross-section in the middle of a specimen with a stress corrosion crack. The initial stress intensity was 80 $\text{MPam}^{1/2}$. The crack path is clearly transgranular and several side branches spread out from the main crack indicating that crack growth is possible in an angular sector of about 90°.

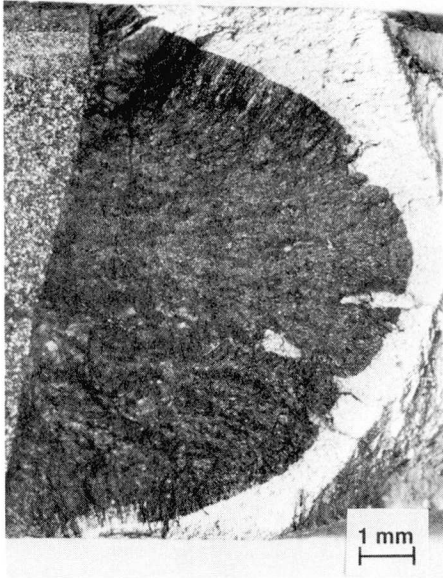


Fig. 26: Fracture surface of a specimen with a transgranular stress corrosion crack. Surface areas from left to right: precrack, SCC area, fatigue crack in air and final rupture

The width of the scatterband is at least in part given by the test procedure, where the crack growth rate is averaged over the whole test duration. A difference in crack growth rates within a factor of 2 or 3 will therefore disappear.

The standard formulas for the determination of the stress intensity are valid only for centre plane cracks. Only stress intensity values for the onset of stress corrosion cracking are therefore given in table 6. One specimen of alloy D had a crack plane inclination of only 15° with a stress corrosion crack length of 23.4 mm. Assuming a centre plane crack one gets a stress intensity of $32.8 \text{ MPam}^{1/2}$. This value is closely to $32 \text{ MPam}^{1/2}$, the lowest stress intensity SCC started. Therefore, the critical K_I level for stress corrosion crack growth, known as $K_{I\text{SCC}}$, may be around $30 \text{ MPam}^{1/2}$. This threshold agrees well with results published by Magdowski [75], who conducted similar tests in static autoclaves.

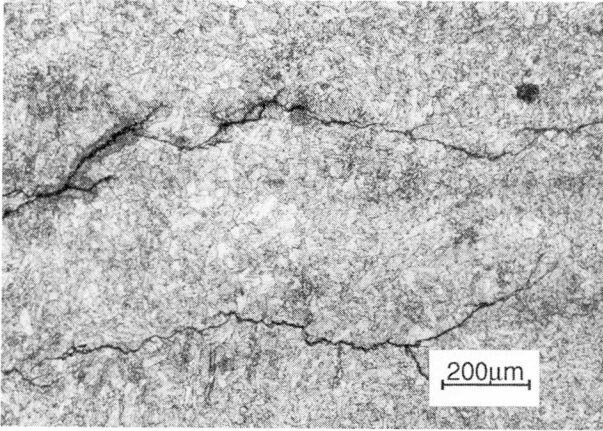


Fig. 27a: Transgranular stress corrosion crack in alloy D RPV steel. Initial stress intensity was $80 \text{ MPam}^{1/2}$. Crack path shows macrobranching

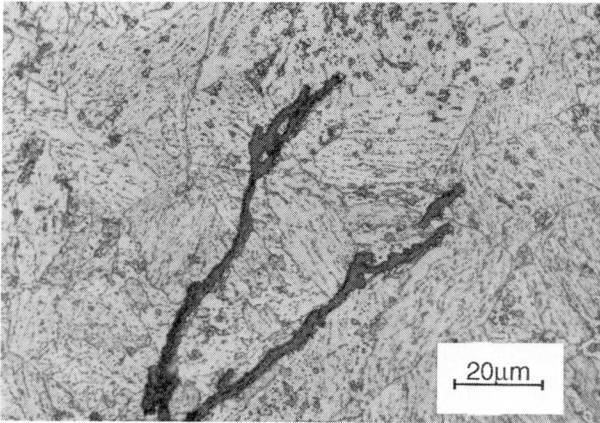


Fig. 27b: Detail of the crack tip. The width of the crack path is about 2 microns.

It's known that initiation of stress corrosion is not favoured by the method of wedge loading of fracture mechanics specimens. The portion of the specimens which exhibited crack growth in tests 7 to 12 was about 20 %, counting only those specimens with a stress intensity above $30 \text{ MPam}^{1/2}$. As a rough estimation, 4 out of 20 specimens crack on average and the probability that none of the specimens cracks is then only about 5% if a statistical normal distribution is assumed. However, statistical analysis is only valid if the environmental parameters are exactly the same for all specimens, which is doubtful, if one considers e.g. electrochemical potential and local water flow rate which may both vary within the autoclave.

Since susceptibility at 1500 ppb oxygen was now sufficiently verified, the next experiments were intended to evaluate the threshold oxygen concentration for SCC (with unchanged conductivity). At an oxygen concentration of 0.8 and 0.4 ppm, cracking was still observed in several specimens in all of the alloys. At 0.2 ppm oxygen however, cracking was absent in tests 13 to 15 according to the visual inspection at the sideface. To detect short stress corrosion cracks, 20 out of the 30 specimens (all specimens with a stress intensity exceeding $35 \text{ MPam}^{1/2}$) were broken open after test 15. For an assessment of possible stress corrosion cracking, the fatigue crack front was inspected in the stereo microscope. A stretched zone is normally seen at the transition from the original pre-fatigue crack to the final brittle fracture in liquid nitrogen. No signs of SCC initiation sites or other localized corrosion attack could be seen at all in this zone. Since detection accuracy is certainly better than about 0.1 mm, a steady state crack growth rate must be lower than $3 \cdot 10^{-11} \text{ m/s}$ or about 1 mm per year.

To illustrate the whole testing procedure up to that point, figure 28 outlines the 'working points' of oxygen concentration and conductivity in a diagram with hypothetical lines of constant crack growth rate. These lines predict the transition zone from crack growth to undetectable crack growth in terms of the dissolved oxygen content and the conductivity. Probably, conductivity should be split into individual concentrations of the single ion species since some of them may be involved in chemical reactions at the crack tip, others just help to lower the solution resistance which itself can have a strong effect. The given lines in figure 28 expand the area of susceptibility to lower conductivities for an increasing oxygen concentration.

To evaluate the effect of the water conductivity, a next series of tests was intended to be run at a lower conductivity and an oxygen content which proved to promote stress corrosion cracking.

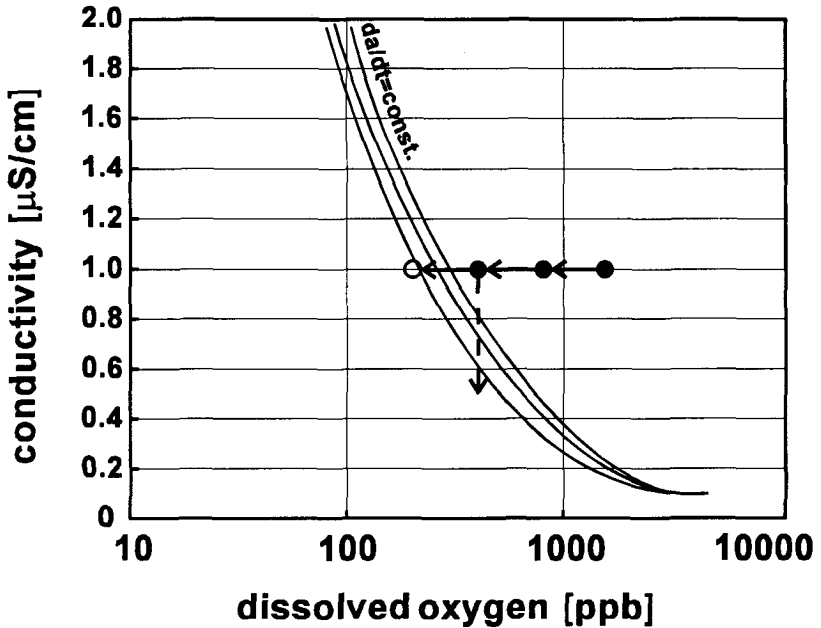


Fig. 28: Oxygen concentration and conductivity in tests 7 to 16 with a hypothetical plot of lines of constant crack growth rate

Therefore, test 16 was run with $0.5 \mu\text{S/cm}$ and 400 ppb oxygen, shown by the dashed arrow in figure 28. The visual inspection after the test revealed no sign of crack growth. The chosen stress intensities were quite low in this test, the highest value was $46.8 \text{ MPam}^{1/2}$ and 20 specimens were freshly introduced. A further test (nr. 17) was then conducted under the same conditions but with higher stress intensities (specimens from test 16). Four specimens were then broken open. That which the highest stress intensity of all specimens ($62.9 \text{ MPam}^{1/2}$) had a distinct semicircular crack with a depth of 0.2 mm , which is shown in figure 29. Dividing by the test time, a growth rate of $9\text{E}-10 \text{ m/s}$ results. Finally, a third test cycle under the same conditions was completed to enhance the data base. After this test, 26 of the 30 specimens (except of four which were new ones and had stress intensities below $28 \text{ MPam}^{1/2}$) were broken open to make sure that possible stress corrosion is detected. Of all these specimens, only one showed a semicircular crack with a depth of 0.3 mm , very similar to that found in test 17. Stress intensity and crack growth rates of these two specimens are also given in table 6.

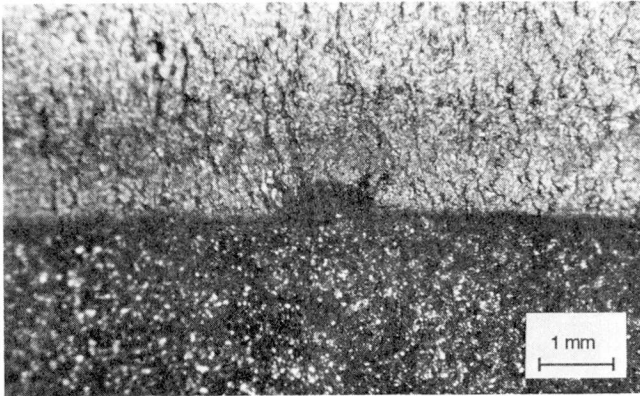


Fig. 29: Transgranular stress corrosion crack in an alloy D-specimen in test 17

From test 16 on, water chemistry analysis comprised most of the possible impurities which make up the enhanced conductivity. For chloride and sulphate, values lower than 30 ppb and 13 ppb respectively, were determined. Other impurities which were present in a concentration of a few ppb were silicon, calcium, potassium and chromium.

5.2.3. Effect of the electrochemical potential

So far, stress corrosion has never been detected on 'fresh' specimens in a test run. Both a new fatigue crack and a slight raise of the load line deflection was successful in triggering stress corrosion cracking, but only on specimens which were under test for at least one test cycle and where thus preoxidized.

Potential measurements revealed that the raise in electrochemical potential upon start up clearly depends on the history of the specimen. A fresh surface of a low alloy steel needs several days to establish the same potential as an already oxidized surface. Therefore, the driving force for SCC will be low at the beginning of a test and it is probable that crack growth may not start any more when the specimen potential remained below a threshold for several days.

The electrochemical potentials of specimens at four different locations within the autoclave were usually measured simultaneously and a scatterband of up 80 mV between the four readings was always given when potentials reached a steady state. Also, at lower

dissolved oxygen contents, the scatter tends to be larger. Several reasons account for this scattering:

- The inlet oxygen content is higher than the outlet (measured in the low pressure part) and a concentration gradient field will develop inside the autoclave which is closely packed with specimens. Thus, a higher flow rate is desirable for an equal concentration within the test autoclave.
- True flow velocity of water at the specimen side faces varies within the autoclave, depending on the location of the specimens. All specimen front- and back-surfaces are parallel to each other and to the main flow direction from inlet to outlet. Because of the low refreshment rate in the experiments, nearly stagnant areas are expected near the autoclave wall.
- The state of oxidation of the specimen surface from preceding tests influences the electrochemical potential.
- Differences in chemical and structural composition may influence the corrosion potential.

The last point seems to be of minor importance in high temperature water with a high dissolved oxygen content, where the potential difference between the stainless steel wall and a low alloy steel specimen was typically between 40 and 60 mV only, as measured in all tests conducted so far. At higher flow rates, low alloy and stainless steel show even smaller differences in their corrosion potential.

The behaviour of a fresh specimen surface is illustrated in figure 30. The different curves depict the potential readings of a platinum electrode, two old specimens and two fresh specimens vs. the autoclave body in test 12 (outlet dissolved oxygen was 0.4 ppm). It's obvious that the corrosion potential of a preoxidized specimen stabilizes after a few hours which may be essential for crack initiation. Fresh specimens were therefore loaded to a stress intensity below $30 \text{ MPam}^{1/2}$ to preoxidize the surface before enhancing the stress intensity for the following test. An other important factor was the time to reach the specified oxygen concentration, since heating up started with a very low oxygen concentration (around 1 ppb) to avoid corrosion at room temperature (specimens stayed overnight in cold water before heating up).

Figure 31 summarizes the measured corrosion potentials for the autoclave material 316L (upper band) and the low alloy pressure vessel steels as well as the range of crack growth rates at 1500, 800 and 400 ppb dissolved oxygen.

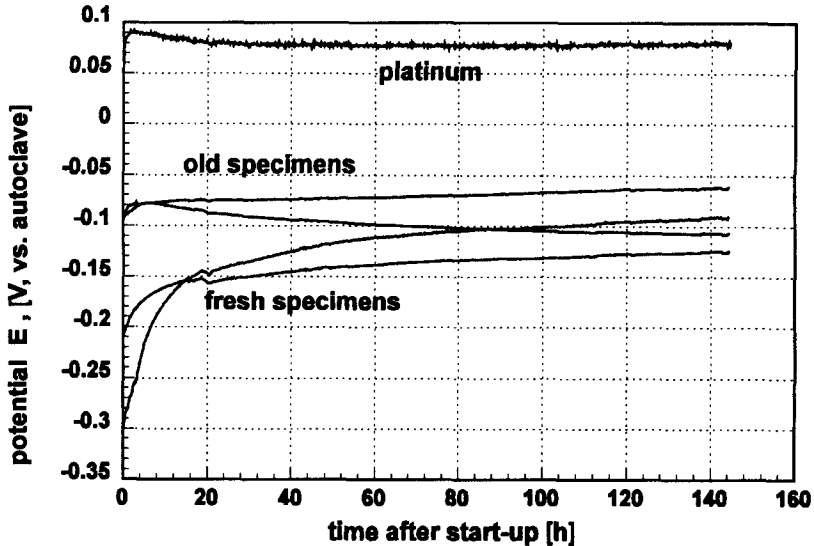


Fig. 30: Potential reading at the beginning of test number 12

The scatterband of the corrosion potential of the low alloy steel specimens suggests that stress corrosion should occur at 200 ppb oxygen also since potential values overlap for the most part with those at 400 ppb. Unfortunately, the corrosion potentials of the broken specimens were not directly measured. However, since the exact position of each specimen was always noted, it was seen that stress corrosion cracking most often occurred in specimens in the first autoclave in the loop and there, mostly in the lower half of the volume. Potential readings gave no hint for higher corrosion potentials in the lower half of the vessel since in one test, a specimen near the outlet hole right below the autoclave lid had the highest values, in an other test this was a specimen near the inlet. Recording of the corrosion potential of all the inserted specimens would certainly be necessary for a more detailed discussion.

The influence of the flow rate could not be determined but is also important because a higher flowrate is known to decrease the susceptibility to SCC but also enhances the corrosion potential, which has an adverse effect. The relative weight of the two effects is not known up to now.

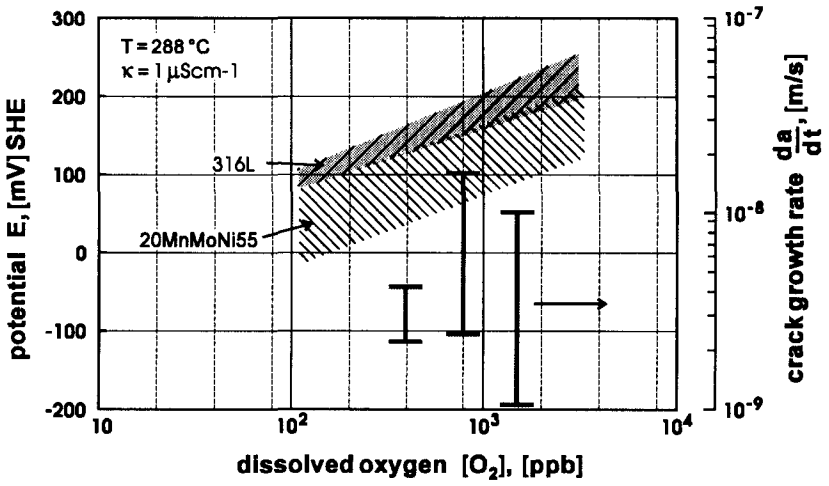


Fig. 31: Corrosion potentials and crack growth rates in 20MnMoNi55 wedge loaded DCB specimens in the refreshed water loop at 288°C and 1 μ S/cm.

5.3. Constant load tests

5.3.1. Test conditions

Constant load tests on DCB fracture mechanics specimens at temperatures from 180 to 320 °C were conducted primarily in order to evaluate the temperature and potential dependence of the stress corrosion crack growth rate in stagnant deionized water.

High purity water with a conductivity of less than 0.3 $\mu\text{S}/\text{cm}$ at the beginning of a test (measured before closure of the autoclave lid) was supplied from a nuclear grade ionic exchanger. The specifications of water leaving the ionic exchanger device followed by an additional activated carbon column and a 0.2 μm diaphragm filter demand a conductivity of 0.055 $\mu\text{S}/\text{cm}$ (RT) and a total oxygenable carbon content of less than 20 ppb. The conductivity was controlled by a on-line instrument to detect saturation of the ionic exchanger package.

Clearly, water chemistry could not be controlled within narrow limits during an experiment. At the end of a test lasting several hundred hours, higher conductivities in the range 2-5 $\mu\text{S}/\text{cm}$ for the titanium autoclave and 5-10 $\mu\text{S}/\text{cm}$ for the 316L autoclave (smaller volume) was measured immediately upon opening. A quantitative analysis of the water was made in a few cases for the following species: Cl^- , SO_4^{2-} , Fe, Cr, Si. The upper and lower limits of this analysis were, expressed in mg/l or ppm: Cl^- : 0.3 to 1.1; SO_4^{2-} : 0.2 to 0.6; Si: 0.6 to 2.5; Fe, Cr: ≤ 0.1 .

Leakage of the reference electrode through the porous plug is responsible for the chloride ions found in the water samples. Sulfate traces can be explained by the dissolution of MnS particles lying in the surface of the specimen. The pH value was measured after the tests and was always between 6 and 7, indicating that dissolved ions had no effect on the pH of the water.

Similar test procedures for all specimens were chosen during start-up of an experiment. Before heating up an autoclave, oxygen was thoroughly driven out by pure argon bubbling through the water. After reaching the specified test temperature, the specimens were kept under argon for two more days in order to stabilize both temperature and clip gage signal. A stress intensity of 20 to 30 $\text{MPam}^{1/2}$ was usually applied during this time. Corrosion potential for insulated RPV steel was then about -650 to -750 mV SHE and around -500 mV for the titanium autoclave. The 316L autoclave did not achieve such a low potential due to its sluggish behaviour as described before.

By changing the inlet gas from pure Argon to an appropriate mixture of oxygen and argon, the corrosion potential was then rapidly raised within about one day. The potential would then rise only slowly to a constant value within a few days. Oxygen

concentrations in the water beyond 1 ppm were generally chosen as a calculated equilibrium value, dependent on the total pressure and oxygen content of the gas mixture. After reaching a near-constant potential, an additional load was carefully put on in steps of 1 to 2.5 kN which corresponds to a ΔK of about 3 to 7 MPam^{1/2}. A possible onset of stress corrosion crack growth was then followed for one day after load raise on the loadline-deflection curve. At lower temperatures near 200 °C, longer times were eventually necessary to decide whether crack growth had started or not. It was observed that a stress corrosion crack in a fresh specimen always started immediately upon applying additional load. Typically, upon loading, a higher crack growth rate established which fall within a few hours to a nearly constant value. However, often several steps were necessary to initiate the stress corrosion process. It was also observed that some crack growth is often observed but ceases after a few hours with an approximately exponential decay in the growth rate as a function of the time, instead of developing a constant velocity.

A list of all tested specimens, their stress intensity range, test temperature, dissolved oxygen concentration and the resulting stress corrosion crack growth rates is given in table II. The given velocities must be understood as maximum values which were sustained for several mm of crack advance. Whenever the crack growth rate was not constant but changing within an interval of fast and stable crack growth, two values are given as an upper and lower limit for the growth rate.

5.3.2. Effect of stress intensity

According to the procedure described above, the lowest stress intensity to start stress corrosion cracking was about 40 MPam^{1/2}. Crack growth itself then produced higher stress intensities due to the constant load. At high nominal stress intensities above about 60 MPam^{1/2}, crack branching with two main cracks growing at the same rate was often observed in the after-test examination. Long stress corrosion cracks generally didn't remain in mid-plane of the specimen but changed their path towards one sideface where the increase of the stress intensity with crack length is much higher. This makes stress intensity as well as crack growth rate determination, which is based on compliance calibration, difficult. Thus, the highest true stress intensities are probably far above those given in table II.

Figure 32 shows data for stress corrosion crack growth rates plotted vs. stress intensity for the alloys A, B and C for temperatures between 210 and 287 °C. Similar results for temperatures between 200 and 320 °C are plotted in Figure 33 for alloy D. The

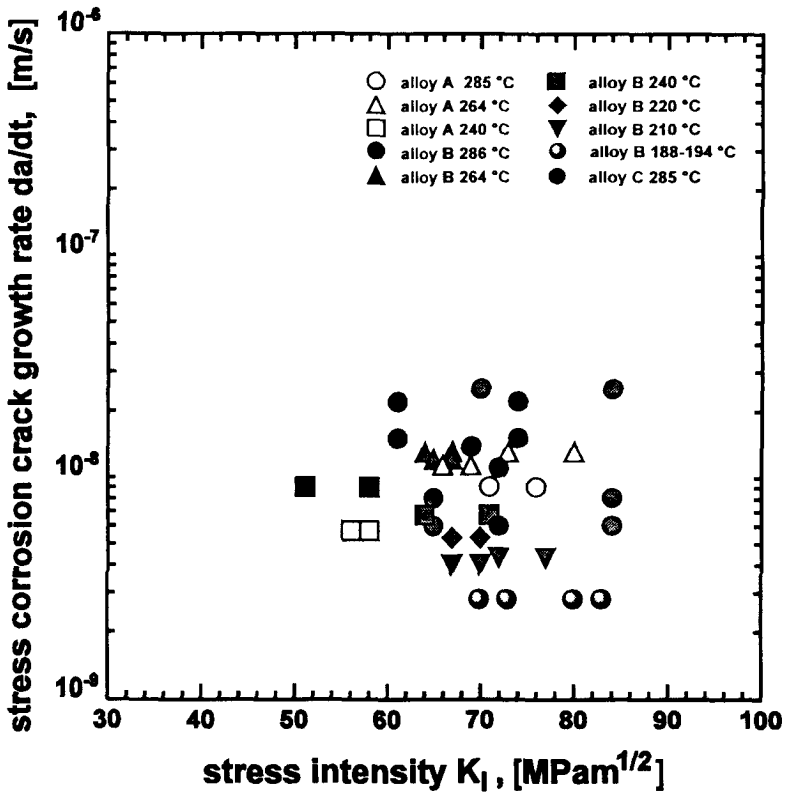


Fig. 32: Effect of stress intensity on stress corrosion crack growth rates at different temperatures for RPV alloys A, B and C

separation of the data is to provide better transparency. In the measured range between 40 and 100 $\text{MPam}^{1/2}$, crack growth rates are not influenced by the applied stress intensity. This behaviour has also been found in wedge loaded specimens tested in the refreshed water loop. The corresponding crack growth rates shown in figure 25 are lower than those measured at constant load but the results from the refreshed water loop tend to be too low because an incubation time and crack arrest cannot be taken into account. Thus, the growth rates are comparable in both environments. The threshold stress intensity K_{ISCC} could not be determined by the constant load method.

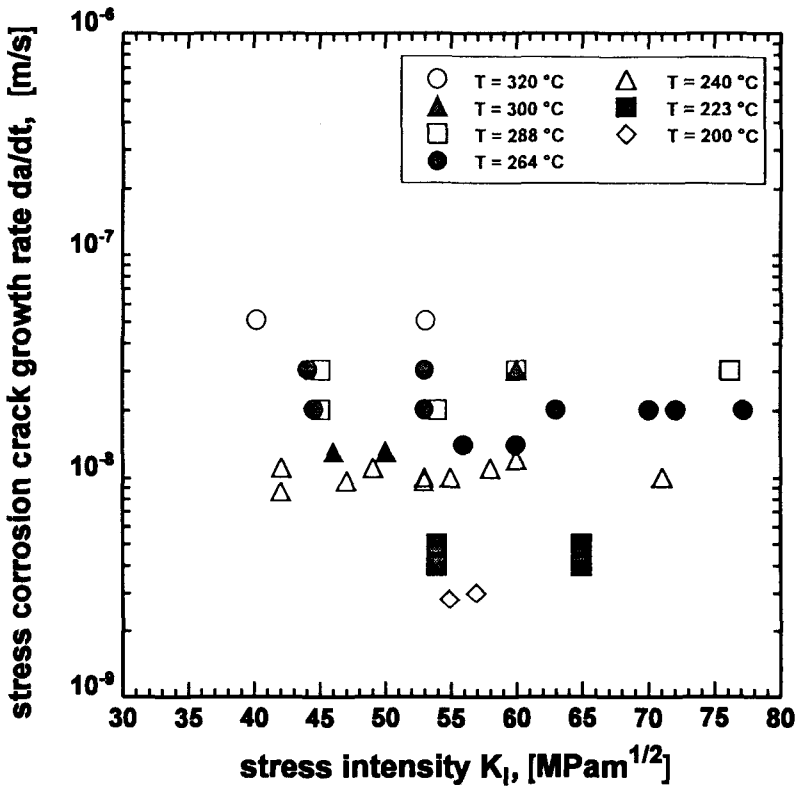


Fig. 33: Effect of stress intensity on stress corrosion crack growth rates at different temperatures for RPV alloy D

However, stress intensities necessary to initiate stress corrosion cracking in these tests were always beyond $30 \text{ MPam}^{1/2}$, which is the apparent threshold measured under constant displacement conditions.

Generally, a comparison of the data presented in this work with literature data is difficult because of different loading procedures and environmental variations of flow rate, oxygen content, conductivity and temperature as well as material properties like sulfur content and strength. Figure 34 shows the crack growth rates at 260 to 288 °C measured in this work and a scatterband of data from the literature which was obtained from fracture mechanics experiments on specimens with constant displacement [75,76], as

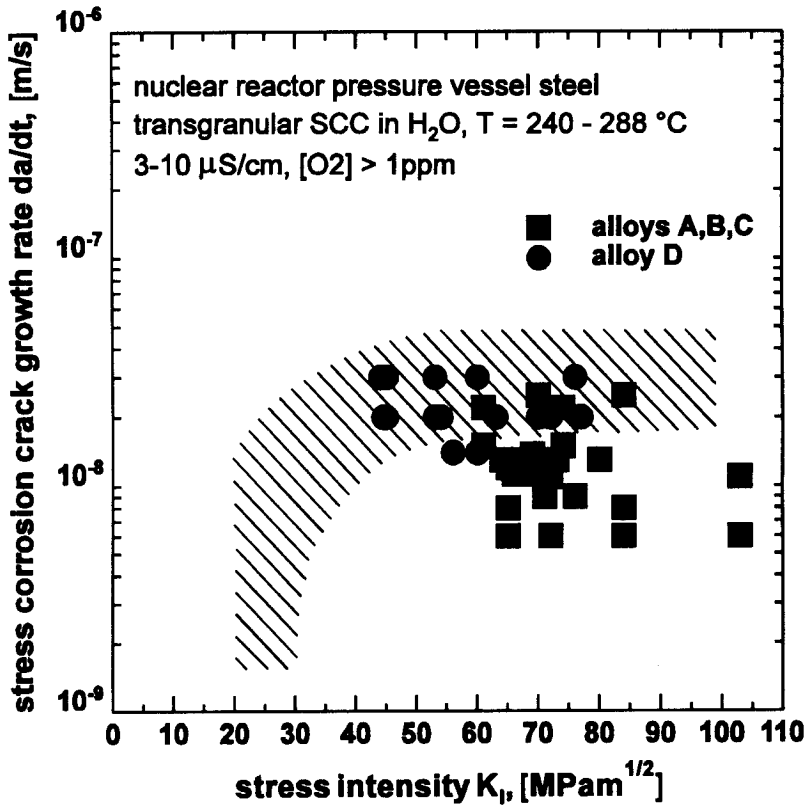


Fig. 34: Stress corrosion crack growth rates of pressure vessel steels, comparison with literature data.

well as constant load at 288 °C [80] and 240 °C [77,78,79] for oxygen concentrations of at least 8 ppm. It can be seen, that the highest crack growth rates measured in this work are well within the scatterband.

The crack growth rates between 1E-8 and 4E-8 at temperatures above 260 °C show considerable scatter. Growth rates of 3 to 4E-8 m/s are believed to be a kinetic velocity limit for the process responsible for crack advance. It's therefore expected that even oxygen concentration and conductivity far above those of the present work will not

produce still higher crack growth rates in the investigated steels. This has already be demonstrated experimentally [76].

5.3.3. Effect of the electrochemical potential

The HSST plate material alloy D was chosen to investigate the influence of corrosion potential on a growing crack at temperatures from 200 to 300 °C. Common practice in these tests was to first produce a high and stable crack growth rate by maintaining oxygen concentrations of typically 2 to 5 ppm. It was seen that crack growth rates at

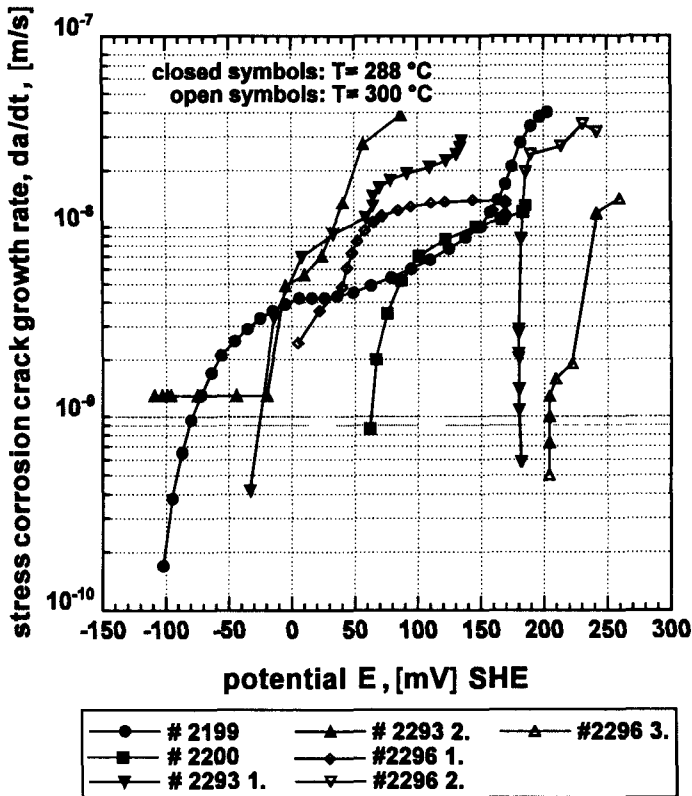


Fig. 35: Regression curves for the crack growth rate vs. the corrosion potential for alloy D at 300 and 288 °C in deionized water.

these oxygen concentrations lie in a plateau region where the effect of oxygen concentration and thus the corrosion potential becomes weak since growth rate is expected to be kinetically limited in this range by transport processes in the electrolyte at the crack tip.

Then, upon changing the gas mixture to a lower oxygen content, the corrosion potential of the specimen dropped slowly. Simultaneously, the crack opening displacement was recorded to get the crack growth velocity as described in detail in chapter 4. As a result, the crack growth rate in each test was plotted vs. the measured electrochemical potential. Test temperatures were chosen as 200, 223, 240, 264, 288 and 300 °C to get an idea and a sound data base for the temperature dependence of the critical potential. Regression curves for the crack growth rate vs. the corrosion potential are depicted in figure 35 to 38 for the mentioned temperatures. At 223 and 200 °C, only one specimen was tested

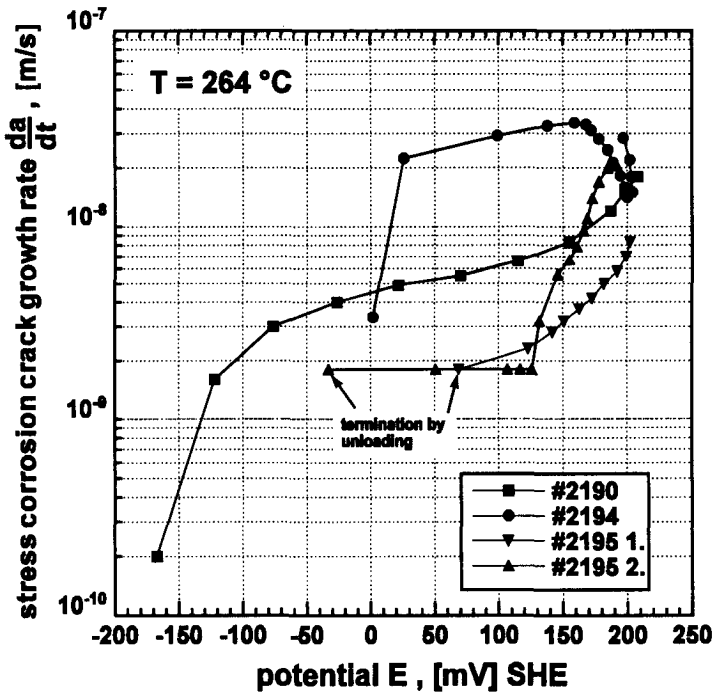


Fig. 36: Regression curves for the crack growth rate vs. the corrosion potential for alloy D at 264 °C in deionized water.

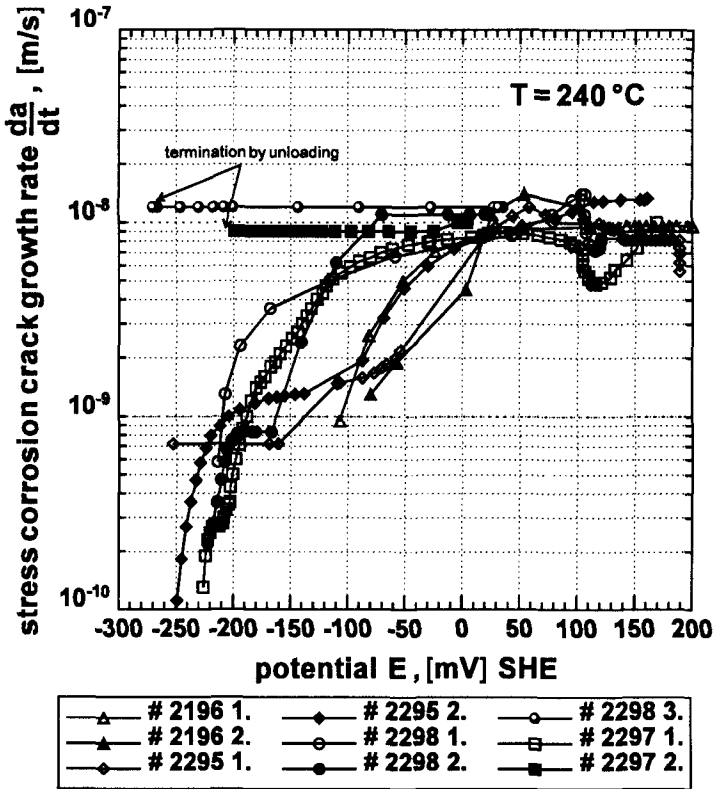


Fig. 37: Regression curves for the crack growth rate vs. the corrosion potential for alloy D at 240 °C in deionized water.

successfully in each case.

Often, the potential was lowered and raised consecutively several times during one experiment in order to study the effect of increasing and decreasing potential on the crack growth rate. The crack growth curve measured during a time interval with decreasing potential was observed to exhibit various shapes, some curves showing a uniform velocity decrease, whereas in other cases the velocity remained at a nearly constant value and dropped strongly below a certain corrosion potential, even when the same specimen was tested in several consecutive scans. The velocity of the potential

decrease was nearly constant in the high oxygen regime of the corrosion potential vs. oxygen concentration curve but dropped rapidly in the transition region.

Crack tip chemistry is expected to play a major role in stress corrosion cracking. A change in the corrosion potential at the crack mouth will induce a change in the crack tip electrolyte composition. The underlying diffusion and migration flows are time dependent and will thus follow with a certain delay. The measured crack growth rate curves do therefore not represent a steady state. To study the time dependent answer to a potential change, a potential step technique driven by a potentiostat should then be applied which would be a very desirable technique to get an idea of the time needed for a change in the crack growth rate at a constant potential.

As can be seen from the given plots, there is a strong effect of the potential on the crack growth rate, which takes the character of a threshold due to the asymptotic shape of the

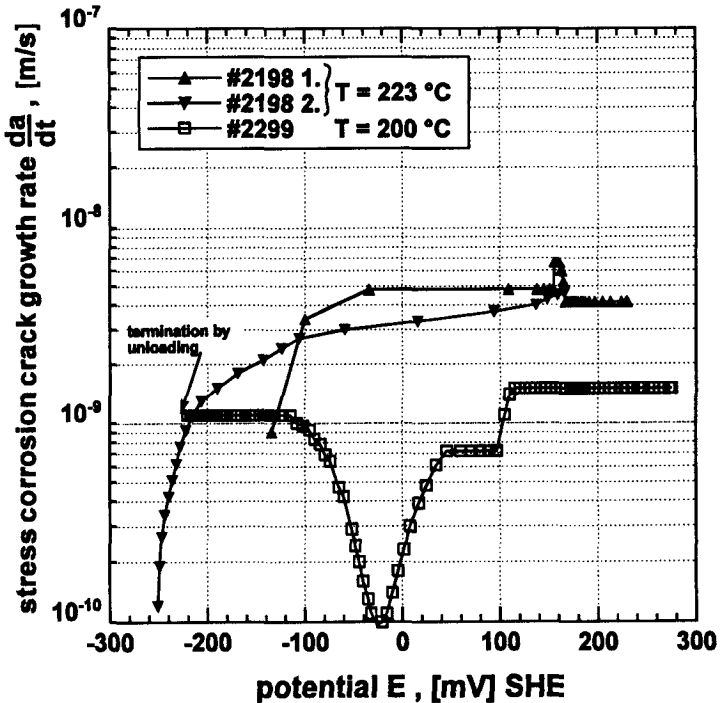


Fig. 38: Regression curves for the crack growth rate vs. the corrosion potential for alloy D at 223 and 200 °C in deionized water.

| specimen designation | temperature [°C] | crit. potential [mV] SHE | stress intensity [MPam ^{1/2}] |
|----------------------|------------------|--------------------------|---|
| 2299 LT9PA | 198 | <-230 | 65 |
| 2198 TL10CP | 223 | -140 | 61 |
| | 223 | -250 | 65 |
| 2196 TL9CP | 240 | -110 | 53 |
| | 240 | -80 | 55 |
| 2295 TL13CP | 240 | -255 | 48 |
| | 240 | -250 | 66 |
| 2298 TL23CP | 240 | -220 | 49 |
| | 240 | -230 | 53 |
| 2195 LT25PA | 264 | -5 | 61 |
| | 264 | -35 | 72 |
| 2190 LT36PA | 264 | -165 | 75 |
| 2194 TL6CP | 264 | 0 | 58 |
| 2293 TL14CP | 288 | -30 | 54 |
| | 288 | -110 | 61 |
| 2199 TL10PA | 287 | -105 | 72 |
| 2200 LT12PA | 288 | 50 | 52 |
| 2296 TL22CP | 300 | 5 | 51 |
| | 300 | 180 | 65 |
| | 300 | 200 | 67 |

Tab. 7: Critical corrosion potential for sustained SCC of reactor pressure vessel steel 20MnMoNi55 alloy D at different temperatures

curves. There is an appreciable difference down the temperature range from 300 to 200 °C. At 240 °C for instance, the growth rate lies in a plateau above about 0 mV vs. SHE and the lowest measured critical potential is around -250 mV.

At 288 °C on the other side, there was a steady decrease of the growth rate from the beginning of the scan. To narrow the scatterband in a region of 3 to 4E-8 m/s, potentials above 200 mV will possibly be necessary. This could also give an explanation for the relatively large scatter of crack growth rates between 260 and 300 °C measured in alloys A, B and C where the chosen oxygen content may have been too low in some cases.

As in wedge loaded specimens, long cracks tend to turn to the side under constant load so that the stress intensity becomes very high. These cracks did not slow down towards

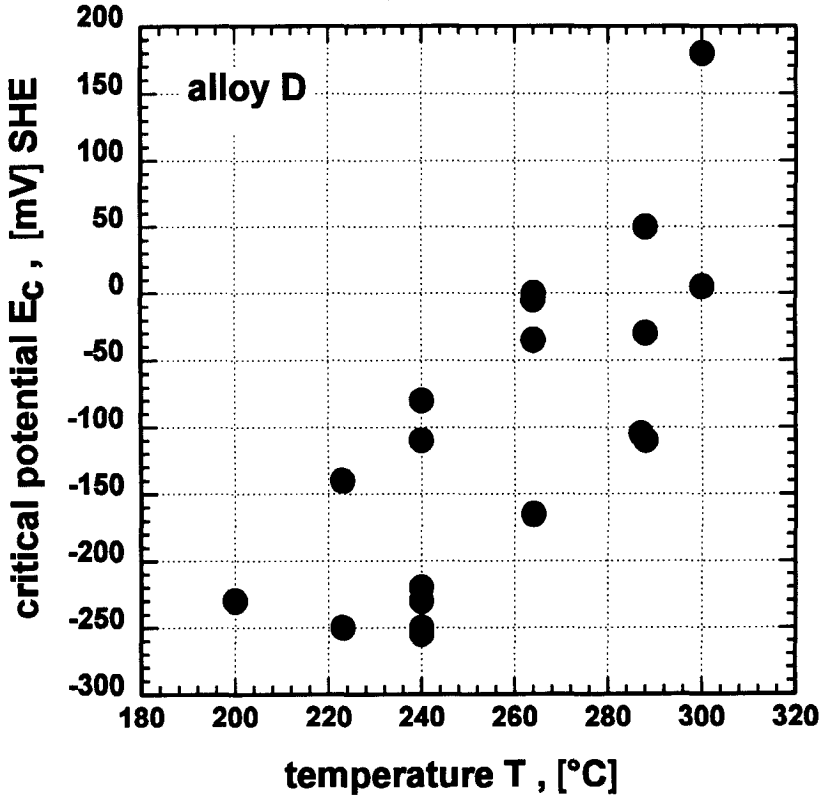


Fig. 39: Critical corrosion potential for SCC derived from falling potential experiments on double cantilever beam specimens at temperatures between 200 and 300 °C

lower potentials and the tests had to be stopped in that case. Interestingly, the growth rate remained constant, indicating that the crack growth was still corrosion based.

As soon as the fitted crack growth rate curves reached a value of below $1\text{E-}10$ m/s, the potential at that time was taken as the critical potential E_c for SCC crack growth. Specimen designation, test temperature and the nominal stress intensity range as well as the measured critical potential values are given in table 7 and plotted in figure 39 as a function of the test temperature.

It is interesting to note the behaviour of a stress corrosion crack when raising potentials from values where no crack growth could be detected any more. Usually, crack growth started only far above E_c but then very fast within one or two hours. There is thus some indication that a certain time is needed to establish the crack tip conditions needed for stress corrosion cracking to proceed. These conditions could be met when the potential driven accumulation of detrimental sulfur anions at the crack tip has reached a critical value. It must be emphasized that load remained completely constant during this process which means that no mechanical component like new crack tip strain is needed for re-initiation of SCC. On the other hand, fast crack growth sometimes wouldn't start at all after a high potential was reached again and a unload/load cycle of about 10% of the total load or application of additional load was necessary to continue the stress corrosion process.

A limiting factor in the evaluation procedure of E_c was the scatter in the measurement of the crack opening displacement signal. Therefore, in some cases it was difficult to properly fit the data in the transition range from high to very low crack growth rate. Moreover, critical potentials are often located in the intermediate region of the corrosion potential-oxygen s-shaped curve where the potential is highly sensitive to even small changes in oxygen concentration and flow rate. Nevertheless, there seems to exist a clear temperature dependence of E_c , with lowest values at 200 to 240 °C as can be seen from figure 37. At 240 °C, crack growth was measurable down to oxygen concentrations of approximately 10 to 20 ppb. At 200 to 290 °C, the critical oxygen concentration is between 10 and 100 ppb in stagnant water. Since the corrosion potential in this intermediate concentration range seems to be highly sensitive to hydrodynamic effects [81], these values cannot be transferred to refreshed water systems.

Susceptibility to SCC decreases at temperatures over 240 °C. At 300 °C, crack growth disappeared already at fairly high corrosion potentials and oxygen concentrations of 4 to 10 ppm. This high threshold explains former experimental difficulties to initiate and sustain stress corrosion crack growth in specimens made from alloys 20MnMoNi55 B and C and the piping steel BW30 at this temperature and an oxygen concentration of 7 to 10 ppm. With these alloys, sustained stable crack growth in the expected order of $1E-8$ m/s could not be maintained, only $1.8 E-9$ m/s was measured for BW30 in a three-day period when crack growth seemed to be stable during that time. there is thus evidence that stress corrosion cracking at 300°C is restricted to high potentials and only possible when strong oxidants like oxygen are present in high concentrations.

At 200 °C, two tests were conducted to evaluate the critical potential. The first specimen (2197) showed a pronounced decrease of the crack growth rate already at 200 mV NWE but the total measurement time was too low to assure that crack growth had stopped.

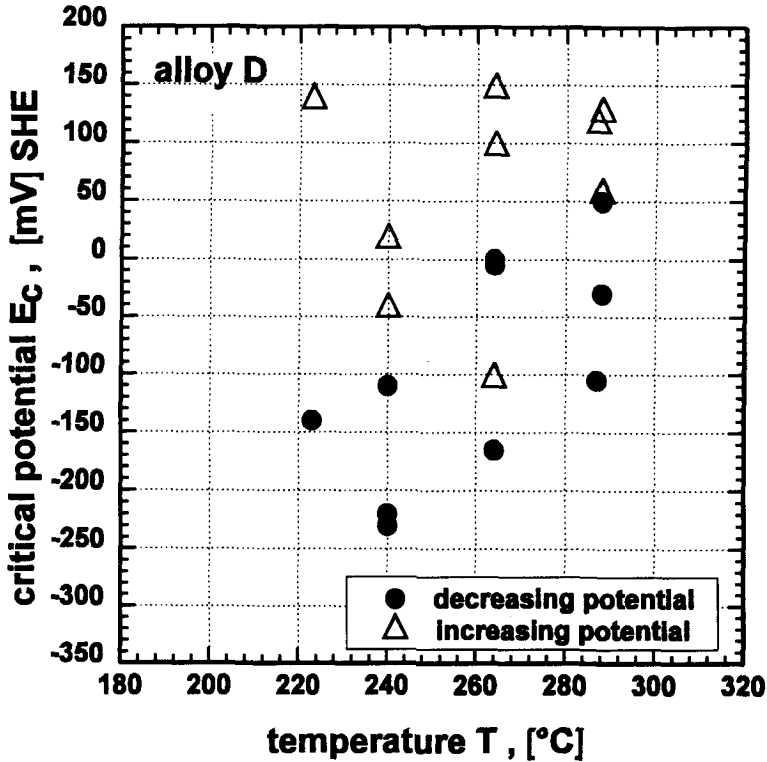


Fig. 40: Critical potentials for crack growth for decreasing and increasing potentials. Equal symbol shapes at a certain temperature belong to the same specimen

Also, the hysteresis effect was not seen when potential was raised again. The second specimen (2299) was then in the test for more than 1800 hours but a clear effect of the electrochemical potential could not be seen because crack growth rate scattered between $2E-9$ and $1E-10$ m/s and a period of a low crack growth rate near the resolution limit of the measurement capability could last for about 100 hours and then be followed by a much higher growth rate even during decreasing potential. Because of the electrical coupling between specimen and stainless steel autoclave, the potential decrease rate was very low even for oxygen concentrations below 5 ppb. The test was stopped at a potential of -225 mV NWE when crack growth was still detected. The critical potential may thus be lower than this value. Apart from the main crack, stress corrosion cracks

initiated from pits at both front faces ahead of the crack tip in the plastic zone and grew to a length of several millimetres.

The hysteresis effect is shown in figure 40 . The critical potentials are plotted as closed symbols and the respective potentials of re-start of measurable crack growth as open symbols for those cases where the load was kept constant.

5.3.4. Effect of temperature

Chemical reactions at the crack tip surface as well as equilibrium concentrations and diffusion/migration of ions from and to the crack tip region are all influenced by the temperature. It's not possible to isolate the different reaction systems contributing to the single numerical quantity of a crack growth rate. However, if stress corrosion in the investigated temperature range is determined as a whole by a thermal activated process, a relationship between crack growth rate and temperature can be expressed by an Arrhenius equation:

$$\frac{d \ln\left(\frac{da}{dt}\right)}{d\left(\frac{1}{T}\right)} = -\frac{E_a}{R} \quad (17)$$

Graphically, the logarithm of the crack growth rate is plotted vs. the reciprocal temperature to get a slope proportional to the activation energy E_a . The activation energy remains constant if only one thermal activated process is rate limiting in a certain temperature interval.

The effect of temperature on stress corrosion crack growth rate is shown for plateau conditions, where growth rates are nearly independent of changes in corrosion potential and stress intensity .The latter ranges from 40 to about 100 MPam^{1/2}. This means that only temperature variations are responsible for the observed differences in crack growth rate. Results are illustrated in Figure 41 where growth rates are plotted vs. reciprocal temperature in an arrhenius-plot. The data are the same as listed in table II. As can be seen, scatter in the data is growing towards higher temperatures, mainly at 300 °C. Alloy D tends to show higher crack growth rates than the other alloys above 240 °C. The slightly different behaviour of alloy D could possibly be related to the sulfur content which is the highest of all investigated alloys. An explanation for the large scatter at higher temperatures can be found in the influence of the corrosion potential on the crack

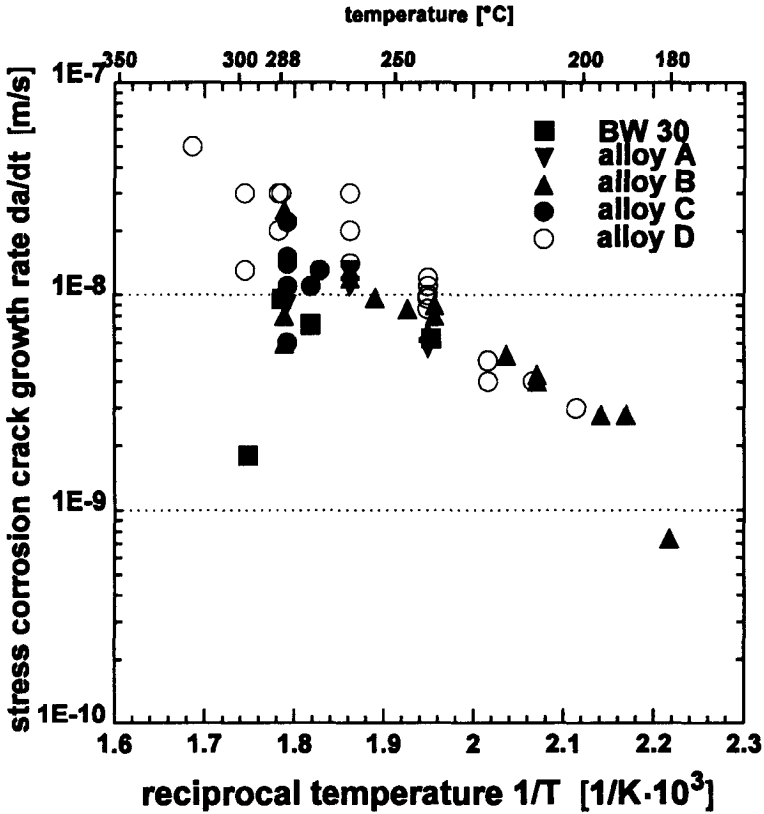


Fig. 41: Effect of temperature on crack growth rate of RPV steels.

growth rate. As has been shown, the critical potential becomes high at temperatures near 300 °C and possibly not all specimens reached a high enough potential that the assumption for potential independence is valid.

At the lowest temperature of 180 °C where an experiment was conducted, only one result is available. Relative errors caused by scatter in the clip gage signal become large at these low crack growth rates, e.g. a change of crack opening displacement of only 7.5 μm in 142 hours resulted in the given velocity of 7.4 E-10 m/s when scatter is usually within $\pm 2 \mu\text{m}$ for that time interval. Crack growth measurement based on the potential drop technique was planned as a parallel unit to the clip gages but installation was not accomplished before completion of the present work.

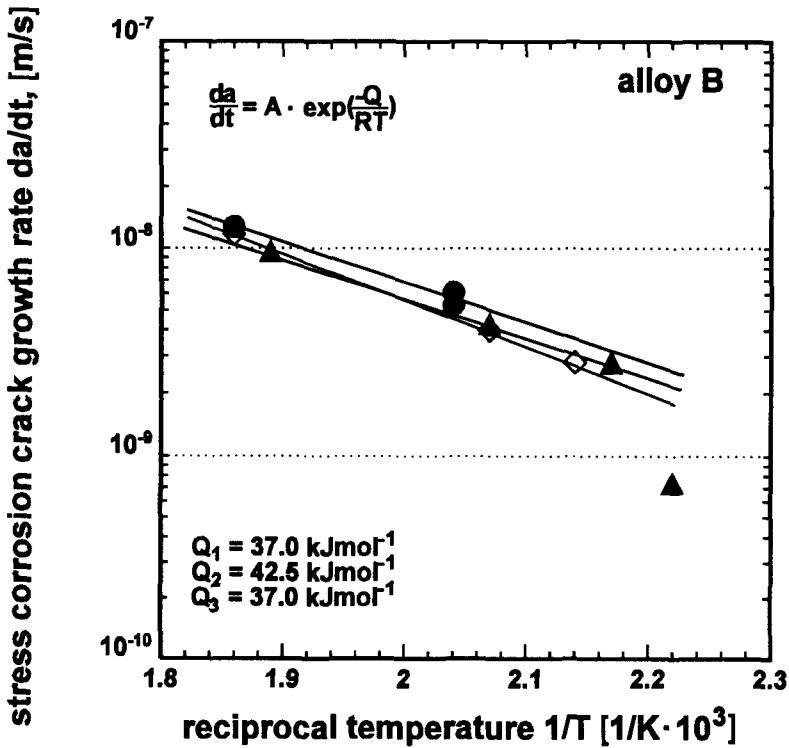


Fig. 42: Arrhenius-plot for crack growth rates of three specimens from alloy B with apparent activation energies

Between about 180 and 270 °C a linear relationship seems plausible for alloys A, B and C. Alloy D was additionally tested at 320 °C at a very high oxygen concentration of 200 ppm which gave a constant growth rate of $5E-8$ m/s. Separate linear regressions for the group of alloy A,B,C and for alloy D yielded the following activation energies: 40.5 kJmol^{-1} with standard a deviation of 2.5 kJmol^{-1} and 51.6 kJmol^{-1} with a standard deviation 2.7 kJmol^{-1} , respectively.

To get an estimation of the activation energy of the stress corrosion crack growth rate of a single specimen, temperature was varied during one experiment and stable crack growth rates were measured at each of the different temperatures. Corrosion potential was not measured but oxygen concentration was kept constant at 2 ppm for one

specimen and 7 ppm for the others. Figure 42 shows results of three experiments with the 20MnMoNi55 alloy B together with regression lines to derive an activation energy according to equation 17. Values between 37 and 42.5 kJmol⁻¹ were obtained.

5.3.5. Effect of specimen thickness

Crack growth measurements on fracture mechanics specimens are intended to give a basis for the evaluation of cracks in real components under service conditions. A single parameter, the stress intensity K_I , serves as characterization of the mechanical load necessary for occurrence of stress corrosion cracking. It's therefore to discuss the validity limits for specimen size so that SCC results measured at a given stress intensity are transferable to generally larger geometries. For the determination of fracture toughness in an inert medium, there is a validity requirement that specimen thickness and crack length should exceed $2.5(K_{IC}/\sigma_s)^2$ when K_{IC} is the fracture toughness and σ_s is the 0.2% offset yield strength of the material [33]. Of course it's not the intention of a stress corrosion test to determine a valid plane strain fracture toughness because applied nominal stress intensities are generally much lower. Nevertheless, for the given specimen size and for high toughness medium strength steels like those investigated in this work, the above criterion is not met at the stress intensities where crack growth was studied. The question arises whether SCC studies on small fracture mechanics test specimen give useful results to permit quantitative predictions for cracking susceptibility and crack growth rates in larger structures, even if above condition for fracture toughness tests in air is not met.

Specimens not meeting the thickness criterion may show extensive plastification and stable mechanical crack growth above certain values of the nominal stress intensity. Creep tests on a low sulfur pressure vessel steel performed in air showed that up to a stress intensity of at least 100 MPam^{1/2}, prolonged creep or stable crack growth can be ruled out for the chosen specimen geometry [83].

The stress intensity factor pertains to conditions of linear elastic behaviour and only indirectly to the plastic zone known to exist around the crack tip. This means that stress intensity is primarily used to quantify the elastic field which is responsible for the stress/strain conditions at the crack tip. It's therefore necessary that certain geometric limits must be considered in order to get a comparable plastic zone size for different geometries of specimens and cracks.

On the other hand it's known and has been confirmed in this work that stress corrosion crack growth rate is not influenced by the stress intensity in a broad plateau region and cracks have the tendency toward formation of branched systems as observed in many specimens. There is further evidence that electrochemical conditions are at least partly responsible for crack growth in high temperature water above 200 °C and thus mainly the crack tip electrolyte will determine the rate of crack penetration. It seems then justified to assume that SCC is rather insensitive to the size of the plastic zone ahead of the crack tip. The role of stress intensity is then reduced to a weakening of the crack tip surface for chemical attack. Moreover, the composition of crack tip solution will be

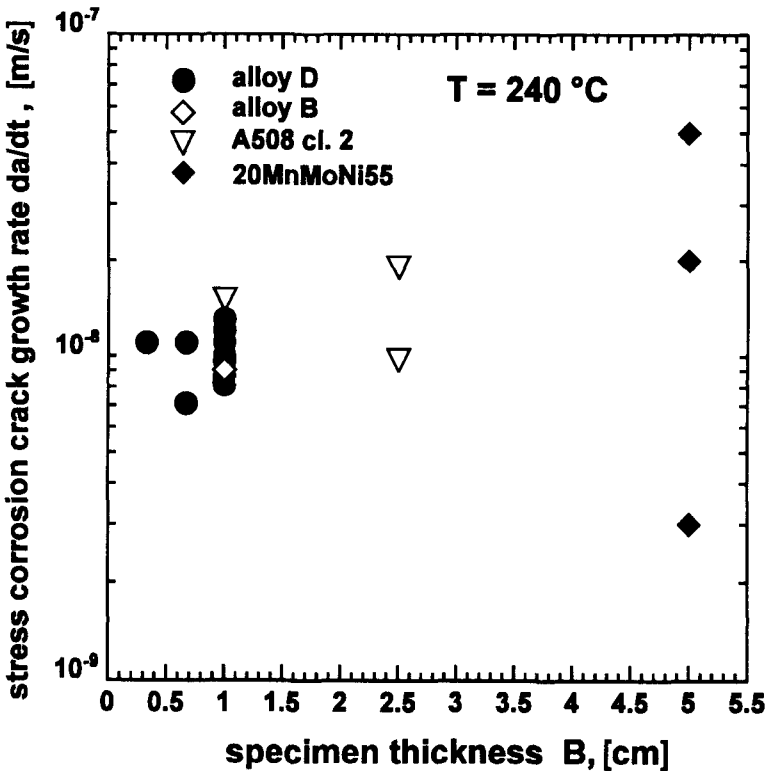


Fig. 43: Influence of the specimen thickness on the maximum crack growth rates in DCB and CT specimens of low alloy pressure vessel steels in deionized water at 240 °C.

influenced by available migration and diffusion paths and therefore by crack opening angle and crack length as well as specimen thickness. A given stress intensity is not able to describe this geometry influence so that new concepts may have to be developed to deal with all aspects of a specific SCC model.

To determine a possible effect of specimen thickness on stress corrosion crack growth rate, two specimens of 1/3 and 2/3 cm thickness of alloy D were tested at 240 °C. Additionally, two experiments with a 1 CT specimens of a A508 cl.2 steel were conducted to enlarge the investigated thickness range to 2.5 cm. The size of the constant load autoclaves did not allow for still bigger specimen sizes. Figure 43 shows maximum stable crack growth rates plotted vs. the specimen thickness. Data for 50 mm thick CT specimens were taken from the literature [79], obtained at 8 ppm oxygen and a stress intensity between 80 and 90 MPam^{1/2}.

One result of the low sulfur alloy B is also shown for comparison with the A508 alloy with about equal sulfur content. As can be seen, there is a slight effect of specimen thickness on crack growth rates measured in the plateau region of potential and stress intensity. Thicker specimens can obviously express somewhat higher maximum crack growth rates which could be explained by the plane strain condition which prevents the crack line trailing as observed in thinner specimens. A principle difference in the crack growth mechanisms can not be inferred from these results.

Another interesting question was the behaviour of the critical cracking potential when the specimen thickness was changed. During the experiments for the above data, critical potentials were also determined on the same specimens.

These values are shown in figure 44 where different points at 1/3, 2/3 and 2.5 cm belong to several falling potential curves. The data indicates an influence of specimen size on the critical potential. The 1 CT specimens of alloy 508 cl. 2 were tested intensively in several falling/rising potential scans to get a better verification for the comparatively high values of E_c . A comparison of different specimen thicknesses is complicated by the different alloy selections, since from alloy D, only 10 mm DCB specimens were available. Alloy A508 cl. 2 seems to have a higher resistance to stress corrosion cracking than alloy D and B, the latter with about equal sulfur content.

There appears to be a trend for lower critical potentials, E_c , with smaller specimen thickness. However, much more experiments will be necessary to conclusively answer the most interesting question of a thickness dependence of the critical potential.

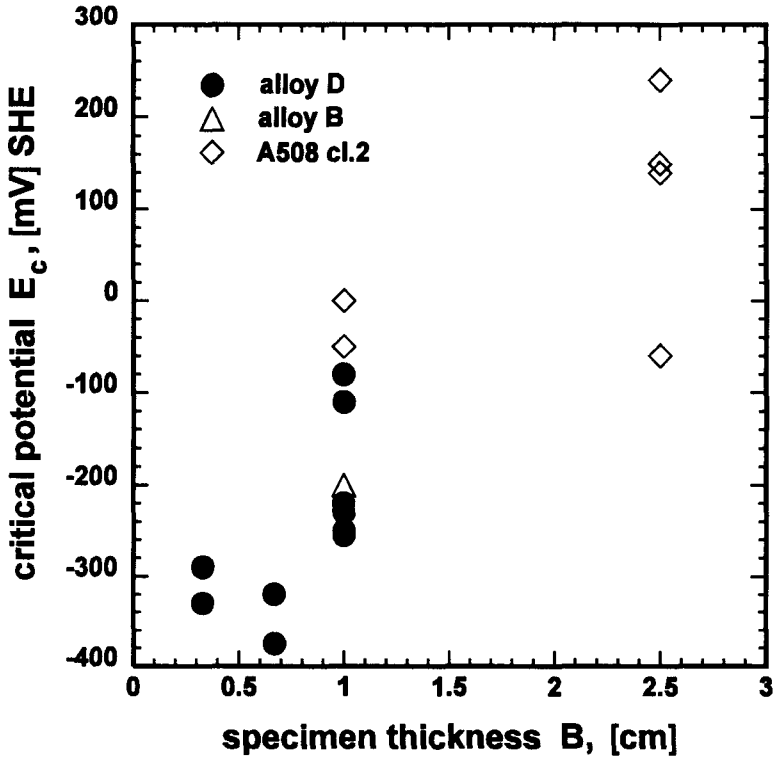


Fig. 44: Critical corrosion potential for stress corrosion cracking as a function of the specimen thickness

5.3.6. Effect of higher water conductivities

Unintended pollution of the deionized water occurred when potential measurements with the external reference electrode were introduced and extensive leakage of its inner 0.1M KCl electrolyte lead to a conductivity of about $20 \mu\text{S}/\text{cm}$ (measured after the test). This value corresponds to several ppm chloride. Only two constant load tests were conducted at these high chloride concentrations and for the following tests, a modified electrode

| test nr. | alloy design. | T [°C] | K _I [MPam ^{1/2}] | [O ₂] [ppm] | Impurity | κ (25°C) [μS/cm] | da/dt [m/s] |
|----------|---------------|--------|---------------------------------------|-------------------------|---------------------------------|------------------|--------------|
| 1 | C | 277 | 63 | <0.005 | FeS | 68 | - |
| 2 | C | 279 | 61 - 68 | 9 | FeS | 115 | 1.1E-8 |
| 3 | C | 277 | 69 - 83 | 10 | FeS | 68 | 2.1 - 2.6E-8 |
| 4 | B | 286 | 70 | 6 - 190 | Na ₂ SO ₄ | 1000 | not stable |
| 5 | B | 288 | 76 - 84 | 9.3 | Na ₂ SO ₄ | 1200 | 9.5E-9 |
| 6 | B | 286 | 70 - 90 | 10 | Na ₂ SO ₄ | 50 | 3.2E-8 |
| 7 | C | 288 | 75 - 80 | 9 | MnS | 45 | 3 - 4E-8 |
| 8 | C | 299 | 85 | 8 | MnS | 45 | not stable |
| 9 | D | 288 | 60 | 8 | FeSO ₄ | ~50 | 4E-8 |

Tab. 8: Constant load experiments at higher water conductivities

was used to minimize the leakage to below 1 ppm chloride after the test. The two mentioned experiments involved alloy B specimens at a temperature of 287 °C, 2.4 and 5 ppm dissolved oxygen, respectively. These oxygen contents proved to be sufficient for sustained stress corrosion cracking in high temperature water of 'normal' conductivity (about 3 to 5 μS/cm at 25 °C)

In both tests at the higher chloride concentrations, stable stress corrosion crack growth could not be achieved, though the stress intensities were enhanced stepwise to values of 68 and 76 MPam^{1/2}. The fracture surfaces in both specimens revealed only one single site of SCC growth with a semielliptic crack of about 2 mm diameter. The remaining precrack front showed only a small 0.1 mm wide fringe of initiation sites. Since this picture was seen in both tests and was never again seen in the following ones, it was concluded that the higher chloride concentrations produced some kind of inhibition. This inhibiting effect could be related to adsorption effects at the crack tip or excessive blunting due to localized corrosion. Further experiments with chloride contaminated water (above 1 ppm) were not conducted.

Another important water pollutant is sulfur which is commonly seen as a major contributor to SCC susceptibility, be it as solid MnS in the steel which dissolves in contact with water or as an already dissolved sulphate or sulphide contamination.

Several experiments with sulfur contaminated water with fairly high concentrations were done in the constant load autoclaves. Different sulfur species were tried to investigate their influence on the stress corrosion susceptibility. In one part of these experiments, either solid FeS or MnS were both introduced in large quantities so that the measured

conductivities represent their solubilities. In test 7, MnS was filled into a 1 mm hole down the precrack to dissolve directly into the crack.

In tests 4, 5 and 6, Na_2SO_4 was used in different concentrations. Test 9 was conducted with a FeSO_4 solution with a concentration of 20 ppm SO_4^- .

As can be seen from table 8, crack growth was not detected in oxygen-free, FeS-saturated water at 277 °C. High oxygen concentrations were then chosen for the following experiments, which was seen to be a necessary condition to initiate high crack growth rates. The highest growth rates were measured at intermediate conductivities of about 50 $\mu\text{S}/\text{cm}$. These velocities lie at the upper bound of the scatterband of those tests which were conducted in deionized water. It's thus believed that 3 to 4 E-8 marks a kinetic velocity limit at a temperature of 288 °C in the investigated steels.

Crack growth in the sulfate solution in test 4 was not stable, in spite of the very high oxygen concentration of about 190 ppm (air) which was introduced after stable crack growth could no be established at about 10 ppm. The crack grew only temporarily during a couple of hours after a load step. This behaviour contradicts the trend for an increasing susceptibility the higher the concentration of sulfur species in the water. Na_2SO_4 may however shift the solution pH at the test temperature to higher values, which will effectively buffer the crack tip electrolyte.

It seems important to note that even in FeS and MnS contaminated water, stress corrosion crack initiation happened only when the oxygen content was raised to high values. It's however possible that the high crack growth rates are then sustained to lower critical potentials than those in pure water. Experiments to verify this assumption were not accomplished.

6. Discussion

A typical feature of stress corrosion cracking in high temperature water is the existence of several threshold conditions which are marked by a large change in the degree of environmental degradation with minor changes of the measurable system parameters. The important variables are listed as follows and for all of them, a threshold behaviour has been reported in the literature:

- Tensile stress in constant load mode on plane specimens
- Strain rate in plane and precracked specimens
- Total strain in plane specimens
- Stress intensity and cyclic stress intensity in precracked specimens
- Dissolved oxygen concentration in the water
- Corrosion potential
- Impurity level in the water and in the material, e.g. sulphide
- Temperature
- Water flow rate

The influence of the different variables is widely discussed and often, controversial views and data is published. The most interesting and complicating task is to find interrelations between the influential system variables and thus between their threshold values. The discussion of literature and own results will therefore centre on the main system parameters which are listed above and their implication on the susceptibility to stress corrosion cracking, without entering too much into the discussion around the exact mechanism which may be operative.

6.1. Mechanical effects

Stress and the accompanied strain is considered to play a fundamental role in stress corrosion of ductile alloys both for initiation and propagation of cracks. The different specimen types (plane or precracked) and load application methods provide an uncertainty about the comparability of results from different laboratories. Some literature data will be examined which are relevant to discuss own results.

6.1.1. Load and strain effects

Current knowledge shows that attention must be given to creep and relaxation effects upon loading of a specimen. In constant load tests on precracked pipeline steel specimens in carbonate-bicarbonate solutions, it was shown that crack initiation takes place immediately after loading and can be suppressed if loading and creep relaxation is done in an inert environment [84]. This indicates that one important condition for crack initiation is a strain rate exceeding a critical value which is influenced by environmental parameters like pH and ionic activities. These considerations apply equally to growing cracks.

During the numerous experiments which were conducted in the constant load autoclaves, it was often seen that crack growth occurred only during a limited time upon a load increase step.

Figure 45 gives an example of a constant load experiment conducted at 268 °C and 1.8 ppm O₂ with a specimen of alloy B. High crack growth rates around 10⁻⁸ m/s were observed upon loading steps from 59 to 61.8, 62.4 to 66.7, 68.9 to 71.8 and 72.4 to 76.8 MPam^{1/2}, but the initially measured high crack growth rate could not be sustained. In some cases, more than one millimeter crack advance was observed during such instable crack growth. A plausible explanation for such a behaviour lies in the electrochemical conditions and the solution composition at the crack tip which change in line with the

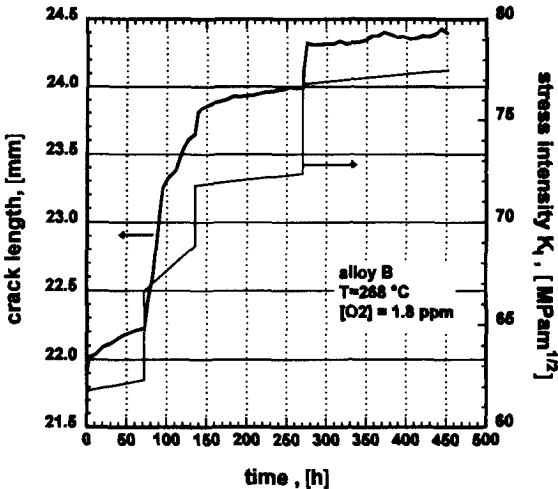


Fig. 45: Non steady state crack growth of alloy B at 268 °C and 1.8 ppm O₂

crack growth rate. Obviously the initial state after the load step could not be sustained, despite the high crack growth rate in the plateau region, which would give a constantly high crack tip strain rate. In a certain area of the chosen environmental parameters, stress corrosion is thus extremely sensitive to load variations. In some experiments, crack growth was triggered with a load increase of only 2%. This fact illustrates that load control in engine driven pull rods (e.g. hydraulic systems) should be done as exactly as possible, if the load is to be kept constant. In this sense, an easy system containing a load beam is best suited for constant load experiments. The instable crack growth after each time additional load is applied is a clear indication that only a still higher crack tip strain causes a 'revival' of the SCC process. Since the initial crack growth rate lies in the plateau region which gives the maximum rate which is possible at all due to kinetic limitations, it may be assumed that a change in the crack tip chemistry happens during crack growth. For this change, it's most probable that an impurity of the steel itself is responsible for SCC which will be discussed later.

As a rough conception of the action of crack tip strain, it can be assumed that fresh metal surface is exposed to the water due to the disruption of the protective oxide layer. This enhances the dissolution current density by several orders of magnitude. The resulting high concentration of metal ions leads to a local solution acidification due to hydrolysis and migration of anions like sulfate or chloride into the crack tip region. This is an autocatalytic process since the main source of dynamic strain is the crack growth itself. For constant load, the crack tip strain rate was given as follows [85]:

$$\dot{\epsilon}_{ct} = A(\sigma_y) \cdot K^m \cdot t^{-1} + \frac{Bv}{x^*} \quad (18)$$

The first part of the equation represents the time dependent creep strain as an answer to a load increase and the second term quantifies the growth rate dependency, when x^* is, according to Ford [86], a displacement quantity of the crack tip stress field. It was seen in this work that the crack tip strain rate seems to be very important considering the initiation of crack growth. However, on growing cracks, a K_I - and therefore strain rate dependence could not be observed. This dependence could well be masked by a kinetic limitation for the measured crack growth rates which mostly lie in the scatterband for the maximum growth rates and are thus also independent of K_I (above about $30\text{MPam}^{1/2}$). During the experiments with a slow change of the dissolved oxygen content, a decreasing or increasing crack growth rate could be measured, but the scatter in the measured critical potential did not allow to find a systematic influence of the stress intensity. For very high stress intensities (above $100\text{MPam}^{1/2}$), sustained cracking is possible even at

potentials lower than the critical ones. This behaviour was observed in two experiments at 240 °C (alloy B and D), where the cracks bent off sideways so as the stress intensity could not be calculated but was certainly above 100 MPam^{1/2}. The crack growth rate remained constantly high in these specimens, even below the critical potential and the test had to be stopped by unloading. It can be argued that purely mechanical crack growth had taken place, but this is unlikely since the growth rate was constant which shows that the mechanisms responsible for SCC must still have been operative.

Cyclic loading offers a further possibility to investigate the influence of crack tip straining on the corrosion process leading to environmental assisted cracking (EAC). Due to a periodic restraining of the crack tip material, the crack growth rate will probably be more stable than under constant load, allowing to reproduce the measured crack growth rates also at critical values of the environmental parameters.

It has been shown that high R-ratios can lower the threshold stress intensity, which means that K_{max} is lower than K_{ISCC} , the latter being determined under constant load conditions [84]. Due to the cyclic loading, a stress-strain hysteresis curve will develop at the crack tip, giving a strain rate which is approximately proportional to the loading frequency [87].

Van der Sluys et al. have shown that medium to high sulfur pressure vessel steels undergo environmental assisted cracking in BWR and PWR water at 288 °C only in a limited frequency range [100-102]. Below a critical frequency, the high growth rate caused by stress corrosion cracking cannot be sustained and falls back near the air base line. In the susceptible range, the time based crack growth is not independent on the frequency, otherwise stress corrosion crack growth is expected for the limiting case of constant load. According to the given data, the crack advance per cycle due to stress corrosion decreases with decreasing frequency or increasing cycle rise time. This means that the stress corrosion part of the crack growth rate is time dependent. It's thus very important to distinguish between constant load and load cycling at low frequencies of about 1 cycle per minute or lower.

For pressure vessel steels in BWR water, the critical frequency at which growth rates express a transient behaviour is lowered by higher stress intensity amplitudes but saturates at some value [101]. The described behaviour indicates that stress corrosion cracking at constant load may not be observed over an extended period of time in clean BWR as well as in PWR water at 288 C. However, low cycling may lead to a severe susceptibility resulting in the same brittle fracture appearance. It's therefore necessary to examine both together constant and cyclic loading with regard to a mechanistic understanding of environmentally assisted cracking.

A confirmation of this view is given by comparing environmentally enhanced crack growth rates at 288 °C under cyclic loading in BWR water with the fastest crack growth rates measured in this work under constant load and a more severe chemistry. These growth rates range from 1E-8 to about 4E-8 m/s for both cases which seems to be the kinetic limit of stress corrosion of low alloy pressure vessel steels in high temperature water at this temperature. The observation of a critical time based crack growth rate in corrosion fatigue experiments which lead to sustained environmental cracking could well be transferred to the constant load case. It can be assumed that, depending on the water chemistry and the electrochemical conditions, a critical crack growth rate exists which must be sustained for stable stress corrosion crack growth. An upper threshold growth rate is given by kinetic limits in the corrosion related transport processes and a lower limit by the growth rate to produce the necessary amount of sulfur concentration and corrosion current to keep the aggressive solution composition at the crack tip and to avoid crack closure by oxides. This lower limit for the crack velocity will still be a function of the water chemistry and possibly also of the applied stress intensity. It should also be considered that small stress corrosion cracks in constant load or constant displacement precracked specimens can be caused by unstable growth upon loading in the test environment, giving an overall growth rate which simulates a steady process. Fatigue results further show that such short cracks can be expected even at potentials prevailing in PWR water, e.g. after the initial loading step.

6.1.2. Threshold stress intensity

A threshold stress intensity K_{ISCC} is found in all stress corrosion tests with precracked specimens and is per definition a precondition to separate SCC from other localized corrosion forms. Since K_I can in principle be calculated for a given crack geometry if the acting loads (plus residual stresses) are known, K_{ISCC} allows to establish a safety margin against stress corrosion cracking. If a crack can not be detected by nondestructive testing, the largest flaw depth which can not be excluded (resolution limit) should be taken for calculation.

Literature data on crack growth rates as a function of stress intensity of low alloy steels in high temperature water indicate a K_{ISCC} value below 30 MPam^{1/2} for A533 pressure vessel steel at 288 °C [75]. For the low alloy piping steel 17MnMoV64, K_{ISCC} was estimated between 20 and 27 MPam^{1/2} at 240 °C [77]. In this work, the lowest stress intensities at which SCC was detected in the high temperature water loop at 288 °C were 32 and 33.5 MPam^{1/2} initially, with several mm of crack growth in each case. It would

have been very desirable to state stress intensities at the tip of the detected stress corrosion crack, but most of the crack growth was out of the midplane by up to 45°. This behaviour is believed to be favoured by the specimen geometry. Under constant load line deflection, the stress intensity first increases towards the side, contrary to slowly decreasing down the midplane. Then, approaching the side face, K_I will decrease until cracking ceases at K_{ISCC} . The analytical or empirical solution of an inclined crack in the used specimen geometry was out of the scope of this work.

According to the plane strain specimen thickness criteria of ASTM E399 [33], stress intensities up to about $30 \text{ MPam}^{1/2}$ are still plain strain values, given a specimen thickness of 10 mm, a fracture toughness of $200 \text{ MPam}^{1/2}$ and a yield strength of 500 MPa. Therefore, the cited stress intensities are valid under plane strain conditions.

Though the value of K_{ISCC} is approximately known, the theoretical explanation is still controversial. Different models for transgranular SCC in high temperature water are currently discussed and apart from the crack growth kinetics, they should certainly be able to explain the measured K_{ISCC} values.

The underlying physical process leading to a threshold stress intensity in the investigated system can be one of the following:

- stress ahead of the crack tip is too low for cracking induced by hydrogen or more general, for a matrix separation due to internal forces.
- there is a critical shear stress for slip step emergence and dissolution in an active path mechanism of stress corrosion cracking.
- the fracture strain to break the crack tip passive film is not reached or the crack tip blunts because the strain rate is too low (film-rupture-model)

Results from other studies [75] demonstrate that K_{ISCC} of low alloy steels in high temperature water is independent of the yield strength of the steel, in contrast to hydrogen induced stress corrosion cracking of high strength steels around ambient temperature. This shows that a change in the crack growth mechanism is likely to take place at a certain temperature and chemical factors like the crack tip solution composition become more important the higher the temperature.

6.1.3. Fractographic features

Fractographic examination of crack surface and cross sections can give an important contribution to the current understanding of stress corrosion cracking. As the primary method, fractography allows to determine the crack path, for instance to differ between trans- and intergranular stress corrosion.

All of the cracked pressure vessel steel specimens showed a transgranular crack path. The macroscopic morphology of the crack surface often features fan shaped subcracks, focusing at an inclusion site or at a corrosion pit from the surface. Due to macro- and microbranching over the crack front, considerable plastic deformation on intermediate ligaments takes place. Whether the necessary energy for the coalescence of microcracks can be delivered is dependent on the stress intensity. It's thus probable that this mechanism contributes to the threshold stress intensity K_{ISCC} .

A certain difficulty for a deeper investigation of the crack surface morphology is the corrosion during the test in high temperature water, which alters the surface behind the crack front. Polished micrographs of stress corrosion cracks show a crack tip which is filled up completely with oxides. The oxide growth rate at the outer surface of the specimen is small compared to the much higher corrosion rate at the crack tip, otherwise oxide layers of about 1 micron right behind the moving crack tip (about $1E-8m/s$) would not be achieved. To avoid crack tip blunting, the lateral corrosion must certainly be

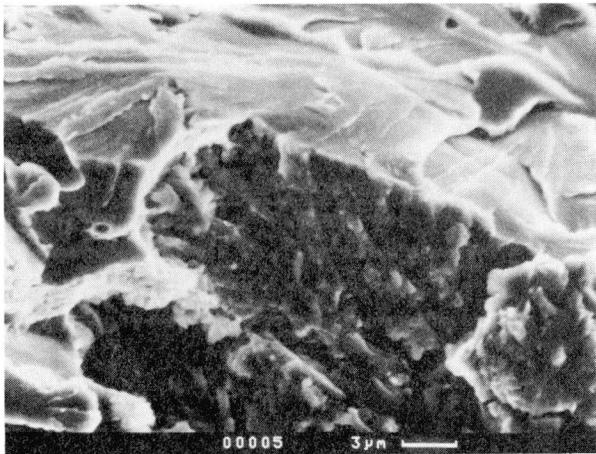


Fig. 46: Electron micrograph of the crack tip in a CT specimen of pressure vessel steel A508-II. Test conditions were deionized water at 240 °C

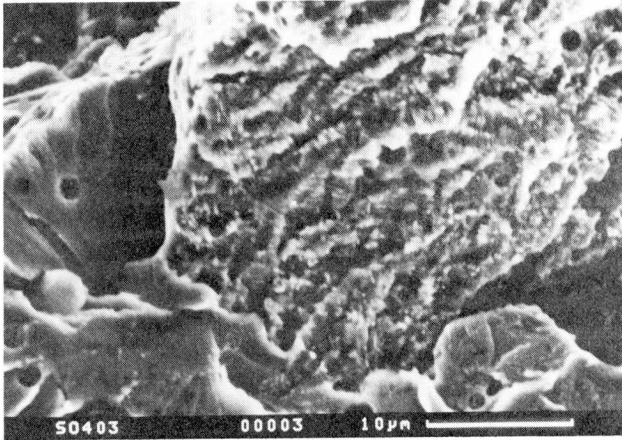


Fig. 47: Electron micrograph of the crack tip in a CT specimen of pressure vessel steel A508-II. Test conditions were deionized water at 240 °C. Oxides were chemically removed.

lower than the crack growth rate.

Figure 46 is an electron micrograph of the stress corrosion crack tip of a SA508-II CT-specimen, tested at 240 °C. To preserve the crack tip condition during stable stress corrosion crack growth as well as possible and to avoid corrosion at lower temperatures, a pressure valve was opened during the test and all of the water evaporated within a few minutes. The specimen was then broken open in liquid nitrogen. The surface seems to be heavily corroded already right behind the crack front. Propagation is not homogeneous but divided into smaller divisions of 1 to 3 microns.

To remove the oxides, the fracture surface was then cleaned potentiostatically in 17% HCl with additions of an organic inhibitor at a cathodic current density of 50 to 100 mA/cm² to avoid metal dissolution. As an additional feature of the crack surface, many striations with a spacing of about 0.5 microns are now visible near the crack tip as shown in figure 47. This implies that slip on crystallographic planes or brittle separation along slip planes are involved in the SCC mechanism.

6.2. Environmental and combined effects

6.2.1. Corrosion in high temperature water

In neutral and slightly alkaline high temperature water above 200 °C, duplex films grow on a steel surface according to a parabolic time law [90]. At low oxygen concentrations, the layers consist of magnetite, Fe₃O₄. The inner, protective layer is built of small equiaxed grains which grow at the oxide/metal interface and partly replace the parent metal. Direct oxidation is expected to occur with water:



The access of oxidant is possible by a certain porosity in the grain boundaries. Since the density of magnetite is only about one half of that of steel, the remainder of the replaced metal is oxidized and must diffuse through the inner layer. When the external solution is saturated, crystalline grains with the morphology of a precipitate build an outer layer which grows at the oxide solution interface. Due to the restricted transport conditions for the ferrous ions inside cracks, very large crystalline grains can be observed on the crack wall. Depending on the transport of hydrogen ions through the inner layer, between about 50 and 90 % of the hydrogen is produced at the metal surface, where a part of it may diffuse into the metal lattice.

The rate limiting step of metal loss is ascribed to a diffusion process. The details of the reaction system are still a matter of discussion but both diffusion of water molecules to the metal surface [92] as well as outward diffusion of ferrous ions [67] is considered to be the rate limiting process. A small porosity in the protective inner oxide layer and grain boundaries [93] offer diffusion paths for the transport of reaction products.

The measured weight loss of carbon steel in high temperature deionized water is quite low, e.g. at 310 °C, values below 0.01 mm/y (3E-13 m/s) were reported [91]. Even at higher corrosion potentials due to the presence of oxidizing species, stable passivity is observed until pitting markedly enhances the overall corrosion rate at still higher potentials. General corrosion in BWR water will thus not affect the durability of low alloy steel parts.

Due to the constraint growth of the oxide at the metal surface, lateral compressive stresses develop but porosity is preserved. It was argued that porosity is steadily introduced by creep processes [67]. The grain size of the inner layer oxide was given as about 0.1 μm. This size is about the lower limit for cleavage fracture according to the

Griffith criterion. It is therefore probable that the grain size is controlled by continuous fracture under a compressive stress up to this lower limit. This means that the grains will only break when the theoretical shear strength is reached. Under the very high stresses needed, creep will also contribute to the deformation process.

Considering a given crack, the difference in the oxide structure and the corrosion rate between the crack enclave and the outer surface will be small for low corrosion potentials, when the oxygen and hydrogen peroxide concentrations are kept at a very low level (below 1 ppb) in deionized water.

Conditions for high linear corrosion rates in carbon and low alloy steels can be found in acidified high temperature water below a pH of about 4. The corrosion process is still accompanied by oxide scales, which are however very thick, laminated and thus non-protective so that corrosion proceeds with a linear kinetic. The transition from protective to non-protective corrosion is strongly dependent on the pH and the solution composition. Acid chloride solutions [90] are best known to promote fast corrosion. It has been found that the corrosion rate is directly proportional to the H^+ concentration. The break-away behaviour of the oxide is attributed to a high porosity such that the rate limiting process is no longer diffusion of ferrous ions or water molecules but the interfacial oxidation rate of Fe to Fe_3O_4 . The oxide layer can become very thick then, containing most of the dissolved material.

In acidified solution, the oxide layer will fill up a narrow crevice within a short time, exerting a wedging force which eventually enhances the stress intensity at the tip of the crevice. It has been noted that the high oxide porosity is not closed even under a high compressive stress [94]. Interestingly, the activation energy for acid chloride non-protective corrosion was given as 40 kJmol^{-1} (for a constant H^+ activity). Activation energies for diffusion in water are generally lower, whereas charge transfer processes are characterized by an activation energy of 30 to 70 kJmol^{-1} [95].

Similar results as in acid chloride solutions were obtained in relatively concentrated $FeSO_4$ solutions (0.1M) at 200 to 280 °C with pressure vessel steel coupons. At 280 °C, the corrosion loss proceeds at a rate of about 3 to 5 E-9 m/s. Comparing with the fastest stress corrosion crack growth rates, this is still an order of magnitude lower. Also, such high ion concentrations are very unlikely and would lead to crack tip blunting and precipitations which should be seen on the crack surface in a later examination. The comparison of corrosion - and crack growth rates may however be misleading, since strains and restricted solution mobility at the crack tip surface can locally enhance the corrosion attack.

This stresses the need to get an idea of the chemomechanical interactions within these defects. Knowledge of the solution composition and the electrochemical reaction rates at the crack tip during SCC is of primary importance for the understanding of the environmental contribution to the crack growth mechanism. If crack growth rates could be measured as a function of a known crack tip electrolyte, important information on the basic mechanisms could be gained. As an indirect indicator, the relevance of the electrochemical potential at the external specimen surface has been shown in this work and it's well known that the chemical and electrochemical conditions inside an occluded cell can completely be altered compared to the bulk solution.

In oxygenated water, a potential drop develops due to oxygen depletion inside the crack and the strong effect of oxygen on the corrosion potential. The difference in the *electrochemical potential inside and outside the crack is responsible for the partial separation of oxydation and reduction sites. Metal which is not directly oxidised by water molecules to magnetite dissolves to ferrous ions, delivering two electrons which reduce oxygen at the outer surface through the reaction:*



Because of the high resistivity of deionized water, the potential drop down the crack remains high and may be around 500 mV [89].

Figure 48 depicts the important elements of the system, containing loads, material factors and environment.

It is almost impossible to measure the local solution composition within a pit or crack, but mathematical modeling offers a way to study the effect of different parameters. Generally, a mass conservation equation considering diffusion, migration, convection and chemical reactions is used for modeling and simplification of the system of interest. This mass conservation law can be written as follows [96]:

$$\frac{\partial c_i}{\partial t} + (\mathbf{v} \text{ grad})c_i = D_i \Delta c_i + \frac{D_i Z_i F}{RT} \text{div}(c_i \text{ grad } \Phi) + R_i \quad (21)$$

C_i is the volume concentration of the i th component, \mathbf{v} is a flow velocity field vector, Φ is the electric field potential, D_i is the coefficient of diffusion, Z_i the ionic valence and R_i is the reaction rate per volume of the i th component.

The equation simplifies for an equilibrium in the concentration gradient down the crack, so that the time variation and the net migration current of species i on the left side become zero. Further simplification is usually done by using the concentrations instead of

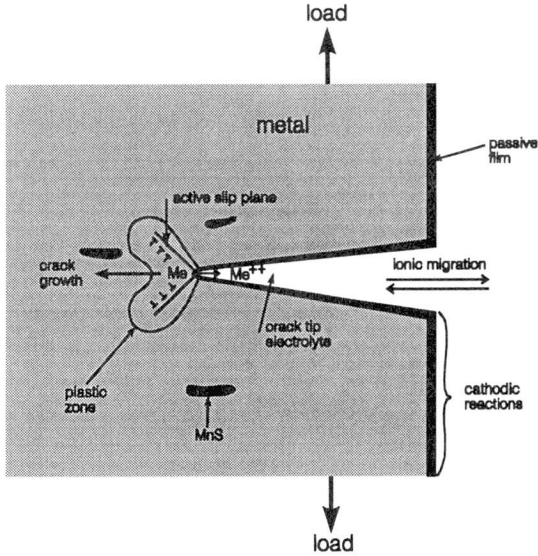


Fig. 48: Schematic drawing of the crack tip system

the activities and to confine the problem to one dimension (down the crack) only. A solution of the kind

$$\frac{c_1}{c_0} \propto e^{\Delta\Phi} \quad (22)$$

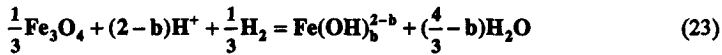
can be derived, which reveals that the crack tip anion concentration is strongly dependent on the external concentration c_0 and the difference in the corrosion potential between the crack mouth and the crack tip. Even in ultrapure water, dissolvable metallurgical impurities like MnS can lead to deleterious anion concentration levels.

Equation 21 is often used in crevice corrosion models which are aimed to the determination of a critical solution composition for local breakdown of passivity and the onset of corrosion attack. In numerical solutions, the incubation period is very sensitive to the given crevice depth and the local pH down the crevice or crack is also dependent on the gap width [97] which is influenced by corrosion products. Crevice corrosion models apply equally to stress corrosion cracking in high temperature water, with the important difference that due to the action of stresses, the critical solution composition is

less severe and the action of the corrosive medium is confined to a small process zone at the crack tip.

The major corrosion product which is detected on the stress corrosion fracture surface of a specimen in high temperature water is magnetite, which builds a several microns thick layer. Released Fe^{2+} from the corrosion process hydrolyses and builds one part of this layer as a precipitate.

The solubility of Fe_3O_4 is based on different hydrolyzed Fe^{2+} -species:



The solubility of magnetite has a minimum for slightly alkaline conditions and is proportional to the pH below about pH 5 [98]. Under acidic conditions, Fe^{2+} makes up most of the dissolved species. The temperature dependence of the solubility of magnetite in acidic water is given in figure 49. It's obvious that the temperature dependence is rather weak for a pH of 3 but increases towards neutral water. At a pH of 5, the solubility decreases more strongly from ambient temperature towards 300 °C.

The low solubility of magnetite results in the fact that dissolved iron precipitates near the location of dissolution and the acidic region will therefore be confined to a small volume at the crack tip. The degree of acidity which can be reached or which is necessary to

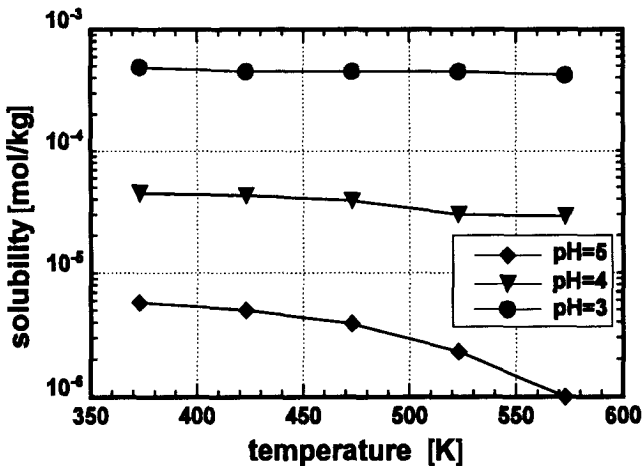


Fig. 49: Solubility of magnetite in water at high temperatures at different values of pH and 779 μm H_2 (from ref. 98). Given pH values apply to 298 K

make stress corrosion possible is still a matter of discussion.

Investigation of crack tip corrosion rates is generally done with a macroscopic version of the crack tip material and solution. Various techniques are used to access oxidation rates upon rupture of a protective film or to measure the influence of straining and solution composition. These techniques include slow or rapid straining or fracturing, scratching or electrochemical potential pulsing. There are however experimental shortcomings in all these techniques in the exact definition of the crack tip solution composition and potential as well as in the mass transport kinetics which is completely altered in a narrow crevice. Since low alloy steels express passivity in high temperature water, one expects to measure the repassivation current of the strained surface in potential pulsing tests, but mechano-chemical effects could also be involved.

Literature data on corrosion fatigue of pressure vessel steel in high temperature water gives some hints on the role of the crack tip chemistry. The mentioned transient behaviour of the crack growth rate in fatigue loading of fracture mechanics specimens in BWR water is reproducible and reversible with a hysteresis effect. This means that both transition from high to low growth rates and vice versa is not observed immediately upon a frequency change. Since strain rate will saturate relatively fast, solution chemistry within the crack must be responsible for the delay in both directions. Lowering the frequency from the high growth rate regime to below the threshold value, da/dN remains the same for some time, but da/dt is correspondingly lower, due to the lower frequency. An explanation for this behaviour can be given with the local crack tip chemistry which is influenced by the time based crack growth rate. Assumed that crack advance is proportional to the anodic dissolution rate at the crack tip (which doesn't mean that this is the main mechanism for crack growth), it follows that the mean current density is then inversely proportional to the raise time in a cycle and the total charge per load cycle is constant. Obviously, the current density change influences the solution chemistry at the crack tip and after some time, the chemical attack ceases and crack growth is mainly caused by mechanical fatigue.

Corrosion may contribute only a part to the crack growth but is clearly modulating it by producing the necessary solution composition. It's probable that surface oxide layers are involved in the strain rate dependent corrosion process by almost completely inhibiting enhanced anodic dissolution below the critical frequency, which would explain the threshold and the growth rates near the air base line. Otherwise, the change in dissolution current density with the crack tip strain rate is expected to be continuous, indicating that corrosion per se is not the mechanisms for crack growth.

In the opposite direction, exceeding the frequency threshold from a region of low to environmentally enhanced crack growth rates, da/dN remains low for many load cycles, but the higher time based growth rate changes the solution chemistry by exposing more fresh metal surface and by opening more MnS inclusions per unit of time. This will increase the acidity as well as the sulfide concentration, leading to stress corrosion cracking.

The constant load experiments of this work also showed that time dependent chemistry effects can be important for stress corrosion cracking. It was shown that the crack growth rate is strongly dependent on the corrosion potential and if the latter is changed, the growth rate follows with a certain delay. The delay time was seen to be shorter when the corrosion potential was lowered than in the opposite direction. There, several hours at a high corrosion potential were needed to re-establish the plateau growth rate from values below $1E-10$ m/s. It's most convincing to explain the delays with a chemistry change at the crack tip.

6.2.2. Critical corrosion potential

The crack growth rate data presented in this work clearly supports the idea of a critical potential for stable stress corrosion crack growth. Most of the available literature data on the influence of oxygen concentration and corrosion potential is based on SSRT. In deionized water at 288 °C, a critical potential of about -150 to -250 mV SHE was found for a low sulfur pressure vessel steel [63,99,114]. In this study, a value of about -100 mV was found at 288 °C for a medium sulfur steel. Considering also the stagnant water conditions and the higher conductivities of about 3 μ S/cm, the SSRT data yields a much more conservative critical potential.

Comparison of fracture mechanics tests and SSRT of plane tensile specimens is problematic. The stress/strain state is completely different due yielding of the whole specimen ligament.

Data for crack growth rates in fracture mechanics specimens at 288 °C and 200 \pm 100 ppb dissolved oxygen was compiled by Ford and Andresen [82] and is shown in figure 50 together with own results. These are divided into results from the refreshed water loop and from constant load tests conducted in stagnant autoclaves.

Above oxygen contents of about 1 ppm and a conductivity of 1 μ S/cm and more, growth rates from constant load and constant displacement experiments differ only slightly. Higher oxygen contents or conductivities will not give significantly higher growth rates. The two data points at 400 ppb oxygen indicate that below 1 ppm oxygen, besides the

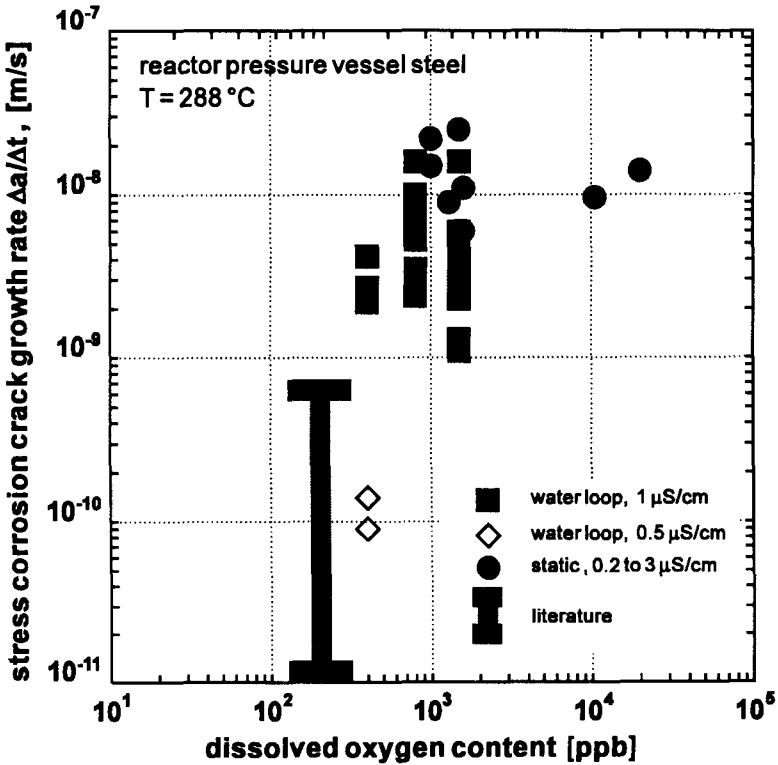


Fig. 50: Transgranular stress corrosion data of pressure vessel steel in deionized water at 288 °C.

oxygen content, also the conductivity is important for the susceptibility to stress corrosion cracking. It is therefore within a narrow field of oxygen content and conductivity, where a strong effect on the growth rate exists. This is certainly a cause for the very large scatter comparing results of different laboratories.

6.2.3. Effect of steel sulfur content

This leads us to a discussion of the effect of sulfur which has gained increasing interest in recent years.

Fatigue crack growth studies as well as SSRT in BWR and PWR water reveal a marked influence of the steel sulfur content on the SCC susceptibility. Below about 1 Hz, two crack growth regimes can be found and it was shown that steels which are high in the sulfur content (0.02%) suffer environmentally assisted cracking even in PWR water at low corrosion potentials [101].

The two crack growth rate regimes found in low frequency fatigue testing in light water environments can be reasonably understood in terms of the loading conditions and the sulfur content of the steel [103,104]. The transition from high to low crack growth rates adopts the character of a threshold, depending not only on the net sulfur content in the steel but also on the MnS size distribution.

MnS inclusions dissolve readily if access of high temperature water is possible [106]. The concentration of sulfur species in the crack is given by a balance between diffusion loss and dissolution of new particles intersected by the growing crack. High initial concentrations are possible in a freshly introduced fracture mechanics specimen, where MnS clusters intersected by the precrack dissolve during start up of the test. In BWR water, a difference in the electrochemical potential between outer surface and crack tip can lead to a steep concentration gradient of anions and is thus very effective to produce

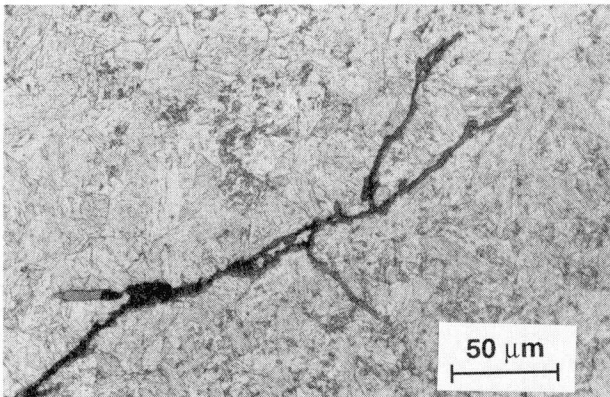


Fig. 51: Stress corrosion crack with a partially dissolved MnS particle. The test was conducted at 220°C and 3 ppm oxygen

and keep a high concentration of e.g. sulfide ions at the crack tip. Figure 51 depicts a part of a stress corrosion crack in a DCB specimen of alloy B, tested at 220 °C and 3 ppm oxygen in the water. The inclusion in the lower left corner was identified as MnS by EDX. The time since passage of the crack front was estimated to 10 to 12 hours. As can be seen, the inclusion is dissolved by about one third during this time.

After opening up a MnS particle there is thus a steady supply of sulphide during some time. This steady release of sulphides from the steel itself may thus be responsible for environmentally assisted cracking even in pure water.

The criterion of a critical sulfur concentration gives also a possible explanation for the absence of EAC in low sulfur steel (50 ppm) in clean BWR and PWR water.

The degree of sulfur release into the crack tip environment in a growing crack depends not only on the net volume content of MnS but also on the size, shape and local distribution of the second phase particles. Modeling the release rate on MnS [108] shows that particle size has a much larger effect on the crack tip concentration of sulphide than the overall content. This fact may explain differences in SCC susceptibility between steels with equal nominal sulfur content. Local inclusions clusters have been blamed for the high growth rates in PWR water expressed by medium to high sulfur pressure vessel steels. The MnS clusters provide an easy fracture path due to the low local ductility and decohesion of matrix and particles and are thus preferred initiation sites for EAC. Separation of matrix and inclusions occurs in the stress field ahead of the crack tip, building a crevice which is filled up upon entrance of water. Sulphide concentrations above 10000 ppm were estimated in dissolving clusters [109]. However, much lower crack tip hydrogen sulphide concentrations between 3 and 10 ppm were able to cause EAC in a low sulfur steel (0.004%S) in PWR water [101] yet reproducibility was poor. It appears therefore that the assumption of a critical crack tip sulfur concentration is difficult to approve and may simplify the real effect of sulfur in the SCC process.

To reveal the effect of sulfur species it seems most promising to investigate their influence on the build up and structure of the passive layer. Constant extension rate (CER) tests in H₂S polluted high temperature water showed that sulphide concentration below a certain threshold has no effect on the corrosion current, which rises slightly underproportional with the applied strain rate [103]. On the other side, the necessary concentration for a high and strain rate independent corrosion rate completely inhibits the growth of a passive layer and is thus not expected in a real stress corrosion crack (otherwise, much higher sulfur concentrations should be present on the crack surface).

However, at lower sulphide concentrations, SCC initiation and high crack growth rates have been measured in SSRT in PWR water at low potentials to simulate corrosion fatigue conditions. Both dissolved MnS [113] and sulphate [114] have proven to

decrease the critical potential for SCC down to values measured in oxygen free PWR water. It can therefore be concluded that the effect of sulphur on the repassivation kinetics of a plane surface is small in a range where SCC is already initiated. Measurement of repassivation kinetics on a plane surface is thus not appropriate to reflect the situation at an actual crack tip.

Thermodynamic calculations yield stability areas for possible corrosion products which are best represented in a Pourbaix diagram which shows the stable phases in relation to pH and the electrochemical potential, assuming fixed concentrations of dissolved species [110]. At higher sulfur ion activities, stable iron-sulphides are possible under deoxygenated conditions prevailing in the crack enclave. Iron sulphide has been detected on corrosion fatigue fracture surfaces at an amount of about 3%, but a correlation could not be found between detected surface sulfur concentration and steel susceptibility or dissolved sulphide concentration in the water [112]. A possible explanation for the deleterious effect of minor sulfur concentrations was given from Combrade et al who showed that adsorbed sulfur is stable and inhibits the formation of a dense magnetite layer [105].

6.2.4. Initiation of SCC

The SCC phenomenon is often divided into initiation and propagation. However, there must be a continuum between these two processes which is also a transition from a certain unpredictability to a quantitative and measurable damage of a structure. Most of the investigations on SCC deal with propagating cracks whereby initiation may occur not before 90 % of the lifetime of a service part. There is thus a strong interest to include the initiation process into a lifetime prediction model which is certainly complicated by the stochastic course of some single events. Initiation of SCC is a very localized process as confirmed by fractographic inspection of the fracture surface. Stress corrosion often spreads out from a point at the surface or at the actual crack tip line. In other fracture mechanics specimens, local initiation points cannot be determined at the precrack line and stress corrosion probably started at many adjacent points at the same time.

On plane specimens tested at a constant extension rate, pits are most often identified as initiation sites for the development of stress corrosion cracks [63,115,116]. Pitting corrosion in low alloy steels is observed even in deionized water when oxygen is present [17]. There is a threshold value for the oxygen concentration which is dependent on other environmental parameters like temperature and flow rate. As a major trend, susceptibility to pitting decreases with increasing temperature. In nominal BWR water at

288 °C and 200 ppb oxygen, pits are not observed on a plane surface. A high flowrate seems to suppress or retard crack initiation in low cycle fatigue experiments [117] which could also be related to decreased local corrosion attack at surface inhomogeneities.

An interesting point is the facilitated pit initiation on a strained surface which may arise from the rupture of the protective oxide and the resulting high local repassivation current densities. In this connection, outcropping MnS inclusions often serve as nucleation sites for pits [118] and SCC in SSRT, especially at the lower oxygen contents of about 200 ppb where MnS inclusions are probably the only site where stress corrosion cracks start to grow [119]. It has been shown that pre-exposure of tensile specimens to the high temperature test environment for some hours to several days causes a decrease in the number of cracks on the fracture surface [119] and in the fraction of the SCC area [120], which indicates that outcropping MnS inclusions have dissolved and the left cavities do not act any more as initiation sites for SCC. This problem is however not addressed in most of the literature data based on slow strain rate testing.

The mechanism of crack initiation at MnS inclusions is obviously bound to a plastic strain limit of several percent, as reported from SSRT conducted at 160 [121] 230 [115] and 288 °C [122]. MnS itself has a high plasticity at all temperatures [123] which is very favourable for machining of steel parts. However, under conditions of tensile stress, voids form at the sulphide/ferrite interface due to the weak nature of the interfacial bonding. Beginning void formation is observed after a small plastic deformation and growth proceeds with increasing strain until the onset of void coalescence which finally results in ductile rupture [124]. Upon access of water in the small crevice between inclusion and steel matrix, a high initial current density is expected at the virgin steel surface, accompanied by a release of sulphide from the inclusion. Sulphides, oxygen depletion and hydrolysis of metal ions lead to an acidification of the crevice solution. The further steps of the initiation process are still a matter of discussion. Both hydrogen embrittlement and anodic dissolution may be involved in crack initiation and propagation since both mechanisms are favoured by the aggressive crack tip solution.

The high plastic strain limit for SCC initiation at oxygen concentrations around 200 to 400 ppb seems to be lowered by higher oxygen concentrations. Constant load tests at 288 °C and 8 ppm oxygen indicate that SCC initiates right beyond the linear elastic strain limit [116].

Setting a threshold for the degree of macroscopic strain required for initiation of SCC can be misleading since local microplastic events in corrosion related grooves or pits may occur even below the linear elastic strain limit. It's therefore not appropriate to distinguish between stress-induced SCC with a macroscopic strain rate ≤ 0 and strain-induced SCC observed only with a positive overall strain rate since local strain can be

operative in both cases although the necessary degree for SCC initiation can largely vary between different systems.

In precracked fracture mechanics specimens, SCC initiation is confined to the crack tip and again, the role of strain and strain rate can not be exactly evaluated due to creep processes. The case of wedge loaded specimens used in the recirculation loop will be discussed in more detail.

These specimens were loaded to a constant load line displacement the day before insertion into the autoclaves and then stayed overnight in cold oxygen free water. After loading, a positive creep strain rate is expected at the crack tip but this will quickly fall to negligible values. A high stress level is sustained ahead of the crack tip which can be estimated to lie between the yield strength for plane stress conditions and about three times the yield strength for plane strain conditions [125]. The distance between peak stress and crack tip is only about twice the crack tip opening displacement.

Heating up from room temperature to 288 °C, yield strength and Young's modulus decrease both by approximately 10%. It's therefore expected that the near-crack tip residual stress will relax somewhat, inducing some additional strain at the crack tip. This strain may well be responsible for stress corrosion crack initiation during or immediately after heating-up of the recirculation loop. A further requirement for crack initiation will be the electrochemical equilibrium potential which should be reached as fast as possible, to establish the necessary crack tip chemistry. Relaxation is confirmed by the decrease of the load line displacement by approximately 2 to 5 % during a test.

Current experience with wedge loaded specimens shows that an increase of the load line displacement by 10% at room temperature, after a test cycle without SCC in the respective specimen, can be responsible for the cracking during the next test. As described, stress corrosion was first observed in test number 7, with the same environmental conditions as in test 5 and 6. However, test 6 was done by reinsertion of the specimens from test 5, without additional loading. The absence of SCC is then explainable by the exhausted creep at 288 °C which is not 'revived'.

However, there is no evidence for crack initiation taking place exclusively at the beginning of a test and investigations on this problem have not been conducted so far since in situ crack growth measurements are generally conducted only during experiments with controlled load. Lately, Hanninen et al [107] found stress corrosion cracking in a bolt loaded specimen in PWR water which initiated most likely during a chemistry transient. At this time, significant crack blunting and stress relaxation had taken place and crack initiation was possible by a local corrosion attack.

The problem of crack initiation times is addressed especially for small crack in the order of a tenth of a millimeter as was seen in test 17 and 18 on one specimen only. Citation of this crack as a uniform crack growth rate may give misleading results.

Several observations confirm that the crack tip oxide film plays an important role at least for the initiation process of stress corrosion cracking. In all constant load tests conducted so far, crack growth did not start at constant load when the corrosion potential was raised to a level far above E_{crit} . Triggering SCC was then successful with a comparatively small load increase of only a few percent of the total load. Before the slight load increase, the crack tip was therefore protected by a oxide layer and due to creep exhaustion, fast initiation was not probable. The absence of SCC initiation after e.g. some days may not be understood as an assurance against SCC. In several tests conducted under constant load, SCC started only several hours (up to 24 hours) after the load increase, when the additional creep strain was almost exhausted. Moreover, corrosion at the crack tip proceeds at a certain level even at the passivated surface and a MnS particle may be reached after some time. From an engineering point of view it's acceptable that stress corrosion initiates at some places but does not propagate. For this reason, critical corrosion potentials and conductivities are certainly most important for practical applications.

The constant load tests conducted with decreasing and increasing potentials have shown that a fast crack growth rate can be re-established from unmeasurable rates with a hysteresis effect because the change of the crack tip chemistry runs behind the potential change at the outer surface of the specimen. The question whether these cracks had really completely stopped can not conclusively be answered, but sustained growth rates of about $1E-10$ m/s seem to be possible, which however questions the concept of a threshold crack growth rate for sustained stress corrosion cracking.

7. References

- [1] H.J. Engell, M.O. Speidel, "Ursachen und Mechanismen der Spannungsrisskorrosion", Werkstoffe und Korrosion, Vol. 20, No. 4, 1969
- [2] "Spannungsrisskorrosion von Stahl in Wasser", M.O. Speidel, R.M.Magdowski, P.J. Uggowitzer, eds., Ergebnisse der Werkstofforschung, Vol. 2, Verlag Thubal-Kain, 1988
- [3] "Stress Corrosion Cracking of Carbon and Low Alloy Steels", in: "Metal corrosion and protection technology", M. Kowaka, ed., Allerton Press, New York, 1990
- [4] F.P. Ford, "Stress Corrosion Cracking", in: "Corrosion Processes", R.N. Parkins, ed., Applied Science Publishers, LTD, 1982
- [5] "Stress Corrosion Cracking - New Approaches", H.L. Craigh Jr., ed., ASTM STP 610, American Society for Testing and Materials, Philadelphia, 1976
- [6] "Advances in Corrosion Science and Technology", M.G.Fontana, R.W.Staehle, eds., Vol. 1-7, Plenum Press, New York, 1970-1980
- [7] H.L. Logan, "The Stress Corrosion of Metals", John Wiley & Sons, New York, 1966
- [8] "Atlas of Stress-Corrosion and Corrosion Fatigue of Metals", A.J. McEvily, Jr., ed., ASM International, Materials Park, Ohio, 1990
- [9] S.H. Bush, R.L. Dillon, "Stress Corrosion in Nuclear Systems", Stress Corrosion Cracking and Hydrogen Embrittlement of Iron Base Alloys", Nace-5, National Association of Corrosion Engineers, Library of Congress, 1977
- [10] S.H. Bush, "Failure Mechanism in Nuclear Power Plant Piping Systems", J. of Pressure Vessel Technology, Vol. 114, No. 4, 1992
- [11] T.U. Marston, R.L. Jones, "Materials Degradation Problems in the Advanced Light Water Reactors", Proc. Fifth International Symposium on Environmental Degradation of Materials in Nuclear Power Systems-Water Reactors, Monterey, CA, 1991

- [12] E. Lenz, N. Wieling, "Strain-Induced Cracking of low alloy steels in LWR Systems-Interpretation of susceptibility by means of a three-dimensional (T, ϵ , dissolved oxygen) diagram", Nuclear Engineering and Design, Vol 91, 1986
- [13] C.J. Czajkowski, "Evaluation of Transgranular Cracking Phenomenon on the Indian Point No. 3 Steam Generator Vessel", Int. J. Pressure Vessels and Piping, Vol. 26, 1986
- [14] B.Vyas, C.J. Czajkowski, J.R. Weeks, "Metallurgical examination of cracked feedwater pipes from nine pressurized water reactors", Nuclear Technology, Vol. 55, 1981
- [15] W.H. Bamford, "The Influence of Environment on Fatigue", Inst. of Mech. Eng., London, 1977
- [16] P.H. Effertz, P. Forchhammer, J.Hickling, "Spannungskorrosionsschäden an Bauteilen in Kraftwerken - Mechanismen und Beispiele", VGB Kraftwerkstechnik, Vol. 62, 1982
- [17] J. Hickling, D. Blind, "Strain-Induced Corrosion Cracking of Low-Alloy Steels in Light-Water Reactor Systems - Case Histories and Identification of Conditions Leading to Susceptibility", Nuclear Engineering and Design, Vol. 91, 1986
- [18] T.Shoji, K. Kiuchi, T. Kondo, "Materials Compatibility with High Temperature Waters and Long Term Stability in Nuclear Reactor Environments", Proc. Fourth International Symposium on Environmental Degradation of Materials in Nuclear Power Systems-Water Reactors, Jekyll Island, GA, 1989
- [19] T. Kondo, H. Nakajima, R. Nagasaki, "Metallographic investigation on the cladding failure in the pressure vessel of a BWR", Nuclear Engineering and Design, Vol. 16, No. , 1971
- [20] R. Magdowski, A. Kraus, M.O. Speidel, "Stress Corrosion Cracking of Reactor Pressure Vessel Steel in 288 °C Water: The Effect of Oxygen, Electrochemical Potential, and Steel Composition"; Corrosion 94, Paper No. 133, NACE
- [21] A.W. Loginow, "Stress Corrosion Testing of Alloys", Mater. Protection, Vol. 5, No. 5, 1966

- [22] D.O. Sprowls, "Evaluation of Stress Corrosion Cracking", Metals Handbook Ninth Edition, Vol. 13, ASM International, 1987
- [23] A.J. Sedriks, "Stress Corrosion Cracking Test Methods", National Association of Corrosion Engineers, 1990
- [24] "Environment-Sensitive Fracture: Evaluation and Comparison of Test Methods", S.W. Dean, E.N. Pugh, G.M. Ugiansky, eds., ASTM STP 821, American Society for Testing and Materials, Philadelphia, 1984
- [25] "Stress Corrosion Cracking, Materials Performance and Evaluation", R.H. Jones, Ed., ASM International, Materials Park, Ohio, 1992
- [26] R.N. Parkins, "A Critical Evaluation of Current Environment-Sensitive Fracture Test Methods", Environment-Sensitive Fracture: Evaluation and Comparison of Test Methods, ASTM STP 821, American Society for Testing and Materials, 1984
- [27] "Stress Corrosion Cracking - The Slow Strain Rate Technique", ASTM STP 665, American Society of Testing and Materials, 1979
- [28] R.N. Parkins, "Environment Sensitive Fracture and its Prevention", British Corrosion Journal, Vol. 14, No. 1, 1979
- [29] A. Turnbull, "Test Methods for Environment Assisted Cracking", British Corrosion Journal, Vol. 27, No. 4, 1992
- [30] Metals Handbook Ninth Edition, Vol. 1, Properties and Selection: Irons and Steels, American Society for Metals, 1978
- [31] "Standard Test Method for J_{IC} , A Measure of Fracture Toughness" ASTM E813-89, 1992 Annual Book of ASTM Standards, Vol. 3.01
- [32] P. Sigrist, private communication
- [33] "Standard Test Method for Plane-Strain Fracture Toughness of Metallic Materials," ASTM E399-90, 1992 Annual Book of ASTM Standards, Vol. 3.01
- [34] M.O. Speidel, "Bruchmechanik und Spannungsrisskorrosion", Blech, Rohre, Profile, Vol. 25, No. 1, 1978

- [35] "Stress Intensity Factors Handbook," Y. Murakami, ed., Pergamon Press, 1987
- [36] H. Tada, P. Paris, G. Irwin, "The Stress Analysis of Cracks Handbook," Del Research Corporation, St. Louis, Missouri, 1979
- [37] G.R. Irwin, "Analysis of Stresses and Strains Near the End of a Crack Traversing a Plate," *J. Appl. Mech.*, Vol. 24, 1957
- [38] S. Mostovoy, P.B. Crosley, E.J. Ripling, "Use of Crack-Line-Loaded Specimens for Measuring Plane Strain Fracture Toughness," *J. of Mat.*, Vol. 2, No. 3 (9), 1967
- [39] R.M.L. Foote, V.T. Buchwald, "An Exact Solution for the Stress Intensity Factor for a Double Cantilever Beam," *Int. J. Fracture*, Vol. 29, 1985
- [40] B.F. Brown, "Stress-Corrosion Cracking in High Strength Steels and in Titanium and Aluminium Alloys," Naval Research Laboratory, Washington D.C., 1972
- [41] B. Stellwag, H. Kaesche, "Revised Compliance Technique for Crack Growth Studies with Modified DCB Test Pieces," *Int. J. of Fracture*, Vol. 14, 1978
- [42] J. Srawley, B. Gross, "Stress Intensity Factors for Crackline-Loaded Edge-Crack Specimens", *Mater.Res. Stand.*, Vol.7, No. 4, 1967
- [43] "Deformation and Fracture Mechanics of Engineering Materials," R.W. Hertzberg, ed., John Wiley & Sons, New York, 1976
- [44] D.D Macdonald, "Reference Electrodes for High Temperature Aqueous Systems-A Review and Assessment," *Corrosion*, Vol. 34, No. 3, 1978
- [45] M.J. Danielson, "The Construction and Thermodynamic Performance of an Ag-AgCl Reference Electrode for Use in High Temperature Aqueous Environments Containing H₂ and H₂S," *Corrosion*, Vol. 35, No. 5, 1979
- [46] P.L. Andresen, "Innovations in Experimental Techniques for Testing in High-Temperature Aqueous Environments," General Electric Report No. 81CRD088, May 1981
- [47] M.J. Danielson, "A Long-Lived External Ag/AgCl Reference Electrode for Use in High Temperature/Pressure Environments," *Corrosion*, Vol. 39, No. 5, 1983

- [48] D.D. Macdonald, A.C. Scott, P. Wentrcek, "Silver-Silver Chloride Thermocells and Thermal Liquid junction Potentials for Potassium Chloride Solutions at Elevated Temperatures," *J. Electrochem. Soc.*, Vol. 126, No. 9, 1979
- [49] D.D. Macdonald, A.C. Scott, P. Wentrcek, "External Reference Electrodes for Use in High Temperature Aqueous Systems," *J. Electrochem. Soc.*, Vol. 126, No. 6, 1979
- [50] R.S. Greeley, W.T. Smith, R.W. Stoughten, M.H. Lietzke, "Electromotive Force Studies in Aqueous Solutions at Elevated Temperatures. 1. The Standard Potential of the Silver-Silver Chloride Electrode," *J. Phys. Chem.*, Vol. 64, 1960
- [51] R. Battino, T.R. Rettich, T. Tominaga, "The Solubility of Oxygen and Ozone in Liquids," *J. Phys. Chem. Ref. Data*, Vol. 12, No. 2, 1983
- [52] "Properties of Water and Steam in SI-Units," ed. U. Grigull, Springer, 1982
- [53] J. Bosholm, "Beschreibung des Verhaltens gasförmiger Stoffe im System Wasser/Dampf," *Kernenergie*, Vol. 26, No. 5, 1983
- [54] G. Maurer, "On the Solubility of Volatile Weak Electrolytes in Aqueous Solutions," *Thermodynamics of Aqueous Systems with Industrial Applications*, American Chemical Society Symposium Series 133, Washington, 1980
- [55] H.L. Clever, C.H. Han, "The Solubility of Gases in Water from 350-600 K," as Ref. 54
- [56] R. Winkler, H. Lehmann, "Zur Qualitätssicherung Oxidischer Korrosionsschutzschichten", *VGB Kraftwerkstechnik*, Vol. 65, Nr. 4, 1985
- [57] D.D. MacDonald, M. Urquidi-MacDonald, "Thin-Layer Mixed-Potential Model for the Corrosion of High-Level Nuclear Waste Canisters", *Corrosion*, Vol. 46, No. 5, 1990
- [58] D.D. MacDonald, "Calculation of Corrosion Potentials in Boiling Water Reactors", *Proc. Fifth International Symposium on Environmental Degradation of Materials in Nuclear Power Systems-Water Reactors*, Monterey, CA, 1991

- [59] B. Rosborg, A. Molander, "The Corrosion Potential of Type 304 Stainless Steel in Swedish LWRs During Steady Reactor Operation", Proc. Second International Symposium on Environmental Degradation of Materials in Nuclear Power Systems-Water Reactors, Monterey, CA, 1985
- [60] J. Leibovitz W.R. Kassen, "W.L. Pearl, S.G. Sawochka, "Improved Electrodes for BWR In-Plant Monitoring", Research Project 706_1, EPR NP 2524, July 1982
- [61] M.E. Indig, "Technology Transfer: Aqueous Electrochemical Measurements Room Temperature to 290 °C", Corrosion, Vol. 46, No. 8, 1990
- [62] C.C. Lin, F.R. Smith, N. Ichikawa, M. Itow, "Electrochemical Potential Measurements under Simulated BWR Water Chemistry Conditions", Corrosion, Vol. 48, No. 1; 1992
- [63] P. Hurst, D.A. Appleton, P. Banks, A.S. Raffel, "Slow Strain Rate Stress Corrosion Tests on A508-3 and A533B Steel in De-Ionized and PWR Water at 563 K", Corrosion Science, Vol. 25, No. 8/9, 1985
- [64] P. Ford et al., "Application of Water Chemistry Control, On-Line Monitoring and Crack Growth Rate Models for Improved BWR Materials Performance", Proc. Fourth International Symposium on Environmental Degradation of Materials in Nuclear Power Systems-Water Reactors, Jekyll Island, Georgia, 1989
- [65] G. Gabetta, E. Caretta, "Corrosion-Potential Measurements Inside and Outside a Growing During Environmental Fatigue Tests at 288 °C, with Different Oxygen Contents", Corrosion Chemistry within Pits, Crevices and Cracks, A. Turnbull ed. HMSO, London, 1987
- [66] L.W. Niedrach, W.H. Stoddard, "Corrosion Potentials and Corrosion Behaviour of AISI 304 Stainless Steel in High Temperature Water Containing Both Dissolved Hydrogen and Oxygen", Corrosion, Vol. 42, No. 12, 1986
- [67] J. Robertson, "The Mechanism of High Temperature Aqueous Corrosion of Steel", Corrosion Science, Vol. 29, No. 11/12, 1989

- [68] P.M. Scott, "A Review of Environmental Effects on Pressure Vessel Integrity", Proc. Third International Symposium on Environmental Degradation of Materials in Nuclear Power Systems-Water Reactors, Traverse City, Michigan, 1987
- [69] J.H. Bulloch, "Understanding and Eliminating of Crack Extension Behaviour in Feed Water Dearthor Systems- A Critical Review", Int. Journal of Pressure Vessels and Piping, Vol. 53, Nr. 1, 1993
- [70] V.G. Levich, "Physicochemical Thermodynamics", Prentice Hall, 1962
- [71] F.P. Ford, P.W. Emigh, "The Prediction of the Maximum Corrosion Fatigue Crack Propagation Rate in the Low Alloy Steel-De-Oxygenated Water System at 288°C", Corrosion Science, Vol.25, No. 8/9, 1985
- [72] T. Ishihara, S. Ohashi, "Effects of Environmental Factors on Stress Cracking for JIS STS 42 Carbon Steel in Hot Water", Corrosion Eng., Vol. 37, No. 8, 1988
- [73] M. Ullberg, "On Corrosion Potential Measurement in BWRs", Proc. Fourth International Symposium on Environmental Degradation of Materials in Nuclear Power Systems-Water Reactors, Jekyll Island, Georgia, 1989
- [74] Electrical Power Research Institute (EPRI), "Guideline for water chemistry in nuclear power plants".
- [75] R. Magdowski, "Stress Corrosion Cracking of Low Alloy Steel in Water", Doctoral Thesis ETHZ, Switzerland, 1987
- [76] M.O. Speidel, R.M. Magdowski, "Stress Corrosion Cracking of Nuclear Reactor Pressure Vessel and Piping Steel", Intern. J. Pressure Vessels and Piping, Vol. 34, 1988
- [77] B. Iskluth, "Beitrag zur Spannungsrissskorrosion am Beispiel eines niedriglegierten warmfesten Feinkornbaustahles in sauerstoffhaltigem Hochtemperaturwasser", Diss. MPA Stuttgart, 1989
- [78] E. Tenckhoff, M. Erve, E. Lenz, G. Vazoukis, "Environmental Assisted Crack Growth in Low Alloy Steels - Results and their Relevance to LWR Components", Nuclear Eng. and Design, Vol. 119, 1990

- [79] V. Läßle, P. Deimel, "Einfluss von Korrosion und mechanischer Belastung auf das Risswachstum niedriglegierter, ferritischer Stähle in sauerstoffhaltigem Hochtemperaturwasser", Dechema-Jahrestagung 1993, Poster Nr. 7.19, 26.-28 Mai 1993, Nürnberg
- [80] K. Matocha, V. Hluchan, J. Wozniak, I. Jiricek, "Environmentally Assisted Cracking of Steam Generator Pressure Vessel Steel in High Temperature Water", Proc. of Second International Atomic Energy Agency Specialists Meeting on Subcritical Crack Growth, Moscow, USSR, May 1990
- [81] D.D. Macdonald, H. Song, K. Makela, K. Yoshida, "Corrosion Potential Measurements on Type 304 SS and Alloy 182 in Simulated BWR Environments", Corrosion, Vol. 49, No. 1, 1993
- [82] F.P. Ford, P.L. Andresen, D. Weinstein, S. Ranganath, R. Pathania, "Stress corrosion Cracking of Low-Alloy Steels in High Temperature Water", Proc. Fifth International Symposium on Environmental Degradation of Materials in Nuclear Power Systems-Water Reactors, Monterey, California, 1991
- [83] R. Attinger, Private Communication
- [84] R.N. Parkins, "Strain Rate Effects in Stress Corrosion Cracking", Corrosion, Vol. 46, No. 3, 1990
- [85] R.C. Newman, M.Saito, "Anodic Stress-Corrosion Cracking: Slip-Dissolution and Film-Induced Cleavage", Int. Conf. on Corrosion-Deformation Interactions CDI'92, Fontainebleau, Oct. 5-7, 1992
- [86] F.P. Ford, "Modelling of Environmentally-Assisted Cracking of Structural Steels in Water", Umgebungsabhängiges Bruchverhalten, Eds. M. Sharper, J. Barthel, DGM 1990
- [87] T. Shoji, H. Takahashi, "Role of Loading Variables in Environmental Enhanced Crack Growth for Water Cooled Nuclear Reactor Pressure Vessels", International Atomic Energy Agency Specialists Meeting on Subcritical Crack Growth, Freiburg, 1981
- [88] R.N. Parkins, "Environment-Sensitive Fracture - Controlling parameters", Proc. 3rd International Conference on Mechanical Behaviour of Materials, Cambridge, 1979

- [89] Final Report of EPRI Research Project "Environmentally-Controlled Cracking of Stainless and Low-Alloy Steels in Light Water Reactor Environments", EPRI Contract RP2006-6, 1985
- [90] E.C Potter, G.M.W. Mann, "The Fast Linear Growth of Magnetite on Mild Steel in High-Temperature Aqueous Conditions", *British Corrosion Journal*, Vol. 1, No. 1, 1965
- [91] H.S. Gadiyar, N.S.D. Elayathu, "Corrosion and Magnetite Growth on Carbon Steels in Water at 310°C - Effect of Dissolved Oxygen, pH and EDTA Addition", *Corrosion*, Vol. 36, No. 6, 1980
- [92] P.L. Andresen, "Modeling of Water and Material Chemistry Effects on Crack Tip Chemistry and Resulting Crack Growth Kinetics", *Proc. Third International Symposium on Environmental Degradation of Materials in Nuclear Power Systems-Water Reactors*, Traverse City, Michigan, 1987
- [93] J. Robertson, M.I. Manning, "Criteria for Formation of Single Layer, Duplex, and Breakaway scales on Steels", *Materials Science and Technology*, Vol. 4, No. 12, 1988
- [94] J. Robertson, J.E. Forrest, "Corrosion of Carbon Steels in High Temperature Acid Chloride Solutions", *Corrosion Science*, Vol. 32, No. 5/6, 1991
- [95] J.M. West, "Basic Corrosion and Oxidation", Ellis Horwood, 1986
- [96] G.P. Cherepanov, "Mechanics of Brittle Fracture", McGraw-Hill, 1979
- [97] M.K. Watson, J. Postlethwaite, "Numerical Simulation of Crevice Corrosion: the Effect of the Crevice Gap Profile", *Corrosion Science*, Vol. 32, No. 11, 1991
- [98] P.R. Tremaine, J.C. LeBlanc, "The solubility of Magnetite and the Hydrolysis and Oxidation of Fe^{2+} in Water to 300 °C", *Journal of Solution Chemistry*, Vol. 9, No. 6, 1980
- [99] J. Congleton, T. Shoji, R.N. Parkins, "The Stress Corrosion Cracking of Reactor Pressure Vessel Steel in High Temperature Water", *Corrosion Science*, Vol. 25, No. 8/9, 1985

- [100] W.A. Van Der Sluys, R.H. Emanuelson, "Cyclic Crack Growth Behaviour of Reactor Pressure Vessel Steels in Light Water Reactor Environments", *Journal of Engineering Materials and Technology*, Vol. 108, No. 1, 1986
- [101] W.A. Van Der Sluys, R.H. Emanuelson, "Enhancement of Fatigue Crack Growth Rates in Pressure Boundary Materials due to Light-Water-Reactor Environments", *Proc. Third International Symposium on Environmental Degradation of Materials in Nuclear Power Systems-Water Reactors*, Traverse City, Michigan, 1987
- [102] W.A. Van Der Sluys, R.H. Pathania, "Studies of Stress Corrosion Cracking in Steels Used for Reactor Pressure Vessels", *Proc. Fifth International Symposium on Environmental Degradation of Materials in Nuclear Power Systems-Water Reactors*, Monterey, Cal., 1991
- [103] P. Combrade, M. Foucault, G. Slama, "Effect of Sulfur on the Fatigue Crack Growth Rates of Pressure Vessel Steel Exposed to PWR Coolant: Preliminary Model for prediction of the Transitions Between High and Low Crack Growth Rates", as Ref. 101
- [104] P. Combrade, F. Foucault, "Crack Tip Conditions Related to Environmentally Assisted Cracking in Pressure Vessel Steels: Effect of Temperature", *Proc. Fifth International Symposium on Environmental Degradation of Materials in Nuclear Power Systems-Water Reactors*, Monterey, Cal., 1991
- [105] P. Combrade, F. Foucault, P. Marcus, G. Slama, "On the Role of Sulfur on the Dissolution of Pressure Vessel Steels at the Tip of a Propagating Crack in PWR Environments", as ref. 73
- [106] K. Klemetti, H. Hänninen, K. Törrönen, M. Kemppainen, M. Pessa, "On the Role of Inclusions in Environment Sensitive Cracking of Reactor Pressure Vessel Steels", *Proc. International Symposium on Environmental Degradation of Materials in Nuclear Power Systems-Water Reactors*, Myrtle Beach, South Carolina, 1983
- [107] H. Hänninen, P. Aaltonen, U. Ehrnstén, E. Arilahti, "Stress Corrosion Cracking of Low Alloy Steel Weldments in LWR Environments", *Proc. Sixth International Symposium on Environmental Degradation of Materials in Nuclear Power Systems-Water Reactors*, San Diego, Cal., 1993 (to be published)

- [108] D.I. Swan, O.J. Chapman, "Modeling of Sulfide Inclusion Distributions in Relation to the Environmentally Assisted Cracking of Low-Alloy Steels in a Pressurized Water Reactor Environment", Environmentally Assisted Cracking: Science and Engineering, ASTM STP 1049, W.B. Lisagor, T.W Crooker, B.N. Leis, Eds., American Society for Testing and Materials, 1990
- [109] J.H. Bulloch, J.D. Atkinson, "An Assessment of the Influence of Sulphide Distribution in the Promotion of Environmentally Assisted Crack Growth in Ferritic Pressure Vessel Steels", 18. MPA-Seminar, Safety and Reliability of Plant Technology with Special Emphasis on Nuclear Technology", Staatl. Materialprüfanstalt Universität Stuttgart, 1992
- [110] C.M. Chen, K. Aral, "Computer-Calculated Potential pH Diagrams to 300°C", EPRI NP-3137, Vol. 3, 1983
- [111] F.P. Ford, "Overview of Collaborative Research into Mechanisms of Environmentally Controlled Cracking in the Low Alloy Pressure Vessel Steel/Water System", Proc. of IAEA Specialists meeting on Subcritical Crack Growth, Sendai, Japan, 1985
- [112] H. Hanninen, M. Vulli, W.H. Cullen, "Study of Corrosion Products on Fatigue Fracture Surfaces of Pressure Vessel Steels Tested in PWR Environments by Using X-Ray Photoelectron and Auger Electron Spectroscopies", Proc. Third International Symposium on Environmental Degradation of Materials in Nuclear Power Systems-Water Reactors, Traverse City, Michigan, 1987
- [113] H. Hänninen, W. Cullen, M. Kemppainen, "Effects of MnS Inclusion Dissolution on Environmentally Assisted Cracking in Low-Alloy and Carbon Steels", Corrosion, Vol. 46, No. 7, 1990
- [114] T. Shoji, H. Takahashi, S. Aizawa, M. Saito, "Effects of Sulfate Contamination, Sulfur in Steel and Strain Rate on Critical Cracking Potential for SCC of Pressure Vessel Steels in Pressurized High Temperature Waters", as Ref. 101
- [115] M.E. Indig, J.E. Weber, D. Weinstein, "Environmental Aspects of Carbon Steel Stress Corrosion in High Purity Water", Reviews on Coating and Corrosion, Vol. 5, 1982

- [116] J. Kuniya, I. Masaoka, R. Sasaki, H. Itoh, T. Okazaki, "Stress Corrosion Cracking Susceptibility of Low Alloy Steels Used for Reactor Pressure Vessels in High Temperature Oxygenated Water", *J. of Pressure Vessel Technology*, Vol. 107, No. 11, 1985
- [117] J. Hickling, Lecture at the ICG-EAC Meeting, Villigen, CH, 11 March 1992
- [118] G. Eklund, "On the Initiation of Corrosion on Carbon Steel", *Scand. J. of Metallurgy*, Vol. 1, No. 6, 1972
- [119] J. Kuniya, H. Anzai, I. Masaoka, "Effect of MnS Inclusions on Stress Corrosion Cracking in Low-Alloy Steels", *Corrosion*, Vol. 48, No. 5, 1992
- [120] T. Mizuno, S. Pednakar, Z. Szlarska-Smialowska, D.D. Macdonald, "Corrosion and Stress Corrosion Cracking of Carbon Steel in Oxygenated, High-Purity Water at Elevated Temperatures", *Proc. International Symposium on Environmental Degradation of Materials in Nuclear Power Systems-Water Reactors*, Myrtle Beach, South Carolina, 1983
- [121] K. Rippstein, H. Kaesche, "The Stress Corrosion Cracking of a Reactor Pressure Vessel Steel in High Temperature Water at High Flow Rates", *Corrosion Science*, Vol. 29, No. 5, 1989
- [122] H. Gladen, H. Kaesche, "SCC of slowly strained Mild Steel in High Pressure, High Temperature Water", 18. MPA-Seminar, Stuttgart, 1992
- [123] R. Kiessling, N. Lange, "Non-Metallic Inclusions in Steel", *The Metals Society*, London, 1978
- [124] "Sulfide Inclusions in Steel", *ASM Materials/Metalworking Technology Series*, No. 6, Metals Park, Ohio, USA, 1975
- [125] J.R. Rice, "Mechanics Aspects of Stress Corrosion Cracking and Hydrogen Embrittlement", in "Stress Corrosion Cracking and Hydrogen Embrittlement of Iron Base Alloys", R.W. Staele, J. Hochmann, R.D. McCright, J.E. Slater, eds., NACE-5, National Association of Corrosion Engineers, 1977
- [126] D.J. Duquette, "Chemo-Mechanical Interactions in Environmentally Induced Cracking", *Corrosion*, Vol. 46, No. 6, 1990

- [127] H. Choi, F.H. Beck, Z. Szlarska-Smialowska, D.D. Macdonald, "The Effect of Flow on the Stress Corrosion Cracking of ASTM A508 Cl 2 Steel and AISI Type 304 Stainless Steel in High Temperature Water", *Corrosion*, Vol. 38, No. 2, 1982

| specimen number | material designation | test number | da/dt [m/s] | after test treatment | old KI [MPam ^{1/2}] |
|-----------------|----------------------|-------------|-------------|---|-------------------------------|
| 2135 | alloy C | 1 | no SCC | new fatigue crack | 61.2 |
| | | 2 | no SCC | load raised by 11.4% (7.4MPam ^{1/2}) | 65.0 |
| | | 3 | no SCC | load raised by 10.5% (7.6MPam ^{1/2}) | 72.4 |
| | | 4 | no SCC | broken open | 80.0 |
| 2136 | alloy C | 1 | no SCC | broken open | 62.6 |
| 2137 | alloy A | 1 | no SCC | new fatigue crack | 60.7 |
| | | 2 | no SCC | load raised by 10.6% (6.8MPam ^{1/2}) | 64.3 |
| | | 3 | no SCC | load raised by 9.0% (6.4MPam ^{1/2}) | 71.1 |
| | | 4 | no SCC | broken open | 77.5 |
| 2138 | alloy A | 1 | no SCC | broken open | 71.9 |
| 2139 | alloy C | 1 | no SCC | new fatigue crack | 69.6 |
| | | 2 | no SCC | broken open | 82.4 |
| 2140 | alloy B | 1 | no SCC | load raised by 48% (19.7MPam ^{1/2}) | 41.0 |
| | | 2 | no SCC | load raised by 13.7% (8.3MPam ^{1/2}) | 60.7 |
| | | 3 | no SCC | new fatigue crack | 69.0 |
| | | 4 | no SCC | broken open | 56.8 |
| 2141 | alloy B | 1 | no SCC | broken open | 57.7 |
| 2142 | alloy B | 1 | no SCC | new fatigue crack | 76.4 |
| | | 2 | no SCC | load raised by 8.7% (6.1MPam ^{1/2}) | 70.1 |
| | | 3 | no SCC | broken open | 76.2 |
| 2143 | alloy B | 1 | no SCC | broken open | 80.2 |
| 2144 | alloy B | 1 | no SCC | broken open | 41.2 |
| 2145 | alloy B | 1 | no SCC | load raised by 17.0% (9.9MPam ^{1/2}) | 58.3 |
| | | 2 | no SCC | load raised by 11.7% (8.0MPam ^{1/2}) | 68.2 |
| | | 3 | no SCC | load raised by 13.0% (9.9MPam ^{1/2}) | 76.2 |
| | | 4 | no SCC | broken open | 86.1 |
| 2146 | alloy B | 1 | no SCC | new fatigue crack | 72.4 |
| | | 2 | no SCC | load raised by 13.6% (9.8MPam ^{1/2}) | 72.0 |
| | | 3 | no SCC | broken open | 81.8 |
| 2147 | alloy B | 1 | no SCC | new fatigue crack | 87.4 |
| | | 2 | no SCC | load raised by 7.2% (5.1MPam ^{1/2}) | 71.1 |
| | | 3 | no SCC | broken open | 76.2 |
| 2148 | alloy B | 1 | no SCC | load raised by 14.1% (9.2MPam ^{1/2}) | 63.8 |
| | | 2 | no SCC | load raised by 16.2% (11.8MPam ^{1/2}) | 72.8 |
| | | 3 | no SCC | load raised by 9.2% (7.8MPam ^{1/2}) | 84.6 |
| | | 4 | no SCC | broken open | 92.4 |
| 2149 | alloy B | 1 | no SCC | load raised by 16.7% (11.0MPam ^{1/2}) | 65.9 |
| | | 2 | no SCC | load raised by 10.0% (7.7MPam ^{1/2}) | 76.9 |
| | | 3 | no SCC | load raised by 13.2% (11.2MPam ^{1/2}) | 84.6 |
| | | 4 | no SCC | broken open | 95.8 |
| 2150 | alloy B | 2 | no SCC | load raised by 8.7% (5.4MPam ^{1/2}) | 62.3 |
| | | 3 | no SCC | load raised by 11.1% (7.5MPam ^{1/2}) | 67.7 |
| | | 4 | no SCC | broken open | 75.2 |
| 2151 | alloy B | 2 | no SCC | load raised by 11.4% (7.8MPam ^{1/2}) | 68.3 |
| | | 3 | no SCC | new fatigue crack | 76.1 |
| | | 4 | no SCC | broken open | 59.6 |
| 2152 | alloy B | 2 | no SCC | load raised by 10.7% (7.1MPam ^{1/2}) | 66.1 |
| | | 3 | no SCC | new fatigue crack | 73.2 |
| | | 4 | no SCC | broken open | 58.9 |
| 2153 | alloy B | 2 | no SCC | broken open | 90.2 |
| 2154 | alloy A | 2 | no SCC | load raised by 12.4% (8.8MPam ^{1/2}) | 71.2 |
| | | 3 | no SCC | load raised by 14.1% (11.3MPam ^{1/2}) | 80.0 |
| | | 4 | no SCC | broken open | 91.3 |
| 2155 | alloy B | 3 | no SCC | load raised by 8.6% (5.1MPam ^{1/2}) | 59.5 |
| | | 4 | no SCC | broken open | 64.6 |

Tab I: Data of DCB specimens tested in the hot water loop at 288
(continued on next 7 pages)

| specimen number | material designation | test number | da/dt [m/s] | after test treatment | old KI [MPam ^{1/2}] |
|-----------------|----------------------|-------------|-------------|---|-------------------------------|
| 2156 | alloy B | 3 | no SCC | load raised by 15.0% (8.8MPam ^{1/2}) | 58.7 |
| | | 4 | no SCC | broken open | 67.5 |
| 2157 | alloy B | 4 | no SCC | broken open | 53.2 |
| 2158 | alloy B | 4 | no SCC | broken open | 54.7 |
| 2159 | alloy B | 4 | no SCC | broken open | 66.4 |
| 2160 | alloy B | 5&6 | no SCC | new fatigue crack | 26.2 |
| | | 8 | no SCC | load raised by 19.8% (6.4MPam ^{1/2}) | 32.3 |
| | | 9 | no SCC | load raised by 13.2% (5.1MPam ^{1/2}) | 38.7 |
| | | 10 | no SCC | load raised by 8.2% (3.6 MPam ^{1/2}) | 43.8 |
| | | 11 | 2.5E-9 | broken open | 47.4 |
| 2161 | alloy B | 5&6 | no SCC | new fatigue crack | 32.1 |
| | | 8 | no SCC | load raised by 12.4% (4.5MPam ^{1/2}) | 36.2 |
| | | 9 | no SCC | broken open | 40.7 |
| 2162 | alloy B | 5&6 | no SCC | new fatigue crack | 35.9 |
| | | 8 | no SCC | load raised by 14.9% (6.0MPam ^{1/2}) | 40.4 |
| | | 9 | no SCC | load raised by 14% (6.5MPam ^{1/2}) | 46.4 |
| | | 10 | no SCC | load raised by 11.3% (6.0MPam ^{1/2}) | 52.9 |
| | | 11 | 2.4E-9 | broken open | 58.9 |
| 2163 | alloy B | 5&6 | no SCC | new fatigue crack | 34.9 |
| | | 8 | no SCC | load raised by 11.4% (5.4MPam ^{1/2}) | 47.3 |
| | | 9 | no SCC | load raised by 14.0% (7.4MPam ^{1/2}) | 52.7 |
| | | 10 | no SCC | load raised by 11.5% (6.9 MPam ^{1/2}) | 60.1 |
| | | 11 | 3.5E-9 | broken open | 67.0 |
| 2164 | alloy B | 5&6 | no SCC | new fatigue crack | 74.4 |
| | | 8 | no SCC | load raised by 16.7% (8.9MPam ^{1/2}) | 53.2 |
| | | 9 | no SCC | load raised by 10.5% (6.5MPam ^{1/2}) | 62.1 |
| | | 10 | no SCC | load raised by 10.9% (7.5MPam ^{1/2}) | 68.6 |
| | | 11 | 5.3E-9 | broken open | 76.1 |
| 2165 | alloy B | 5&6 | no SCC | new fatigue crack | 49.9 |
| | | 8 | no SCC | load raised by 15.9% (8.9MPam ^{1/2}) | 56.1 |
| | | 9 | 4.0E-9 | broken open | 65.0 |
| 2166 | alloy B | 5&6 | no SCC | new fatigue crack | 61.3 |
| | | 8 | no SCC | load raised by 15.6% (9.4MPam ^{1/2}) | 60.2 |
| | | 10 | no SCC | broken open | 69.2 |
| 2167 | alloy B | 5&6 | no SCC | new fatigue crack | 69.1 |
| | | 8 | no SCC | load raised by 14.1% (8.5MPam ^{1/2}) | 60.5 |
| | | 9 | 3.2E-9 | broken open | 69.0 |
| 2168 | alloy B | 5&6 | no SCC | new fatigue crack | 36.5 |
| | | 8 | no SCC | load raised by 19.6% (6MPam ^{1/2}) | 30.6 |
| | | 9 | no SCC | load raised by 13.9% (5.1MPam ^{1/2}) | 36.6 |
| | | 10 | no SCC | load raised by 16.1 % (6.7MPam ^{1/2}) | 41.7 |
| | | 11 | no SCC | load raised by 14.5% (7.0MPam ^{1/2}) | 48.4 |
| | | 12 | 2.7E-9 | broken open | 55.4 |
| 2169 | alloy B | 5&6 | no SCC | new fatigue crack | 31.5 |
| | | 8 | no SCC | load raised by 13.8 % (5.7MPam ^{1/2}) | 41.4 |
| | | 10 | no SCC | load raised by 9.6 % (4.5MPam ^{1/2}) | 47.1 |
| | | 11 | no SCC | load raised by 12.6 % (6.5MPam ^{1/2}) | 51.6 |
| | | 12 | 2.2E-9 | broken open | 58.1 |
| 2170 | alloy B | 5&6 | no SCC | new fatigue crack | 34.7 |
| | | 8 | no SCC | load raised by 14.1% (7.2MPam ^{1/2}) | 50.9 |
| | | 9 | no SCC | load raised by 11.1% (6.5MPam ^{1/2}) | 58.1 |
| | | 10 | no SCC | load raised by 11.2% (6.5MPam ^{1/2}) | 64.6 |
| | | 11 | no SCC | load raised by 10.8% (7.0MPam ^{1/2}) | 71.6 |
| | | 12 | 2.2E-9 | broken open | 78.0 |

Tab. I: Continuation

| specimen number | material designation | test number | da/dt [m/s] | after test treatment | old KI [MPam ^{1/2}] |
|-----------------|----------------------|-------------|-------------|---|-------------------------------|
| 2171 | alloy B TL | 5&6 | no SCC | new fatigue crack | 36.5 |
| | | 8 | no SCC | load raised by 15.1% (6.8MPam ^{1/2}) | 45.0 |
| | | 9 | no SCC | broken open | 51.8 |
| 2172 | alloy B | 5&6 | no SCC | new fatigue crack | 33.8 |
| | | 8 | no SCC | load raised by 13.9% (7.2MPam ^{1/2}) | 51.7 |
| | | 9 | no SCC | load raised by 12.7% (7.5MPam ^{1/2}) | 58.9 |
| | | 10 | 2.8E-9 | broken open | 66.4 |
| 2173 | alloy B | 5&6 | no SCC | new fatigue crack | 48.1 |
| | | 8 | no SCC | load raised by 16.5% (9.1MPam ^{1/2}) | 55.1 |
| | | 9 | no SCC | load raised by 11.5% (7.4MPam ^{1/2}) | 64.2 |
| | | 10 | no SCC | load raised by 10.5% (7.5MPam ^{1/2}) | 71.6 |
| | | 11 | 6.2E-9 | broken open | 79.1 |
| 2174 | alloy B | 5&6 | no SCC | new fatigue crack | 60.5 |
| | | 8 | no SCC | load raised by 16.4% (9.7MPam ^{1/2}) | 59.3 |
| | | 9 | no SCC | load raised by 12.0% (8.3MPam ^{1/2}) | 69.0 |
| | | 10 | 3.7E-9 | broken open | 77.3 |
| 2175 | alloy B | 5&6 | no SCC | new fatigue crack | 67.1 |
| | | 7 | no SCC | load raised by 9.0% (5.2MPam ^{1/2}) | 58.0 |
| | | 8 | no SCC | load raised by 13.1% (8.3MPam ^{1/2}) | 63.2 |
| | | 9 | no SCC | load raised by 9.0% (8.1MPam ^{1/2}) | 71.5 |
| | | 10 | 5.9E-9 | broken open | 79.6 |
| 2176 | alloy B | 5&6 | no SCC | new fatigue crack | 80.5 |
| | | 7 | no SCC | load raised by 6.2% (4.7MPam ^{1/2}) | 75.3 |
| | | 8 | no SCC | load raised by 18.3% (14.6MPam ^{1/2}) | 80.0 |
| | | 9 | 2.3E-9 | broken open | 94.6 |
| 2177 | alloy C | 5&6 | no SCC | new fatigue crack | 29.9 |
| | | 7 | 1.3E-9 | broken open | 32.0 |
| 2178 | alloy C | 5&6 | no SCC | new fatigue crack | 36.6 |
| | | 7 | no SCC | load raised by 12.0% (4.4MPam ^{1/2}) | 36.7 |
| | | 8 | no SCC | load raised by 9.2% (3.8MPam ^{1/2}) | 41.1 |
| | | 9 | no SCC | load raised by 19.2% (8.6MPam ^{1/2}) | 44.9 |
| | | 10 | no SCC | load raised by 11.8% (6.3MPam ^{1/2}) | 53.5 |
| 2179 | alloy C | 5&6 | no SCC | new fatigue crack | 51.2 |
| | | 7 | 5.6E-9 | broken open | 51.3 |
| 2180 | alloy C | 5&6 | no SCC | new fatigue crack | 59.6 |
| | | 7 | 4.7E-9 | broken open | 59.0 |
| 2181 | alloy D | 5&6 | no SCC | new fatigue crack | 25.6 |
| | | 7 | no SCC | load raised by 25.5% (7.0MPam ^{1/2}) | 27.4 |
| | | 8 | no SCC | load raised by 11.0% (3.8MPam ^{1/2}) | 34.4 |
| | | 9 | no SCC | load raised by 11.0% (3.8MPam ^{1/2}) | 38.2 |
| | | 10 | no SCC | load raised by 9.3% (4.2MPam ^{1/2}) | 45.1 |
| | | 11 | no SCC | load raised by 8.3% (4.1MPam ^{1/2}) | 49.3 |
| | | 12 | no SCC | load raised by 9.0% (4.8MPam ^{1/2}) | 53.4 |
| 13 | no SCC | broken open | 58.1 | | |
| 2182 | alloy D | 5&6 | no SCC | new fatigue crack | 31.4 |
| | | 7 | no SCC | load raised by 21.8% (6.2MPam ^{1/2}) | 28.4 |
| | | 8 | no SCC | load raised by 20.2% (7MPam ^{1/2}) | 34.6 |
| | | 9 | no SCC | load raised by 18.3% (7.6MPam ^{1/2}) | 41.6 |
| | | 10 | no SCC | load raised by 11.2% (5.5MPam ^{1/2}) | 49.2 |
| | | 11 | no SCC | load raised by 8.8% (4.8MPam ^{1/2}) | 54.7 |
| | | 12 | no SCC | load raised by 8.7% (5.2MPam ^{1/2}) | 59.5 |
| 13 | no SCC | broken open | 64.7 | | |

Tab. I: Continuation

| specimen number | material designation | test number | da/dt [m/s] | after test treatment | old KI [MPam ^{1/2}] |
|-----------------|----------------------|-------------|-------------|---|-------------------------------|
| 2183 | alloy D | 5&6 | no SCC | new fatigue crack | 37.4 |
| | | 7 | no SCC | load raised by 23.9% (7.9MPam ^{1/2}) | 34.4 |
| | | 8 | no SCC | load raised by 10.2% (4.3MPam ^{1/2}) | 42.3 |
| | | 9 | 5.6E-9 | broken open | 46.6 |
| 2184 | alloy D | 5&6 | no SCC | new fatigue crack | 38.1 |
| | | 7 | no SCC | load raised by 13.1% (5.4MPam ^{1/2}) | 41.1 |
| | | 8 | 5.7E-9 | broken open | 46.5 |
| 2185 | alloy D | 5&6 | no SCC | new fatigue crack | 39.2 |
| | | 7 | no SCC | load raised by 20.8% (8.0MPam ^{1/2}) | 38.4 |
| | | 8 | no SCC | load raised by 15.3% (7.1MPam ^{1/2}) | 46.4 |
| | | 9 | no SCC | load raised by 15.1% (8.1MPam ^{1/2}) | 53.5 |
| | | 10 | no SCC | load raised by 9.4% (5.8MPam ^{1/2}) | 61.6 |
| | | 11 | 1.0E-8 | broken open | 67.4 |
| 2186 | alloy D | 5&6 | no SCC | new fatigue crack | 46.3 |
| | | 7 | no SCC | load raise by 17.9% (7.9MPam ^{1/2}) | 44.1 |
| | | 8 | no SCC | load raise by 13.5% (7MPam ^{1/2}) | 52.0 |
| | | 9 | 1.6E-8 | broken open | 59.0 |
| 2187 | alloy D | 5&6 | no SCC | new fatigue crack | 50.6 |
| | | 7 | 4.4E-9 | broken open | 53.0 |
| 2188 | alloy D | 5&6 | no SCC | new fatigue crack | 59.2 |
| | | 7 | 1.1E-9 | broken open | 59.8 |
| 2189 | alloy D | 5&6 | no SCC | new fatigue crack | 72.4 |
| | | 7 | no SCC | load raised by 12.2% (8.7MPam ^{1/2}) | 71.4 |
| | | 8 | 2.4E-9 | broken open | 80.1 |
| | | 8 | 2.4E-9 | broken open | 80.1 |
| 2306 | alloy A | 7 | no SCC | load raised by 7.8% (4.0MPam ^{1/2}) | 51.2 |
| | | 8 | no SCC | load raised by 16.8% (9.3MPam ^{1/2}) | 55.2 |
| | | 10 | no SCC | load raised by 13.2% (8.5MPam ^{1/2}) | 64.5 |
| | | 11 | no SCC | load raised by 15.5% (11.3MPam ^{1/2}) | 73.0 |
| | | 12 | 4.2E-9 | broken open | 84.3 |
| 2600 | alloy D | 9 | no SCC | load raised by 20.2% (3.3MPam ^{1/2}) | 16.3 |
| | | 10 | no SCC | load raised by 16.8% (3.3MPam ^{1/2}) | 19.6 |
| | | 11 | no SCC | load raised by 20.5% (4.7MPam ^{1/2}) | 22.9 |
| | | 12 | no SCC | load raised by 22.8% (6.4MPam ^{1/2}) | 27.6 |
| | | 13 | no SCC | broken open | 33.9 |
| 2601 | alloy D | 9 | no SCC | load raised by 44.7% (8.9MPam ^{1/2}) | 19.9 |
| | | 10 | no SCC | load raised by 8.0% (2.3MPam ^{1/2}) | 28.8 |
| | | 11 | no SCC | load raised by 16.7% (5.2MPam ^{1/2}) | 31.1 |
| | | 12 | no SCC | load raised by 17.9% (6.5MPam ^{1/2}) | 36.3 |
| | | 13 | no SCC | load raised by 16.8% (7.2MPam ^{1/2}) | 42.8 |
| | | 14 | no SCC | load raised by 13.8% (6.9MPam ^{1/2}) | 50.0 |
| | | 15 | no SCC | broken open | 56.9 |
| 2602 | alloy D | 9 | no SCC | load raised by 19.9% (5.1MPam ^{1/2}) | 25.6 |
| | | 10 | no SCC | load raised by 12.1% (3.7MPam ^{1/2}) | 30.7 |
| | | 11 | no SCC | load raised by 7.8% (2.7MPam ^{1/2}) | 34.4 |
| | | 12 | no SCC | load raised by 8.6% (3.3MPam ^{1/2}) | 37.1 |
| | | 13 | no SCC | load raised by 15.6% (6.3MPam ^{1/2}) | 40.3 |
| | | 14 | no SCC | load raised by 16.7% (7.8MPam ^{1/2}) | 46.6 |
| | | 15 | no SCC | broken open | 54.4 |
| 2603 | alloy D | 9 | no SCC | load raised by 16.7% (5.1MPam ^{1/2}) | 30.5 |
| | | 10 | no SCC | load raised by 12.6% (4.5MPam ^{1/2}) | 35.6 |
| | | 11 | no SCC | load raised by 15.7% (6.3MPam ^{1/2}) | 40.1 |
| | | 12 | no SCC | load raised by 9.9% (4.6MPam ^{1/2}) | 46.4 |
| | | 13 | no SCC | load raised by 11.2% (5.7MPam ^{1/2}) | 51.0 |
| | | 14 | no SCC | load raised by 19.0% (10.8 | 56.7 |
| | | 15 | no SCC | broken open | 67.5 |

Tab. I: Continuation

| specimen number | material designation | test number | da/dt [m/s] | after test treatment | old KI [MPam ^{1/2}] |
|-----------------|----------------------|-------------|-------------|--|-------------------------------|
| 2604 | alloy D | 9 | no SCC | load raised by 14.6% (4.5MPam ^{1/2}) | 30.7 |
| | | 10 | no SCC | load raised by 13.9% (4.9MPam ^{1/2}) | 35.2 |
| | | 11 | no SCC | load raised by 9.5% (3.8 MPam ^{1/2}) | 40.1 |
| | | 12 | no SCC | load raised by 9.8% (4.3MPam ^{1/2}) | 43.9 |
| | | 13 | no SCC | load raised by 8.9% (4.3MPam ^{1/2}) | 48.2 |
| | | 14 | no SCC | load raised by 10.9% (5.7MPam ^{1/2}) | 52.5 |
| | | 15 | no SCC | broken open | 58.2 |
| 2605 | alloy D | 9 | no SCC | load raised by 14.3% (4.4MPam ^{1/2}) | 30.8 |
| | | 10 | no SCC | load raised by 12.5% (4.4MPam ^{1/2}) | 35.2 |
| | | 11 | no SCC | load raised by 12.5% (4.4MPam ^{1/2}) | 39.6 |
| | | 12 | no SCC | load raised by 10.4% (4.5MPam ^{1/2}) | 43.4 |
| | | 13 | no SCC | load raised by 13.4% (6.4MPam ^{1/2}) | 47.9 |
| | | 14 | no SCC | load raised by 11.2% (6.1MPam ^{1/2}) | 54.3 |
| | | 15 | no SCC | broken open | 60.4 |
| 2606 | alloy D | 9 | no SCC | load raised by 9.3% (2.9MPam ^{1/2}) | 31.2 |
| | | 10 | no SCC | load raised by 11.7% (4.0MPam ^{1/2}) | 34.1 |
| | | 11 | no SCC | load raised by 11.5% (4.4MPam ^{1/2}) | 38.1 |
| | | 12 | no SCC | load raised by 9.4% (4MPam ^{1/2}) | 42.5 |
| | | 13 | no SCC | load raised by 8.4% (3.9MPam ^{1/2}) | 46.5 |
| | | 14 | no SCC | load raised by 13.5% (6.8MPam ^{1/2}) | 50.4 |
| | | 15 | no SCC | broken open | 57.2 |
| 2607 | alloy D | 9 | no SCC | load raised by 17.7% (6.2MPam ^{1/2}) | 35.0 |
| | | 10 | no SCC | load raised by 13.8% (5.7MPam ^{1/2}) | 41.2 |
| | | 11 | no SCC | load raised by 10.0% (4.7MPam ^{1/2}) | 46.9 |
| | | 12 | no SCC | load raised by 10.7% (5.5MPam ^{1/2}) | 51.6 |
| | | 13 | no SCC | load raised by 8.8% (5.0MPam ^{1/2}) | 57.1 |
| | | 14 | no SCC | load raised by 10.05(6.2MPam ^{1/2}) | 62.1 |
| | | 15 | no SCC | broken open | 68.3 |
| 2608 | alloy D | 9 | no SCC | load raised by 13.9% (5.2MPam ^{1/2}) | 37.3 |
| | | 10 | no SCC | load raised by 15.1% (6.4MPam ^{1/2}) | 42.5 |
| | | 11 | no SCC | load raised by 10.4% (5.1MPam ^{1/2}) | 48.9 |
| | | 12 | no SCC | load raised by 11.3% (6.1MPam ^{1/2}) | 54.0 |
| | | 13 | no SCC | load raised by 13.5% (8.1MPam ^{1/2}) | 60.1 |
| | | 14 | no SCC | load raised by 11.0% (7.5MPam ^{1/2}) | 68.2 |
| | | 15 | no SCC | broken open | 75.7 |
| 2609 | alloy C | 10 | no SCC | load raised by 7.4% (2.3MPam ^{1/2}) | 31.2 |
| | | 11 | 1.6E-8 | broken open | 33.5 |
| 2610 | alloy C | 10 | no SCC | load raised by 11.2% (3.8MPam ^{1/2}) | 34.0 |
| | | 11 | no SCC | load raised by 15.6% (5.9MPam ^{1/2}) | 37.8 |
| | | 12 | no SCC | load raised by 9.4% (4.1MPam ^{1/2}) | 43.7 |
| | | 13 | no SCC | load raised by 14.6% (7.0MPam ^{1/2}) | 47.8 |
| | | 14 | no SCC | load raised by 13.3% (7.3MPam ^{1/2}) | 54.8 |
| 15 | no SCC | broken open | 62.1 | | |
| 2611 | alloy C | 10 | no SCC | load raised by 12.2% (5.0MPam ^{1/2}) | 40.9 |
| | | 11 | no SCC | load raised by 11.5% (5.3MPam ^{1/2}) | 45.9 |
| | | 12 | no SCC | load raised by 10.7% (5.5MPam ^{1/2}) | 51.2 |
| | | 13 | no SCC | load raised by 7.4% (4.2MPam ^{1/2}) | 56.7 |
| | | 14 | no SCC | load raised by 14.1% (8.6MPam ^{1/2}) | 60.9 |
| 15 | no SCC | broken open | 69.5 | | |
| 2612 | alloy C | 10 | no SCC | load raised by 8.1% (3.3MPam ^{1/2}) | 40.7 |
| | | 11 | no SCC | load raised by 10.9% (4.8MPam ^{1/2}) | 44.0 |
| | | 12 | no SCC | load raised by 8.4% (4.1MPam ^{1/2}) | 48.8 |
| | | 13 | no SCC | load raised by 11.5% (6.1MPam ^{1/2}) | 52.9 |
| | | 14 | no SCC | load raised by 13.2% (7.8MPam ^{1/2}) | 59.0 |
| 15 | no SCC | broken open | 66.8 | | |

Tab. I: Continuation

| specimen number | material designation | test number | da/dt [m/s] | after test treatment | old KI [MPam ^{1/2}] |
|-----------------|----------------------|-------------|-------------|---|-------------------------------|
| 2640 | alloy C | 11 | no SCC | load raised by 20.1% (3.1MPam ^{1/2}) | 15.4 |
| | | 12 | no SCC | load raised by 25.4% (4.7MPam ^{1/2}) | 18.5 |
| | | 13 | no SCC | load raised by 34.9% (8.1MPam ^{1/2}) | 23.2 |
| | | 14 | no SCC | load raised by 28.4% (8.9MPam ^{1/2}) | 31.3 |
| | | 15 | no SCC | broken open | 40.2 |
| 2641 | alloy C | 11 | no SCC | load raised by 11.7% (2.4mPam ^{1/2}) | 20.6 |
| | | 12 | no SCC | load raised by 10.0% (2.3MPam ^{1/2}) | 23.0 |
| | | 13 | no SCC | load raised by 30.0% (7.6MPam ^{1/2}) | 25.3 |
| | | 14 | no SCC | load raised by 23.7% (7.8MPam ^{1/2}) | 32.9 |
| | | 15 | no SCC | broken open | 40.7 |
| 2642 | alloy C | 11 | no SCC | load raised by 15.3% (2.5MPam ^{1/2}) | 16.3 |
| | | 12 | no SCC | load raised by 7.4% (1.4MPam ^{1/2}) | 18.8 |
| | | 13 | no SCC | load raised by 55.0% (11.1MPam ^{1/2}) | 20.2 |
| | | 14 | no SCC | load raised by 42.4% (13.2MPam ^{1/2}) | 31.1 |
| | | 15 | no SCC | broken open | 44.3 |
| 2643 | alloy C | 11 | no SCC | load raised by 33.5% (5.3 MPam ^{1/2}) | 15.8 |
| | | 12 | no SCC | load raised by 9.0% (1.9MPam ^{1/2}) | 21.1 |
| | | 13 | no SCC | load raised by 33.9% (7.8MPam ^{1/2}) | 23.0 |
| | | 14 | no SCC | broken open | 30.8 |
| 2651 | alloy C | 12 | no SCC | load raised by 17.5% (2.7MPam ^{1/2}) | 15.4 |
| | | 13 | no SCC | load raised by 50.3% (9.1MPam ^{1/2}) | 18.1 |
| | | 14 | no SCC | load raised by 47% (12.8MPam ^{1/2}) | 27.2 |
| | | 15 | no SCC | broken open | 40.0 |
| 2652 | alloy C | 12 | no SCC | load raised by 12.2% (2.3MPam ^{1/2}) | 18.9 |
| | | 13 | no SCC | load raised by 47.2% (10.0MPam ^{1/2}) | 21.2 |
| | | 14 | no SCC | load raised by 16.0% (5.0MPam ^{1/2}) | 31.2 |
| | | 15 | no SCC | broken open | 36.2 |
| 2653 | alloy C | 12 | no SCC | load raised by 12.1% (2.1MPam ^{1/2}) | 17.3 |
| | | 13 | no SCC | load raised by 36.1% (7.0MPam ^{1/2}) | 19.4 |
| | | 14 | no SCC | load raised by 42.4% (11.2MPam ^{1/2}) | 26.4 |
| | | 15 | no SCC | broken open | 37.6 |
| 2654 | alloy C | 12 | no SCC | load raised by 15.1% (2.3MPam ^{1/2}) | 15.2 |
| | | 13 | no SCC | load raised by 46.9% (8.2MPam ^{1/2}) | 17.5 |
| | | 14 | no SCC | load raised by 45.1% (11.6MPam ^{1/2}) | 25.7 |
| | | 15 | no SCC | broken open | 37.3 |
| 2655 | alloy A | 12 | no SCC | load raised by 28.4% (4.6MPam ^{1/2}) | 16.2 |
| | | 13 | no SCC | load raised by 32.2% (6.7MPam ^{1/2}) | 20.8 |
| | | 14 | no SCC | load raised by 32.4% (8.9MPam ^{1/2}) | 27.5 |
| | | 15 | no SCC | broken open | 36.4 |
| 2656 | alloy A | 12 | no SCC | load raised by 12.4% (2.4MPam ^{1/2}) | 19.3 |
| | | 13 | no SCC | load raised by 27.6% (6.0MPam ^{1/2}) | 21.7 |
| | | 14 | no SCC | load raised by 24.2% (6.7MPam ^{1/2}) | 27.7 |
| | | 15 | no SCC | load raised by 24.1% (8.3MPam ^{1/2}) | 34.4 |
| | | 16 | no SCC | load raised by 19.0% (8.1MPam ^{1/2}) | 42.7 |
| | | 17 | no SCC | load raised by 10.8% (5.5MPam ^{1/2}) | 50.8 |
| 18 | no SCC | broken open | 56.3 | | |
| 2657 | alloy A | 12 | no SCC | load raised by 30.8% (4.9MPam ^{1/2}) | 15.9 |
| | | 13 | no SCC | load raised by 29.3% (6.1MPam ^{1/2}) | 20.8 |
| | | 14 | no SCC | load raised by 22.7% (6.1MPam ^{1/2}) | 26.9 |
| | | 15 | no SCC | load raised by 27.3% (9.0MPam ^{1/2}) | 33.0 |
| | | 16 | no SCC | load raised by 27.6% (11.6MPam ^{1/2}) | 42.0 |
| | | 17 | no SCC | load raised by 17.1% (9.2MPam ^{1/2}) | 53.6 |
| 18 | no SCC | broken open | 62.8 | | |

Tab. I: Continuation

| specimen number | material designation | test number | da/dt [m/s] | after test treatment | old KI [MPam ^{1/2}] |
|-----------------|----------------------|-------------|-------------|---|-------------------------------|
| 2658 | alloy A | 12 | no SCC | load raised by 13.9% (2.9MPam ^{1/2}) | 20.8 |
| | | 13 | no SCC | load raised by 26.6% (6.3MPam ^{1/2}) | 23.7 |
| | | 14 | no SCC | load raised by 29.3% (8.8MPam ^{1/2}) | 30.0 |
| | | 15 | no SCC | broken open | 38.8 |
| 2720 | alloy D | 14 | no SCC | load raised by 28.3% (7.0MPam ^{1/2}) | 24.7 |
| | | 15 | no SCC | load raised by 27.4% (8.7MPam ^{1/2}) | 31.7 |
| | | 16 | no SCC | load raised by 27.4% (8.7MPam ^{1/2}) | 40.4 |
| | | 17 | no SCC | load raised by 19.8% (10.4MPam ^{1/2}) | 52.3 |
| 18 | 1.4E-10 | broken open | 62.7 | | |
| 2721 | alloy D | 14 | no SCC | load raised by 53.6% (10.4MPam ^{1/2}) | 19.4 |
| | | 15 | no SCC | load raised by 45.6% (13.6MPam ^{1/2}) | 29.8 |
| | | 16 | no SCC | load raised by 45.2% (19.6MPam ^{1/2}) | 43.3 |
| | | 17 | 9.0E-11 | broken open | 62.9 |
| 2722 | alloy D | 14 | no SCC | load raised by 43.4% (8.2MPam ^{1/2}) | 18.9 |
| | | 15 | no SCC | load raised by 43.2% (11.7MPam ^{1/2}) | 27.1 |
| | | 16 | no SCC | load raised by 54.1% (21.0MPam ^{1/2}) | 38.8 |
| | | 17 | no SCC | load raised by 20.5% (12.3MPam ^{1/2}) | 59.8 |
| 18 | no SCC | broken open | 72.1 | | |
| 2723 | alloy D | 14 | no SCC | load raised by 34.9% (8.2MPam ^{1/2}) | 23.5 |
| | | 15 | no SCC | load raised by 47.6% (15.1MPam ^{1/2}) | 31.7 |
| | | 16 | no SCC | load raised by 22.0% (10.3MPam ^{1/2}) | 46.8 |
| | | 17 | no SCC | load raised by 18.5% (10.6MPam ^{1/2}) | 57.1 |
| 18 | no SCC | broken open | 67.7 | | |
| 2724 | alloy C | 14 | no SCC | load raised by 39.9% (7.5MPam ^{1/2}) | 18.8 |
| | | 15 | no SCC | load raised by 51.7% (13.6MPam ^{1/2}) | 26.3 |
| | | 16 | no SCC | load raised by 45.4% (18.1MPam ^{1/2}) | 39.9 |
| | | 17 | no SCC | load raised by 18.6% (10.8MPam ^{1/2}) | 58.0 |
| 18 | no SCC | broken open | 68.8 | | |
| 2725 | alloy C | 14 | no SCC | load raised by 49.7% (9.6MPam ^{1/2}) | 19.3 |
| | | 15 | no SCC | load raised by 42.2% (12.2MPam ^{1/2}) | 28.9 |
| | | 16 | no SCC | load raised by 32.6% (13.4MPam ^{1/2}) | 41.1 |
| | | 17 | no SCC | load raised by 15.2% (8.3MPam ^{1/2}) | 54.5 |
| 18 | no SCC | broken open | 62.8 | | |
| 2726 | alloy C | 14 | no SCC | load raised by 58.5% (11.3MPam ^{1/2}) | 19.3 |
| | | 15 | no SCC | load raised by 29.7% (9.1MPam ^{1/2}) | 30.6 |
| | | 16 | no SCC | load raised by 29.7% (9.1MPam ^{1/2}) | 39.7 |
| | | 17 | no SCC | load raised by 17.4% (9.4MPam ^{1/2}) | 53.9 |
| 18 | no SCC | broken open | 63.3 | | |
| 2754 | alloy D | 15 | no SCC | load raised by 36.8% (10.0MPam ^{1/2}) | 27.2 |
| | | 16 | no SCC | load raised by 61% (22.7MPam ^{1/2}) | 37.2 |
| | | 17 | no SCC | broken open | 59.9 |
| 2782 | alloy C | 16 | no SCC | load raised by 34.1% (10.8MPam ^{1/2}) | 31.6 |
| | | 17 | no SCC | load raised by 32.7% (13.9MPam ^{1/2}) | 42.4 |
| | | 18 | no SCC | broken open | 56.3 |
| 2783 | alloy C | 16 | no SCC | load raised by 27.8% (8.3MPam ^{1/2}) | 29.8 |
| | | 17 | no SCC | load raised by 30.1% (11.5MPam ^{1/2}) | 38.1 |
| | | 18 | no SCC | broken open | 49.6 |
| 2784 | alloy C | 16 | no SCC | load raised by 44.1% (12.8MPam ^{1/2}) | 29.0 |
| | | 17 | no SCC | load raised by 17.4% (7.3MPam ^{1/2}) | 41.8 |
| | | 18 | no SCC | broken open | 49.1 |
| 2785 | alloy C | 16 | no SCC | load raised by 46.2% (13.4MPam ^{1/2}) | 29.0 |
| | | 17 | no SCC | load raised by 29% (12.3MPam ^{1/2}) | 42.4 |
| | | 18 | no SCC | broken open | 54.7 |
| 2786 | alloy C | 16 | no SCC | load raised by 41.2% (14.3MPam ^{1/2}) | 34.7 |
| | | 17 | no SCC | load raised by 21.4% (10.5MPam ^{1/2}) | 49.0 |
| | | 18 | no SCC | broken open | 59.5 |

Tab. I: Continuation

| specimen number | material designation | test number | da/dt [m/s] | after test treatment | old KI [MPam ^{1/2}] |
|-----------------|----------------------|-------------|-------------|---|-------------------------------|
| 2787 | alloy C | 16 | no SCC | load raised by 69% (15.4MPam ^{1/2}) | 22.3 |
| | | 17 | no SCC | load raised by 35% (13.2MPam ^{1/2}) | 37.7 |
| | | 18 | no SCC | broken open | 50.9 |
| 2788 | alloy C | 16 | no SCC | load raised by 62% (15.7MPam ^{1/2}) | 25.3 |
| | | 17 | no SCC | load raised by 24.3% (10MPam ^{1/2}) | 41.0 |
| | | 18 | no SCC | broken open | 51.0 |
| 2789 | alloy C | 16 | no SCC | load raised by 52.8% (11.3MPam ^{1/2}) | 21.4 |
| | | 17 | no SCC | load raised by 32.4% (10.6MPam ^{1/2}) | 32.7 |
| | | 18 | no SCC | broken open | 43.3 |
| 2790 | alloy C | 16 | no SCC | load raised by 58.7% (13.7MPam ^{1/2}) | 23.3 |
| | | 17 | no SCC | load raised by 20.5% (7.6MPam ^{1/2}) | 37.0 |
| | | 18 | no SCC | broken open | 44.6 |
| 2791 | alloy C | 16 | no SCC | load raised by 93.2% (22.2MPam ^{1/2}) | 23.8 |
| | | 17 | no SCC | load raised by 18.9% (8.7MPam ^{1/2}) | 46.0 |
| | | 18 | no SCC | broken open | 54.7 |
| 2792 | alloy C | 16 | no SCC | load raised by 63.7% (15.5MPam ^{1/2}) | 24.3 |
| | | 17 | no SCC | load raised by 29.1% (11.6MPam ^{1/2}) | 39.8 |
| | | 18 | no SCC | broken open | 51.4 |
| 2793 | alloy C | 16 | no SCC | load raised by 67.3% (18.6MPam ^{1/2}) | 27.6 |
| | | 17 | no SCC | load raised by 25.3% (11.7MPam ^{1/2}) | 46.2 |
| | | 18 | no SCC | broken open | 57.9 |
| 2794 | alloy D | 16 | no SCC | load raised by 88.5% (23.1MPam ^{1/2}) | 26.1 |
| | | 17 | no SCC | load raised by 28.4% (14MPam ^{1/2}) | 49.2 |
| | | 18 | no SCC | broken open | 63.2 |
| 2795 | alloy D | 16 | no SCC | load raised by 71.4% (19.8MPam ^{1/2}) | 27.7 |
| | | 17 | no SCC | load raised by 34.3% (16.3MPam ^{1/2}) | 47.5 |
| | | 18 | no SCC | broken open | 63.8 |
| 2796 | alloy D | 16 | no SCC | load raised by 72% (20.4MPam ^{1/2}) | 28.3 |
| | | 17 | no SCC | load raised by 20.9% (10.2MPam ^{1/2}) | 48.7 |
| | | 18 | no SCC | broken open | 58.9 |
| 2797 | alloy D | 16 | no SCC | load raised by 70.1% (19.3MPam ^{1/2}) | 27.5 |
| | | 17 | no SCC | broken open | 46.8 |
| 2798 | alloy D | 16 | no SCC | load raised by 59.1% (16.5MPam ^{1/2}) | 27.9 |
| | | 17 | no SCC | load raised by 21.6% (9.6MPam ^{1/2}) | 44.4 |
| | | 18 | no SCC | broken open | 54.0 |
| 2799 | alloy D | 16 | no SCC | load raised by 64.5% (20MPam ^{1/2}) | 31.0 |
| | | 17 | no SCC | load raised by 19.8% (10.1MPam ^{1/2}) | 51.0 |
| | | 18 | no SCC | broken open | 61.1 |
| 2800 | alloy C | 16 | no SCC | load raised by 58.4% (14.2MPam ^{1/2}) | 24.3 |
| | | 17 | no SCC | load raised by 19.4% (7.5MPam ^{1/2}) | 38.5 |
| | | 18 | no SCC | broken open | 46.0 |
| 2801 | alloy C | 16 | no SCC | load raised by 29.2% (9.2MPam ^{1/2}) | 31.5 |
| | | 17 | no SCC | broken open | 40.7 |

Tab. I: Continuation

| Specimen # | Specimen designation | Stress intensity range [MPam ^{1/2}] | Temperature [°C] | da/dt | [O ₂] |
|------------|----------------------|--|---------------------|---------|-------------------|
| | | | | [m/s] | [ppm] |
| 1733 | alloy A | 71 - 76 | 285 | 9.0E-9 | 1.3 |
| 1984 | alloy A | 66 - 69 | 264 | 1.1E-8 | 18.0 |
| 1984 | alloy A | 73 - >80 | 264 | 1.3E-8 | 20 to 1.3 |
| 1964 | alloy A | 56 - 58 | 240 | 5.7E-9 | 1.0 |
| 1977 | alloy B | 65 - 84 | 286 | 6.0E-9 | 1.5 |
| 1977 | alloy B | 65 - 84 | 286 | 8.0E-9 | 1.5 |
| 1977 | alloy B | 70 - 84 | 286 | 2.5E-8 | 7.0 |
| 1972 | alloy B | 64 - 67 | 264 | 1.3E-8 | 2.0 |
| 1981 | alloy B | 65 - 67 | 264 | 1.2E-8 | 4.7 |
| 1978 | alloy B | 66 - 72 | 256 | 9.7E-9 | 5.0 |
| 1982 | alloy B | 77 | 246 | 8.6E-9 | 33.0 |
| 1967 | alloy B | 64 - 71 | 240 | 6.7E-9 | 0.7 |
| 2297 | alloy B | 51 - 58 | 238 | 9.0E-9 | - |
| 1972 | alloy B | 67 - 70 | 218 | 5.3E-9 | 3.0 |
| 1978 | alloy B | 72 - 77 | 210 | 4.3E-9 | 7.0 |
| 1981 | alloy B | 67 - 70 | 210 | 4.0E-9 | 7.0 |
| 1981 | alloy B | 70 - 73 | 194 | 2.8E-9 | 7.0 |
| 1978 | alloy B | 80 - 83 | 188 | 2.8E-9 | 7.0 |
| 1978 | alloy B | 83 | 178 | 7.4E-10 | 6.5 |
| 1690 | alloy C | 61 - 74 | 285 | 1.5E-8 | 1.0 |
| 1690 | alloy C | 61 - 74 | 285 | 2.2E-8 | 1.0 |
| 1735 | alloy C | 72 - 103 | 285 | 6.0E-9 | 1.6 |
| 1735 | alloy C | 72 - 103 | 285 | 1.1E-8 | 1.6 |
| 2191 | alloy C | 69 | 285 | 1.4E-8 | 20.0 |
| 1689 | alloy C | 67 - 74 | 277 | 1.1E-8 | 1.0 |
| 1689 | alloy C | 56 - 60 | 274 | 1.3E-8 | 1.0 |
| 1983 | BW30 | 75 - 76 | 299 | 1.8E-9 | 7.3 |
| 1983 | BW30 | 70 - 75 | 287 | 9.6E-9 | 10.5 |
| 1983 | BW30 | 76 - 77 | 277 | 7.3E-9 | 15.4 |
| 1983 | BW30 | 77 - >80 | 239 | 6.3E-9 | 20.6 |

Tab II: Experimental parameters and results of constant load tests with fracture mechanics DCB specimens (continued on next page)

| Specimen # | Specimen designation | Stress intensity range | Temperature | da/dt | [O ₂] |
|---------------------|----------------------|------------------------|-------------|--------|-------------------|
| | | [MPam ^{1/2}] | [°C] | [m/s] | [ppm] |
| 2781 | alloy D | 40 - 80 | 320 | 5.0E-8 | 200 |
| 2296 | alloy D | 46 - 50 | 300 | 1.3E-8 | - |
| 2296 | alloy D | 60 | 300 | 3.0E-8 | - |
| 2199 | alloy D | 60 - >76 | 287 | 3.0E-8 | - |
| 2200 | alloy D | 45 - 54 | 288 | 2.0E-8 | - |
| 2293 | alloy D | 45 | 288 | 3.0E-8 | - |
| 2190 | alloy D | 44.5 - 77 | 264 | 2.0E-8 | - |
| 2194 | alloy D | 44 - 53 | 264 | 2.0E-8 | - |
| 2194 | alloy D | 44 - 53 | 264 | 3.0E-8 | - |
| 2195 | alloy D | 56-60 | 264 | 1.4E-8 | - |
| 2195 | alloy D | 63 - 72 | 264 | 2.0E-8 | - |
| 2196 | alloy D | 47 - 53 | 240 | 9.6E-9 | - |
| 2196 | alloy D | 53 - 55 | 240 | 1.0E-8 | - |
| 2290 | alloy D | 56 - 71 | 240 | 1.0E-8 | - |
| 2292 | alloy D | 42 - 58 | 240 | 1.1E-8 | - |
| 2298 | alloy D | 42 | 240 | 8.6E-9 | - |
| 2298 | alloy D | 49 | 240 | 1.1E-8 | - |
| 2298 | alloy D | >60 | 240 | 1.2E-8 | - |
| 2198 | alloy D | 54 - 65 | 223 | 4.0E-9 | - |
| 2198 | alloy D | 54 - 65 | 223 | 5.0E-9 | - |
| 2190 | alloy D | 77 - 83 | 211 | 4.0E-9 | - |
| 2197 | alloy D | 57 | 200 | 3.0E-9 | - |
| 2299 | alloy D | 55 | 199 | 2.8E-9 | - |
| 2300 ⁽¹⁾ | A508-II | 63 - 90 | 240 | 1.4E-8 | - |
| 2301 ⁽¹⁾ | A508-II | 80 - 100 | 240 | 2E-8 | - |
| 2302 | A508-II | 50 - 70 | 240 | 1.5E-8 | - |

(1) ICT-Specimen

Tab II: Experimental parameters and results of constant load tests with fracture mechanics DCB specimens

CURRICULUM VITAE

Name: Kraus, Andreas
Date and City of Birth: January 1, 1964, Uster

Education

1971 - 1977 Primary School in Uster
1977 - 1984 Secondary and High School KZO Wetzikon, Graduation Type C
1984 - 1989 Studies of Material Science at the Swiss Federal Institute of Technology (ETH) in Zurich, Graduation
1989 - 1994 Preparation of the Ph. D. Thesis at the Institute of Metallurgy at the Swiss Federal Institute of Technology

Employment

1984 - 1989 Several practical studies at Sulzer Rüti, Mettler AG , EMPA Dübendorf
1989 - 1994 Research Assistant at the Institute of Metallurgy, ETHZ

Languages

German, English, French